
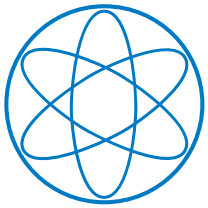


Doctoral Thesis in Physics at
Technische Universität München

Power exhaust in future alternative divertor configurations for the ASDEX Upgrade tokamak

presented by

Ou Pan

First examiner: Prof. Dr. Ulrich Stroth

Second examiner: Prof. Dr. Aliaksandr Bandarenka

Supervisor: Prof. Dr. Ulrich Stroth

Fakultät für Physik, Technische Universität München

Power exhaust in future alternative divertor configurations for the ASDEX Upgrade tokamak

Ou Pan

Vollständiger Abdruck der von der Fakultät für Physik der Technischen Universität München zur Erlangung des akademischen Grades eines

Doktors der Naturwissenschaften

genehmigten Dissertation.

Vorsitzender:

Prof. Dr. David Egger

Prüfender der Dissertation:

1. Prof. Dr. Ulrich Stroth

2. Prof. Dr. Aliaksandr Bandarenka

Die Dissertation wurde am 24.09.2020 bei der Technischen Universität München eingereicht und durch die Fakultät für Physik am 17.11.2020 angenommen.

Abstract

In the experimental thermonuclear fusion reactor under construction, ITER, and its planned successor, DEMO, the power exhaust is one of the most critical challenges. As the interaction regions between the confined plasma and the solid surfaces of the surrounding vessel, the scrape-off layer and divertor play a crucial role in the power and particle exhaust. High power loads on the plasma-facing components and especially on the divertor targets impose severe constraints on the achievable performance of future reactors.

Recently it was decided to upgrade the upper divertor of the ASDEX Upgrade tokamak to study alternative divertor configurations which are currently discussed as a possible solution for the power exhaust problem.

By means of numerical simulations, this thesis investigates power exhaust in two alternative divertor configurations, namely the X-divertor and the snowflake divertor. Compared to the conventional single null configuration with the same external input parameters and background profiles, the alternative divertor configurations show lower power loads at the divertor targets, and the targeted state of divertor detachment can be achieved with radiation cooling at lower impurity ion concentrations. This is possible due to the higher capacity of power and momentum removal via enhanced volumetric processes and cross-field transport.

In order to optimize the magnetic equilibrium and make predictions for the future upper divertor geometry, a series of upper single null high confinement discharges were carried out in ASDEX Upgrade and used for the comparison with simulations done with the SOLPS-ITER code. Transport coefficients, boundary conditions and gas puffing rate were adapted iteratively to achieve the best overall fit to experimental measurements. By using the same coefficients, the plasma conditions in single null configuration were extrapolated to those in X-divertor and snowflake divertor configurations. The simulation results confirm the above mentioned advantages in the alternative divertor configurations and make an optimistic prediction for the power exhaust performance in the future upper divertor of ASDEX Upgrade.

In addition, SOLPS-ITER simulations with fluid drifts fully activated are carried out in the snowflake divertor configuration for the first time. The drifts induce poloidal and radial convective transport, which leads to a power flux redistribution between the primary and secondary strike points in the snowflake divertor. Power is found even on a strike point magnetically disconnected from the main plasma. The activation of secondary strike points was one of the motivations for studying the snowflake configuration. Here the effect is small, but

it might be interesting for a reactor if the effect scales favorably with machine size.

Kurzfassung

Für den im Bau befindlichen experimentellen thermonuklearen Fusionsreaktor ITER und seinem geplanten Nachfolger DEMO ist die Leistungsabfuhr eine der kritischsten Herausforderungen. Für diese Leistungsabfuhr spielen der Scrape-off layer (dt. Abschälschicht) und der Divertor eine entscheidende Rolle. Die hohen Wärmebelastungen an den plasmaexponierten Oberflächen der Divertortargets stellen erhebliche Einschränkungen für die erreichbare Leistung zukünftiger Reaktoren dar.

An ASDEX Upgrade wurde kürzlich der Ausbau des oberen Divertors beschlossen, um alternative Divertorkonfigurationen zu untersuchen, die derzeit als mögliche Lösung für das Problem der Leistungsabfuhr diskutiert werden.

In dieser Arbeit werden numerische Simulationen für zwei Arten von Divertor beschrieben, der X-Divertor und der Snowflake-Divertor. Im Vergleich zur herkömmlichen Konfiguration mit einem magnetischen X-Punkt und sonst denselben Parametern zeigen die alternative Divertorkonfigurationen geringere Wärmebelastungen der Divertorziegel und die angestrebte Entkopplung des Plasmas vom Divertor durch Strahlungskühlung schon bei geringer Konzentrationen an eingebrachten Verunreinigungen. Als Ursache hierfür wurde die erhöhte Leistungs- und Impulsdissipation durch volumetrische Prozesse, sowie Transport senkrecht zum Magnetfeld über die sekundäre Separatrix im Snowflake-Divertor identifiziert.

Um die magnetische Konfiguration zu optimieren und Vorhersagen für den oberen Divertor in der zukünftigen Geometrie zu treffen, wurde in ASDEX Upgrade eine Reihe von Entladungen mit hohem Einschluss durchgeführt und für den Vergleich mit den Simulationen verwendet. Simulationen wurden mit dem Code SOLPS-ITER durch gefährt, wobei die Transportkoeffizienten, Randbedingungen und die Gasinjektionsrate iterativ anwurden, um die beste Übereinstimmung mit den experimentellen Messungen zu erzielen. Unter Verwendung der gleichen Parameter wurden dann die Bedingungen von der aktuelle Konfiguration auf diejenigen in X- und Snowflake-Divertor extrapoliert. Die Simulationsergebnisse bestätigen die oben genannten Vorteile der alternative Divertorkonfigurationen und erlauben eine optimistische Vorhersage für die Leistungsabfuhr im zukünftigen oberen Divertor in ASDEX Upgrade.

Weiterhin wurden erstmals Simulationen mit SOLPS-ITER bei vollständig aktivierten Plasmadriften in der Snowflake-Konfiguration durchgeführt. Diese Simulationen zeigen einen modifizierten poloidalen und radialen konvektiven Transport, der zu einer Umverteilung der Teilchen- und Wärmeflüsse zwischen dem primären und dem sekundären Auftreffpunkt im Snowflake-Divertor führt. Leistung wird sogar an einer Stelle gefunden, die magnetisch vom Hauptplasma getrennt ist. Die Aktivierung von sekundären Auftreffpunkte war eine der

Motivationen für die Untersuchung der Snowflakekonfigurationen. Hier ist der Effekt gering, aber er könnte für einen Reaktor interessant sein, wenn er mit der Maschinengröße günstig skaliert.

Contents

1 Motivation and scope of this thesis **1**

2 Introduction **5**
2.1 Controlled thermonuclear fusion 5
2.2 Tokamak 6
2.3 Divertor and scrape-off layer 7
2.4 Plasma confinement 9
2.5 The ASDEX Upgrade tokamak 10

3 Divertor physics **15**
3.1 Sheath theory 15
3.2 Power transport in the SOL and divertor 16
3.3 Divertor regimes 19
3.4 Drifts 22
3.5 Alternative divertor configurations 23
3.5.1 Snowflake divertor 24
3.5.2 X-divertor 27
3.5.3 Other alternative divertor configurations 27
3.5.4 Alternative divertor configurations for the divertor in ASDEX Upgrade 28

4 The SOLPS code package **31**
4.1 Model equations 31
4.2 Boundary conditions 35
4.3 Physics of neutral particles 36
4.4 Setup for a snowflake configuration 37

5 SOLPS simulations comparing the single null and alternative divertor configurations **41**
5.1 Simulation setup 41
5.2 Divertor behaviour 43
5.3 Radiation and volumetric recombination 46

5.4 Summary 49

6 Impurity seeding scan **51**
6.1 Evolution of divertor detachment 51
6.1.1 Low-seeding cases 53
6.1.2 High-seeding cases 55
6.2 Power and particle balances in the SOL 58
6.2.1 Inner divertor 61
6.2.2 Outer divertor 63
6.3 Summary 65

7 Predictions for the future ASDEX Upgrade divertor based on experimental data **67**
7.1 Experiments and simulations setup 67
7.2 Extrapolation to the future upper divertor 71
7.2.1 Snowflake divertor 73
7.2.2 X-divertor 79
7.3 Summary 82

8 Drifts effects **83**
8.1 Simulation setup 84
8.2 Simulation results 85
8.3 Summary 90

9 Conclusion **93**

Chapter 1

Motivation and scope of this thesis

In a thermonuclear fusion process, two lighter atomic nuclei such as hydrogen isotopes combine to form a heavier nucleus such as helium and release energy. In order to overcome the electrostatic repulsion between the nuclei, the kinetic energy of the reactants should be sufficiently high ($\sim$ 10 keV). In such condition, the fuel atoms are ionized and form a plasma. Controlled thermonuclear fusion is a potential source of clean, safe and virtually unlimited energy.

The divertor tokamak concept is one of the leading approaches to a fusion reactor, where a high-temperature plasma is confined in a toroidal vessel by a magnetic field. The world's largest experimental reactor under construction, ITER [1], and its planned successor, DEMO [2], are both designed based on this concept. In a conventional single null divertor configuration (see Fig. 1.1 (a)), there is a poloidal magnetic field null (X-point) and a magnetic separatrix crossing it. Inside the separatrix, magnetic field lines are termed closed and never make contact with the vessel components. In the scrape-off layer (SOL) region outside the separatrix, magnetic field lines are diverted into a divertor chamber where they intersect a target plate near a strike point. As the interaction regions between the confined plasma and the solid surfaces of the surrounding vessel, the SOL and divertor play a crucial role in the performance of the reactor.

In the present design of DEMO [3, 4], the power carried by charged particles from the confinement region into the SOL will be about 150 MW. Since the parallel transport along the magnetic field line is orders of magnitude larger than the one perpendicular to the field line, most of the power is transported to the divertor chamber in the SOL characterised by the power fall-off length λ_q. Based on the scaling developed in the present-day devices, the predicted value of λ_q for DEMO would be as small as 0.8 mm [4, 5]. This means that most of the power will be deposited on a small 'plasma-wetted' area at the

divertor target if there are not other dissipative processes active. However, in order to guarantee a sufficiently long lifetime of the plasma-facing components (PFCs) at the target, the maximum power flux density on the PFCs is limited to below 5 MW/m^2 [4]. This limit leads to a power exhaust problem which is one of the most critical challenges in fusion reactor research. In order to achieve such a reduction of the power load at the target, more than 95 % of the power should be dissipated in the SOL and divertor before reaching the target. In experiments in the present-day devices, such a highly radiative regime is challenging and can lead to instabilities and confinement degradation [4, 6]. In addition, the ion particle flux at the divertor target in DEMO is expected to be much higher than that in the present-day devices, and the power flux caused by the recombining ions at the target alone can exceed the material limits [6]. Thus, a 'detached' divertor regime [7, 8, 9, 10] is required, in which volumetric processes and cross-field transport reduce also the particle fluxes before reaching the target. For the reasons mentioned above, divertor concepts, which can achieve a higher radiative power fraction and a higher degree of divertor detachment without confinement degradation, are strongly required.

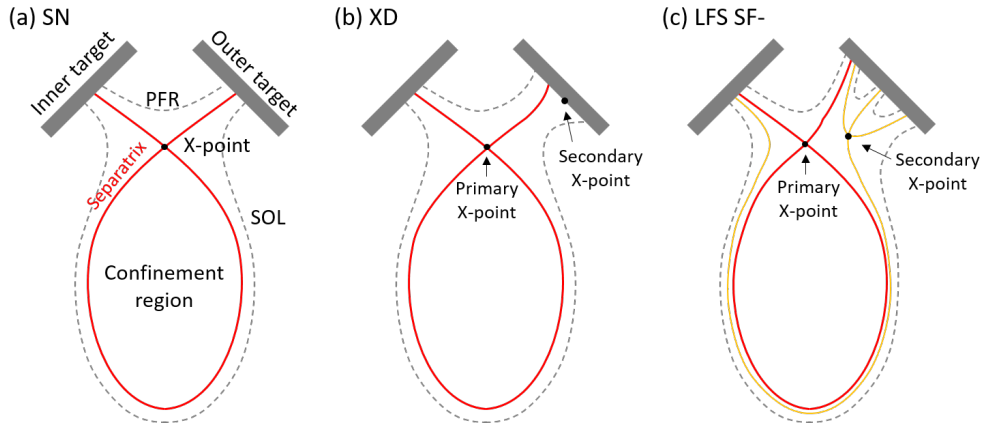

FIGURE 1.1: Divertor configurations. (a) Single null divertor, (b) X-divertor, (c) snowflake divertor.

The divertor configuration development aiming at optimising power and particle exhaust has been an active area of fusion research since the 1970s [11]. Different from the single null divertor configuration, many alternative divertor configurations, such as the X-divertor and snowflake divertor, were proposed. The goal of these configurations is to increase the plasma-wetted area at the divertor target and/or to increase the dissipative channels or the cross-field transport.

In X-divertor configurations [12], the magnetic field lines are flared in the divertor region by creating another X-point near the target (see Fig. 1.1 (b)). The field lines diverge in the poloidal plane as moving from the main plasma

X-point to the target, while the lines converge in a single null configuration. Such a significant poloidal flux expansion is considered to have potential in increasing the plasma-wetted area.

In snowflake divertor configurations [13], the original idea is to create a second-order poloidal field null (the poloidal field and its gradient are both zero) with additional poloidal magnetic field coils, which creates a hexagonal separatrix and four strike lines at the divertor targets. For practical reasons, however, it is hard to achieve an exact second-order null. The second-order null splits into two nearby first-order nulls (see Fig. 1.1 (c)), and the magnetic field properties are determined by their simultaneous actions. A weak poloidal field area can be generated around the nulls if the distance between them is small enough [14]. One of the potential benefits of a snowflake configuration is the capability to distribute the power and particle flux between all/part of the strike points. In addition to this, the weak poloidal field around the nulls is supposed to modify the power and particle transport in the divertor region. In the past ten years, a series of experiments in snowflake configurations were carried out at the TCV tokamak [15, 16, 17]. The power flux sharing between the two strike points at the outer target and higher radiative power fraction were observed.

The ASDEX Upgrade (AUG) tokamak [18] at IPP Garching is a device with high heating power capacity and a full-tungsten divertor and first wall. It is a key device for the research of tokamak physics and in particular for the power exhaust problem towards future fusion reactors. Recently, a modification of the upper divertor is prepared in AUG to study various alternative divertor configurations experimentally in a machine with a high heating power compared to its size.

For the planning of the divertor upgrade, the 3D edge transport code EMC3-EIRENE was applied [19]. However, volumetric recombination and drifts were not implemented in the code during the planning phase of the upgrade. These two processes were required to reproduce important features of the experimentally diagnosed SOL plasma in the single null configuration in AUG [20, 21], e.g. divertor detachment. In addition to this, drift effects are expected to play an important role in the power distribution among the strike lines in the snowflake configuration [11]. For example, in EMC3-EIRENE simulations for the snowflake configuration in the TCV tokamak, the modelling without drifts [16, 22] underestimated the heat flux at the secondary strike point by about one order of magnitude compared to experimental measurements [15]. In a subsequent work [23], a qualitative explanation for the activation of the secondary strike point was found by computing drift terms on the plasma background given by EMC3-EIRENE. However, a quantitative and self-consistent simulation is still missing. Other 2D transport codes such as

UEDGE and SOLEDGE2D have also been used to model snowflake-like configurations in the tokamaks NSTX [24], NSTX-U [25] and HL-2M [26]. These simulations generally found that, under comparable conditions, the use of the snowflake divertor allows a significant reduction of the maximum power flux at the target [14]. However, these studies were only considering the strike lines directly connected to the upstream SOL. Therefore, these studies could not assess the cross-field transport across the additional separatrix branches and the 'activation' of additional strike points. For the reasons mentioned above, simulations of the snowflake configuration with volumetric recombination, drifts and a full geometry including all strike points are strongly required.

The SOLPS (Scrape-Off Layer Plasma Simulation) code [27, 28] contains a comprehensive description of the drifts and the atomic and molecular processes including volumetric recombination. It is widely applied in divertor studies, especially for the investigation of divertor detachment, and is able to reproduce results from experiments [21, 29, 30, 31]. The SOLPS code has been the workhorse for the design of the ITER divertor and is considered as one of the principal modelling tools for the DEMO divertor [28]. However, because the standard tool to generate the numerical grid of the SOLPS package is not able to generate grids for snowflake topology, such a configuration was never simulated by SOLPS before this thesis.

Numerical simulations are an essential part of the power exhaust research. Modelling for the alternative divertor configurations can contribute to a better insight into their potential in reducing divertor target load and facilitating the divertor detachment. In this thesis, the complete snowflake geometry was implemented in the SOLPS code for the first time. This made it possible to simulate plasma conditions in the snowflake configuration to study its effects on the power exhaust and to predict the performance of the future upper divertor based on the present experiments in AUG.

The thesis is organized as follows. Chapter 2 briefly introduces basic concepts in tokamak research and the ASDEX Upgrade tokamak for which the numerical simulations were carried out and where the experiments were performed. Chapter 3 presents the divertor physics related to the power and particle exhaust. Chapter 4 introduces the SOLPS code package and the implementation of the snowflake geometry. Chapter 5 shows the SOLPS simulation results comparing between the single null, X-divertor and snowflake divertor configurations. In chapter 6, the evolution of divertor detachment in the snowflake configuration is studied by scanning impurity seeding rates in the simulation. In chapter 7, the SOLPS code is applied to predict the plasma conditions in the future upper divertor in AUG based on the experimental measurements made in the present single null divertor. In chapter 8, the effect of drifts on the divertor conditions in the snowflake divertor is presented.

Chapter 2

Introduction

2.1 Controlled thermonuclear fusion

Controlled thermonuclear fusion is a potential source of clean, safe and virtually unlimited energy. In a thermonuclear fusion process, two lighter atomic nuclei combine to form a heavier nucleus and release energy. A technologically feasible reaction is that a pair of deuterium (D) and tritium (T) nuclei produces a helium nucleus (alpha particle) and a neutron, releasing a total energy of 17.6 MeV [32],

$$\mathrm{D} + \mathrm{T} \longrightarrow {}^{4}\mathrm{He}\ (3.5\ \mathrm{MeV}) + \mathrm{n}\ (14.1\ \mathrm{MeV}). \tag{2.1}$$

In order to overcome the electrostatic barrier and trigger the fusion reaction, the kinetic energy of D and T should be sufficiently high and temperatures of the order of 10 keV are needed. Under such conditions, the fuel atoms are ionized and form a plasma.

Devices designed to harness the controlled thermonuclear fusion energy are called fusion reactors. So far, there are two major approaches to the fusion reactor research related to magnetic confinement and inertial confinement of the plasma. The latter uses high-energy laser beams to heat and compress a fuel target in the form of a pellet. In this thesis, we focus on the magnetic confinement one.

Ignition is a basic requirement for a fusion reactor, meaning that the temperature required for fusion reactions is self-sustained without external heating. This requires sufficiently high temperature (T), high density (n) and long energy confinement time (τ_E). For the D-T reaction, the criterion for ignition is given by

$$nT\tau_E > 3 \times 10^{21}\ \mathrm{m}^{-3}\cdot\mathrm{keV}\cdot\mathrm{s}, \tag{2.2}$$

which is known as the Lawson criterion [33].

2.2 Tokamak

The tokamak concept is one of the leading approaches to magnetic confinement fusion. The world's largest experimental reactor under construction, ITER, and its planned successor, DEMO, are both designed based on the tokamak concept. In a tokamak device, hot plasma is confined in a toroidal vessel by a magnetic field (see Fig 2.1). The geometry of the torus is described by its major radius (R_0) and minor radius (a). There are two principal components of the magnetic field: the toroidal and the poloidal field B_ϕ and B_θ, respectively. The resulting total magnetic field $\vec{B}$ is helical.

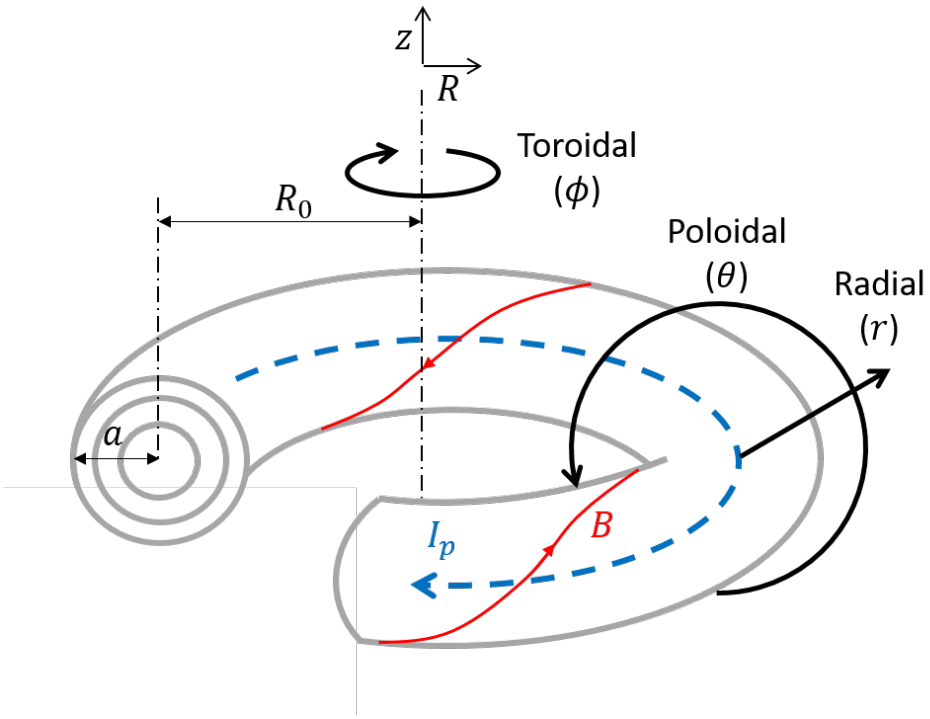

FIGURE 2.1: The magnetic field structure in a tokamak.

The toroidal magnetic field B_ϕ is created by external magnetic coils (TF coils, see Fig. 2.2 (a)). According to Ampère's law, B_ϕ falls off along the major radius coordinate, $B_\phi(R) \propto 1/R$. Denoting the toroidal field at the plasma centre ($R = R_0$) as B_0, $B_\phi(R)$ can be written as

$$B_\phi(R) = \frac{f_{pol}}{R}, \tag{2.3}$$

where $f_{pol} \approx R_0 B_0$. The region with $R < R_0$ is called the high-field side (HFS) since B_ϕ is higher than B_0, while the one at $R > R_0$ is called the low-field side (LFS).

Ions and electrons drift in opposite directions in a magnetic field with a

gradient and/or curvature. If there is only the toroidal field in the tokamak, the separation of ions and electrons will form an vertical electric field and result in particle losses via E×B drift. The existence of a poloidal field B_θ leads to the helical total field lines, which connect the upper and lower regions in the plasma and reduce the charge separation via current along the field lines called Pfirsch-Schlüter current [32]. The poloidal magnetic field is created by the toroidal plasma current I_p as well as by poloidal field (PF) coils (see Fig. 2.2 (a)) used for plasma shaping and control.

The equilibrium condition in such magnetic fields requires that the magnetic force balances the force due to the plasma pressure [32],

$$\vec{j} \times \vec{B} = \nabla p \tag{2.4}$$

where $\vec{j}$ is the current density and p the plasma pressure. It is clear from this equation that $\vec{B} \cdot \nabla p = 0$, indicating that there is no pressure gradient along the magnetic field lines [32]. The parallel sound speed in the plasma is typically 10^5–10^6 m/s, and consequently, any imbalance along the magnetic field is removed rapidly. The surfaces of constant pressure are nested (see Fig 2.1) and called magnetic surfaces. The magnetic field lines follow a helical path on these magnetic surfaces as they wind around the torus. The average twist of the magnetic field can be characterized by the so-called safety factor, $q = \langle rB_\phi / RB_\theta \rangle$, which is a measure of the average pitch of the helical field lines [32]. When identifying the magnetic surfaces, it is convenient to introduce the poloidal magnetic flux function Ψ which is determined by the poloidal magnetic flux lying within each magnetic surface and, therefore, a constant on that surface. In the cylindrical coordinate system shown in Fig 2.1, Ψ can be defined as

$$B_R = -\frac{1}{2\pi R}\frac{\partial \Psi}{\partial z}; B_z = \frac{1}{2\pi R}\frac{\partial \Psi}{\partial R}. \tag{2.5}$$

2.3 Divertor and scrape-off layer

In magnetically confined fusion research, a divertor concept was proposed to optimize plasma power exhaust, particle control, impurity source reduction and screening [34, 35, 36, 37].

Figure 2.2 (b) shows a poloidal cross-section of the ASDEX Upgrade tokamak (AUG) with an upper single null (SN) divertor configuration. With currents in the upper divertor coils (see Fig. 2.2 (a)), a poloidal magnetic field null (X-point) is created at a position closer to the plasma than the protruding elements of the surrounding vessel (the so-called limiter). A separatrix crossing the X-point is generated magnetically. Inside the separatrix, magnetic field lines are termed closed and never make contact with the vessel components. In

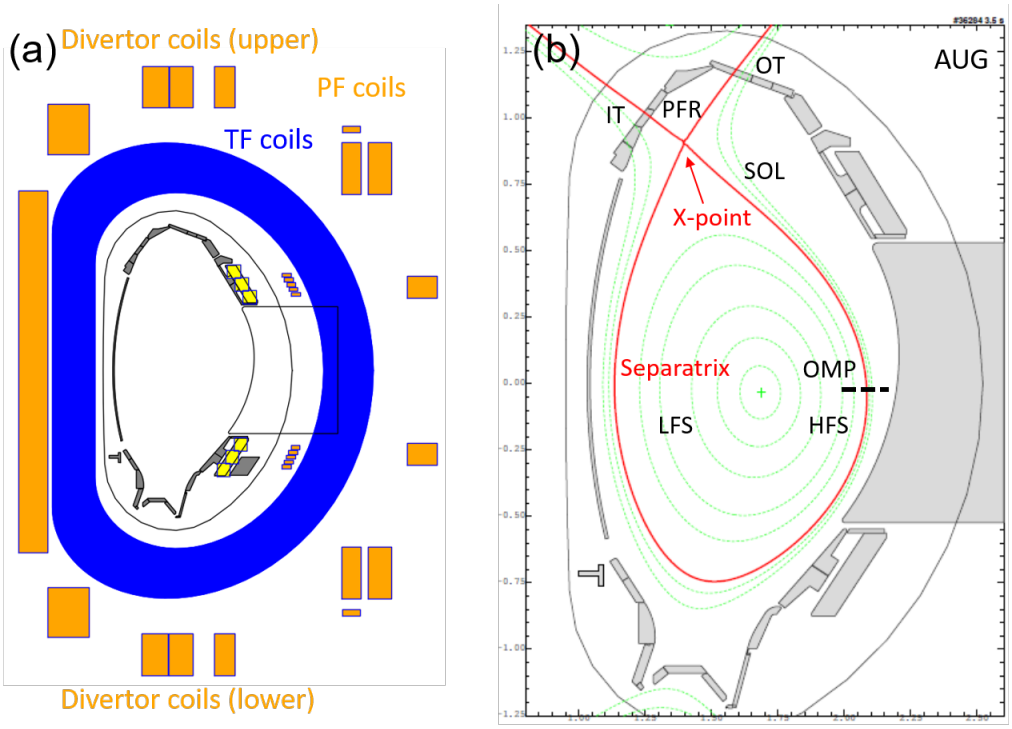

FIGURE 2.2: Poloidal cross-section of the ASDEX Upgrade tokamak. (a) The magnetic field coils. (b) An upper single null divertor configuration.

the scrape-off layer (SOL) region outside the separatrix, magnetic field lines are diverted into a divertor chamber and intersect a target plate. Most of energy and particles lost from the confined plasma into the SOL flow to the divertor targets along the magnetic field lines. The divertor targets act as a separated plasma-material interface, so the sputtered impurities from the target can be controlled in the divertor region before entering the core. The target located on the high-field side (HFS) is called the inner target (IT), and the one on the low-field side (LFS) the outer target (OT). The part of the separatrix from the X-point to the target and its intersection with the target are called divertor leg and strike point (SP), respectively. The region between the divertor legs is called the private flux region (PFR). The outer mid-plane (OMP) is the horizontal plane at the height of the magnetic axis on the low-field side.

The coordinate ρ_{pol} is commonly used to locate magnetic surfaces. It is defined as

$$\rho_{pol} = \sqrt{\frac{\Psi - \Psi_0}{\Psi_{sep} - \Psi_0}} \tag{2.6}$$

where Ψ_0 and Ψ_{sep} are the poloidal magnetic fluxes at the plasma centre and the separatrix, respectively. The coordinate ρ_{pol} satisfies $\rho_{pol} = 0$ at the plasma centre, $0 < \rho_{pol} < 1$ in the confinement region, $\rho_{pol} = 1$ at the separatrix and

$\rho_{pol} > 1$ in the SOL.

2.4 Plasma confinement

As introduced in section 2.1, the energy confinement time is a key parameter of the performance of a fusion reactor. In present tokamak devices, three categories of confinement regimes were found [32]. The first one relates to ohmically heated plasmas. The second and third regimes relate to plasmas with additional heating. According to the degree of confinement, they are called low (L) and high (H) confinement modes. The H-mode was first discovered at the ASDEX tokamak [38] and subsequently observed at many tokamaks. When the heating power exceeds a certain threshold, an abrupt transition to H-mode occurs, and the confinement time is typically twice of that in L-mode. In H-mode, an increased pressure gradient is found at the edge of the plasma (see Fig. 2.3). The mechanisms for the formation of H-mode have not been fully understood. A widely held view is that the strong shear flow at the edge suppresses the radial turbulent transport and establishes an edge transport barrier. ITER and DEMO are designed to be operated in H-mode.

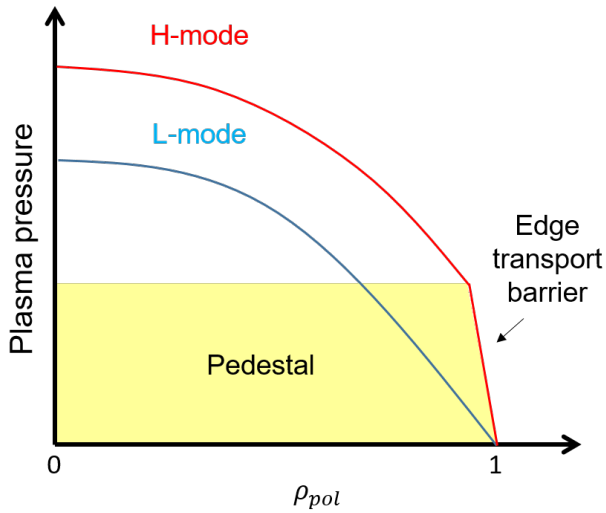

FIGURE 2.3: Schematic plasma pressure profiles in L-mode and H-mode.

The discovery of the H-mode was accompanied by the observation of quasi-periodic bursts in signals of magnetic pick-up coils and soft X-ray diodes [38]. This phenomenon is called Edge Localized Mode, ELMs. It is caused by magnetohydrodynamic (MHD) instabilities in the edge of the plasma, which lead to cyclic relaxations of the pressure gradients. ELMs cause some deterioration of confinement and expel particles and energy into the SOL. This leads to

transient particle and heat loads on the divertor targets. In present-day tokamaks, three types of ELMs are observed [1]. Type-I ELMs refer to the case where the bursts are single and large, while type-III ELMs are continuous and small. ELMs are beneficial for expelling impurities from the confined plasma, however, ELMs can also lead to challenging heat loads on the divertor targets. In DEMO, it is likely mandatory to avoid the type-I ELMs [2].

2.5 The ASDEX Upgrade tokamak

The upgraded Axis-Symmetric Divertor EXperiment tokamak [18], shortly ASDEX Upgrade (AUG), is a tokamak device operated by the Max-Planck Institute for Plasma Physics in Garching, Germany.

The operational parameters of AUG are given in Table 1. The heating system consists of the intrinsic ohmic heating and the auxiliary heating systems including neutral beam injection (NBI), electron cyclotron resonance heating (ECRH) and ion cyclotron resonance heating (ICRH) [39]. With this high heating power capacity and a full-tungsten divertor and first wall, ASDEX Upgrade is a key device for the research of tokamak physics and in particular for the power exhaust problem towards future fusion devices.

Item	Value
Major radius	1.65 m
Minor radius	0.50 m
Plasma Volume	14 m^3
Plasma surface	42 m^2
Pulse length	<10 s
Plasma current	0.4–1.6 MA
Ohmic heating power	≈1 MW
NBI heating power	20 MW
ICR heating power	6 MW
ECR heating power	4 MW

TABLE 2.1: Values for characteristic plasma parameters for different discharges.

ASDEX Upgrade is equipped with various diagnostics for the investigation of edge, SOL and divertor physics. Here we briefly introduce the diagnostics related to this thesis.

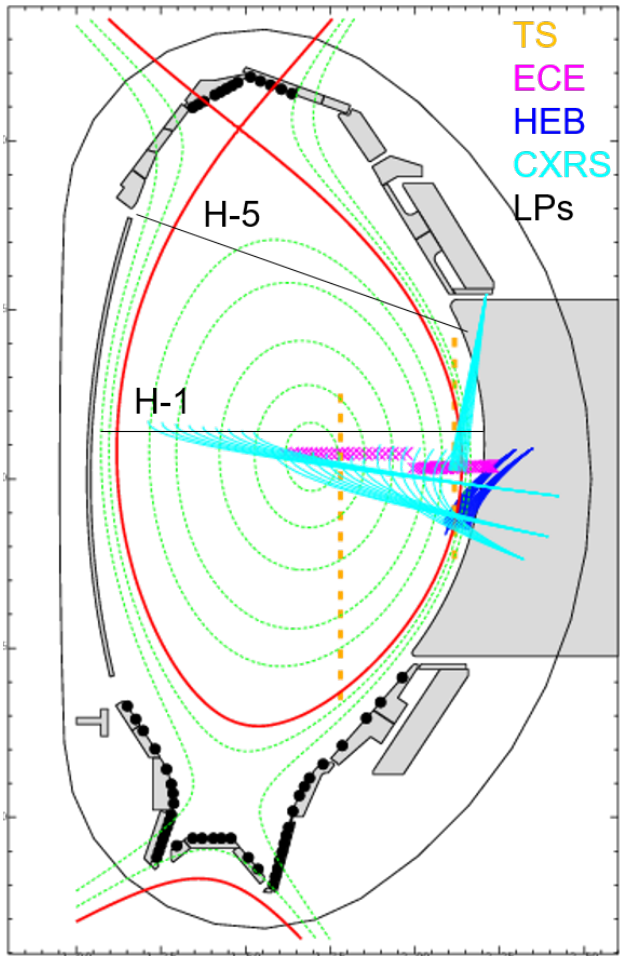

FIGURE 2.4: Diagnostics in ASDEX Upgrade.

Interferometry

Interferometry measures the line-averaged density along a line of sight (LOS). The phase speed of electromagnetic waves in plasma relates to the plasma density. The line-averaged density is obtained by measuring the phase shift between a laser beam passing through the plasma and a reference one bypassing the plasma. In AUG, interferometry measures the line-averaged density along five LOS (H-1 to H-5). The 'H-1' and 'H-5' signals (see Fig. 2.4) are usually used for the core and edge line-averaged densities, respectively.

Bolometers

Bolometers measure the integrated radiation along a line of sight. In AUG, there are two bolometer systems: foil bolometers with 128 LOS and diode bolometers with 256 LOS [40]. The radiation from the plasma heats the foil. The foil bolometers calculate the radiation power by measuring the resistance

of the temperature-sensitive detector covered by the foil. The diode bolometers measure the photocurrent of absolute extreme ultraviolet (AXUV) emission, which is approximately proportional to the incoming radiation power. The network of LOS covers the main chamber volume. By applying a tomographic reconstruction or Abel transform techniques, the spatial distribution of radiation in the 2D poloidal plane can be calculated.

Thomson scattering

The Thomson scattering (TS) diagnostic [41] is widely applied in plasma physics research to measure the electron density and temperature exactly at the same position by detecting the laser light scattered by the electrons in the plasma. If the wavelength of the incident light is much smaller than the Debye length, the spectral density of the scattered light can be assumed proportional to the electron velocity distribution. The electron density is derived from the total intensity of the scattered light and the electron temperature from the Doppler broadening of the spectrum. In AUG, there are two vertical Thomson scattering systems for measuring the core and edge regions (see Fig 2.4). The temporal and spatial resolution in radial direction of the core system are 8.3 ms and 25 mm, respectively. Those of the edge system are 12.5 ms and 3 mm, respectively. The relative systematic errors are 7 % [42, 43].

Electron cyclotron emission radiometer

The electron cyclotron emission (ECE) diagnostic is employed to measure the electron temperature. The optically thick plasma in the confinement region can be considered as a black body. The power radiated at the resonance frequency depends on the electron temperature at the electron cyclotron resonance location. The lth harmonic of the electron cyclotron frequency ($\omega_{c,e}^{l} = \frac{leB}{m_e}$) depends on the local magnetic field. Since the magnetic field decays approximately as $1/R$, each frequency channel can be uniquely mapped to a radial location. Hence, the radial temperature profile can be obtained. In AUG, the temporal and spatial resolution of the ECE system are 32 μs and 5 mm, respectively [44].

Helium beam spectroscopy

The thermal helium beam emission line ratio spectroscopy (HEB) measures the electron density and temperature in the edge and SOL regions simultaneously. The neutral helium is injected locally into the plasma by a piezo valve, while measuring the emission intensities at different wave lengths. From the different line ratios and a collisional-radiative model, the underlying electron

temperature and density can be reconstructed. In AUG, the temporal and spatial resolution of the HEB system are 2.3 ms and 3–7 mm, respectively [45].

Charge-exchange recombination spectroscopy

The charge-exchange recombination spectroscopy (CXRS) measures the density, temperature and fluid velocity of impurity ions. The charge exchange collision between a fully stripped impurity ion and a fast neutral from neutral particle heating beams produces an impurity ion with one electron, a so-called hydrogen-like impurity ion. By measuring the line radiation of these ions, the ion density, temperature and velocity can be derived from the intensity, Doppler broadening and Doppler shift of the spectrum, respectively. Impurities of boron, nitrogen, carbon and helium are commonly used for CXRS measurements. In AUG, there are two main CXRS systems. The 'core' system measures inside the confinement region with lines of sight oriented in the toroidal direction. The 'edge' system covers the region near the separatrix with two spectrometers to estimate the poloidal and toroidal velocity components at the same time. The temporal resolution of the core system is 3.5 ms and the spatial one in radial direction 20–25 mm, respectively. Those of the edge system are 1.9 ms and 5 mm, respectively [46].

Divertor Langmuir probes

Langmuir probes (LP) are employed to measure the ion saturation current and the electron temperature at the divertor targets. So called single probes apply a voltage sweep to a single electrode exposed to the plasma measuring the current-voltage (I-V) characteristics in the plasma sheath. Since the shape of the I-V curve is determined by the plasma particle fluxes and the electron temperature at the sheath entrance, these plasma quantities can be derived by fitting the measured data to a theoretically derived curve. In AUG, triple Langmuir probe arrays are used [47]. The three probes at each position measure three points on the I-V curve simultaneously allowing a substantially higher temporal resolution (40 μs) compared to the single probe with a voltage sweep. The poloidal separation of the Langmuir probes is 20–30 mm and the extension of the collectors is 5 mm [48].

Thermography

The target thermography system diagnoses the heat fluxes onto the divertor target. The infrared photon flux reaching the detector relates to the temperature at the target material surface that the detector facing to. The target heat

flux can be derived from the temporal evolution of the surface temperature by solving the heat diffusion equation for the target with the 2D heat transport code THEODOR [49]. In AUG, the temporal and spatial resolutions of the infrared system are 1 ms and 0.6 mm, respectively. The temporal resolution also depends on the spatial coverage. It is important to keep in mind that the measured power fluxes can convolve inter-ELM and ELM heat loads at high ELM frequencies. Reflections and volume radiation can be an issue for the data evaluation [50].

Chapter 3

Divertor physics

In present-day and planned tokamak devices, the divertor is the main interface between the confined plasma and the solid materials surrounding it. It plays an important role for power and particle exhaust and impurity control. The divertor conditions directly influence the operation and performance of the device. In the divertor region, the plasma parameters (e.g. density and temperature) depend on the combination of the plasma-material interaction, the power and particle transport and the volumetric processes. This chapter introduces the divertor physics related to the power exhaust problem. Section 3.1 introduces the theory of the electrostatic sheath forming in front of the target. Section 3.2 shows the energy transport in the SOL and divertor regions. Section 3.3 discusses the divertor regimes including divertor detachment. Section 3.4 introduces fluid drifts in the SOL and divertor. Section 3.5 introduces the alternative divertor configurations proposed to mitigate the power exhaust problem.

3.1 Sheath theory

In front of a plasma-material interface, a layer called Debye sheath [51] plays an essential role in the particle and power transport. In magnetized plasma, electrons and ions move freely along the magnetic field while making a gyro motion in the plane perpendicular to the field. Since the electron mass is much smaller than the ion mass, the thermal velocity of electrons is larger for a given temperature. At the interface of plasma and a material surface, the larger mobility of electrons results in an accumulation of negative charges at the surface. The electric potential drops substantially ($\Delta\Phi \sim 3T_e$) inside the sheath in front of the surface, as shown in Fig 3.1. This potential drop accelerates ions towards the surface and repels electrons so that the outflux of electrons and ions becomes ambipolar. The width of the sheath is of the

order of the Debye length. The Bohm criterion [51] requires that the ion fluid velocity perpendicular to the surface at the sheath entrance should be at least the local sound speed of $c_s = \sqrt{(T_e + \gamma_i T_i)/m_i}$ otherwise no static solutions can be found for the sheath. Therefore, a presheath is necessary for the acceleration of ions to meet this criterion. In cases with a magnetic field at oblique angles of incidence at the surface, the Bohm-Chodura criterion [52] should be used, which introduces a magnetic presheath of the dimension of the ion gyroradius. At the entrance of this magnetic presheath, the ion velocity parallel to the magnetic field has to reach or exceed the local sound speed. The ions are accelerated further in the magnetic presheath to ensure that the velocity component perpendicular to the surface fulfils the Bohm criterion at the entrance of the Debye sheath.

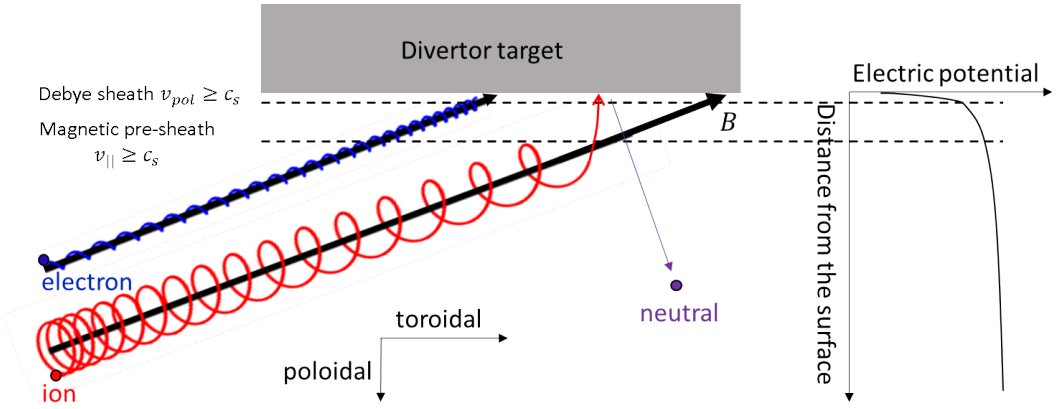

FIGURE 3.1: The sheath structure.

Ions hitting the material surface are neutralized. Except for a small portion retained inside the component, most of the formed neutrals are reflected or re-emitted back to the plasma. The recycled neutrals are either removed by pumps or ionized again as plasma particle sources. This self-sustaining phenomenon is called recycling.

3.2 Power transport in the SOL and divertor

In a magnetized plasma, the gyro-motion of ions and electrons leads to a strong anisotrophy of the transport. The parallel transport along the magnetic field line is orders of magnitude larger than the one perpendicular to the field line.

In the direction parallel to the magnetic field line, the two-fluid assumption is widely used for describing the transport in the SOL. The parallel heat flux density can be written as

$$q_{\parallel} = \sum_{a=i,e} \left[\left(\frac{1}{2} m_a v_a^2 + \frac{5}{2} T_a \right) n_a v_a - \hat{\kappa}_a T_a^{5/2} \nabla_{\parallel} T_a \right] \tag{3.1}$$

where $m_{i,e}$ are the ion and electron masses, $v_{i,e}$ the fluid velocities, $n_{i,e}$ the densities, $T_{i,e}$ the temperatures and $\hat{\kappa}_{i,e} T_{i,e}^{5/2}$ the Spitzer-Härm heat conduction coefficients of electrons and ions. The first term on the r.h.s is the convective heat flux and the second the conductive one.

The connection length L_c is an important parameter for the parallel transport in the SOL. It is defined as the length of the magnetic field line from the upstream position (e.g. at the outer mid-plane) to the divertor target,

$$L_c = \int_{OMP}^{target} \frac{\sqrt{B_\phi^2 + B_\theta^2}}{|B_\theta|} dl \tag{3.2}$$

where dl is the poloidal lenth element. Apart from the poloidal length of the field line, the connection length also depends on the radio of B_ϕ to B_θ. It is longer in the flux tube in close vicinity of the separatrix due to the weak poloidal field near the X-point.

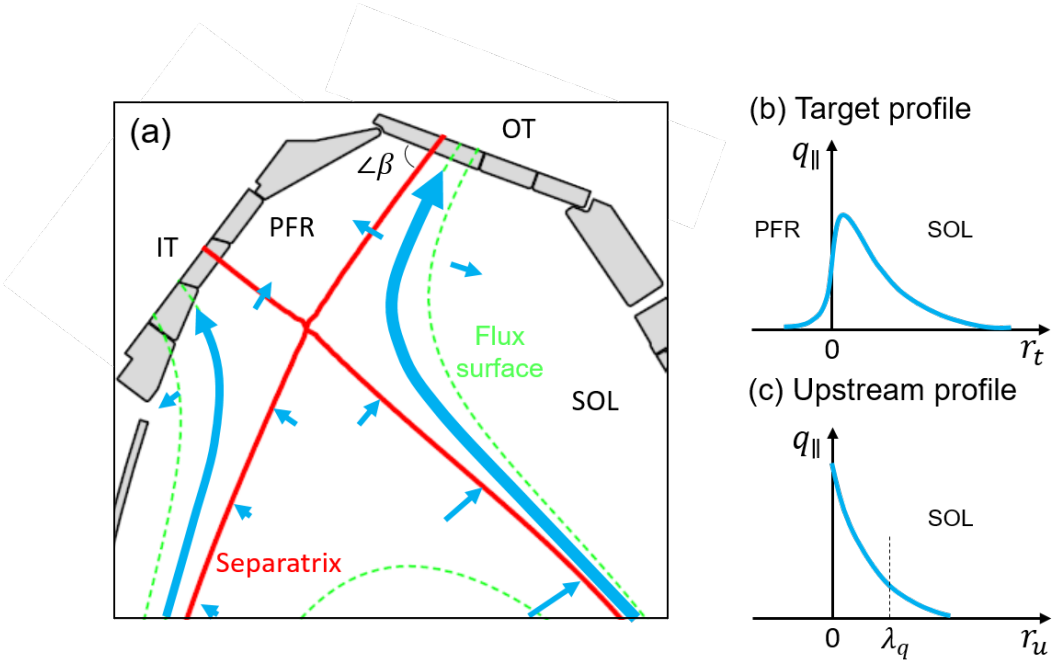

FIGURE 3.2: (a) Heat transport in the SOL. The radial profiles of the heat flux at the (b) divertor target and (c) the upstream position.

The existence of the X-point also causes poloidal magnetic flux expansion in the SOL (see Fig. 3.2 (a)). The expansion ratio at the divertor target with

respect to the upstream position can be estimated by

$$f_x = \frac{\delta r_t}{\delta r_u} = \frac{B_{\phi,tar}/B_{\theta,tar}}{B_{\phi,u}/B_{\theta,u}} \tag{3.3}$$

where δr_u and δr_t are the distances between two flux surfaces at the upstream position (e.g. the outer mid-plane) and the target, respectively.

In the direction perpendicular to the magnetic field line, transport of a scale larger than the gyroradius can be caused by diffusion, drifts, charge exchange collisions and turbulent events. Plasma particles and power in the confinement region are transported radially across the separatrix into the SOL. Except for a small fraction transported radially further to the chamber wall, most of the particles and the power are transported to the divertor chamber along the magnetic field lines. At the upstream position (e.g. the outer mid-plane), the parallel power flux decays exponentially in the radial direction (see Fig. 3.2 (c)),

$$q_{\parallel,u}(r_u) \propto e^{-r_u/\lambda_q}, \tag{3.4}$$

where r_u is the radial distance from the separatrix at the upstream position and λ_q is a characteristic power fall-off length. In AUG, typical values for λ_q are 1.2–2.9 mm in attached H-modes and 2.8–5.2 mm in attached L-modes [53]. Based on the scaling developed in the present-day devices, the predicted λ_q for DEMO would be as small as 0.8 mm [4, 5].

In the divertor chamber, a part of the power is transported radially into the private flux region (PFR) and the far SOL when travelling towards the target (see Fig. 3.2 (a)). Taking into account such a competition between parallel transport and the radial cross-field transport, the radial profile of the parallel power flux at the target can be written as a convolution of an exponential function with the power fall-off length λ_q and a Gaussian function of a width related to the cross-field diffusive transport $S \approx \sqrt{4n\chi_\perp\tau}$ [4, 5], where $\chi_\perp$ is the perpendicular heat transport coefficient and τ the transport time from the X-point to the target:

$$q_{\parallel,tar}(r_t) = \frac{P_{SOL} f_{tar}(1-f_{dis})}{2\pi R_t \lambda_q \sin\theta_u} e^{-\frac{r_t}{f_x \lambda_q}} \otimes \frac{1}{\sqrt{\pi} f_x S} e^{-\left(\frac{r_t}{f_x S}\right)^2} \tag{3.5}$$

The so-called divertor spreading factor S is typically of the order as λ_q. P_{SOL} is the power across the separatrix into the SOL, f_{tar} the power fraction to the specific target, f_{dis} the power dissipation fraction in the SOL and divertor, R_t and r_t the major radius and radial distance to the separatrix at the target, $\sin\theta_u = |B_{\theta,u}/B_u|$ the magnetic pitch at the upstream position.

In power exhaust studies, one of the most important parameters is the maximum power flux density perpendicular to the target. It can be estimated

by

$$q_{\perp,max} \approx \frac{P_{SOL} f_{tar}(1 - f_{dis}) \sin\beta}{2\pi R_t f_x \lambda_{int}} \tag{3.6}$$

where β is the angle between the divertor leg and the target (see Fig. 3.2 (a)) and λ_{int} is the integral power decay length [54],

$$\lambda_{int} = \frac{1}{q_{max}} \int q \mathrm{d}r \approx \lambda_q + 1.64S. \tag{3.7}$$

In the present design of DEMO [3, 4], the power leaving the confinement region into the SOL, P_{SOL}, will be about 150 MW. Substituting the designed value for DEMO ($R_t \approx 9$ m, $\lambda_q \approx 0.8$ mm, $S \approx 1$ mm, $f_x/\sin\beta \approx 5$) into Eq. 3.6 and assuming that 70 % of P_{SOL} is transported to the divertor with a distribution between the outer and inner targets $f_{tar}^{OT} : f_{tar}^{IT} = 2 : 1$ [55], one obtains an estimate of the peak power flux density at the outer target in DEMO, $q_{\perp,max}^{OT} \approx 100(1 - f_{dis})$ MW/m^2.

In order to guarantee a sufficiently long life time of the plasma facing components at the target, the maximum power flux density on the target must be limited to below 5 MW/m^2 [4]. This means that more than 95 % of the power should be dissipated, e.g. via radiation, before reaching the target. In experiments in present-day devices, such a highly radiative regime is challenging and can lead to instabilities and confinement degradation. In addition, the ion particle flux at the divertor target in DEMO is expected to be much higher than that in present-day devices, and the power flux caused by the recombining ions at the target alone can exceed the material limits. Thus, a detached divertor regime (see section 3.3) is required, in which volumetric processes and cross-field transport reduce the particle fluxes before reaching the target [6].

3.3 Divertor regimes

Travelling along the magnetic field lines, the power and particles are affected by various volumetric processes, including radiation, ionization, charge exchange and volumetric recombination (see Fig. 3.3).

The plasma collisionality ($\nu \sim n/T^{3/2}$) is a crucial parameter in the divertor since it directly relates to the power and particle transport and the volumetric processes. When the collisionality is very low, the conductive heat transport and the volumetric processes are negligible, implying nearly no temperature difference between the upstream position and the target. The convective heat transport is dominant. Particles from the upstream position are accelerated to the local sound speed at the sheath entrance in front of the divertor target.

Given the volumetric particle sources and sinks (e.g. ionization and volumetric recombination) are negligible, the conservation of the particle flux ($\Gamma \sim nv$) implies a lower density at the target compared to the upstream position. Most of the neutral particles recycled at the divertor target escape out of the divertor region without being ionized. Such a situation is called 'sheath limited regime' [56].

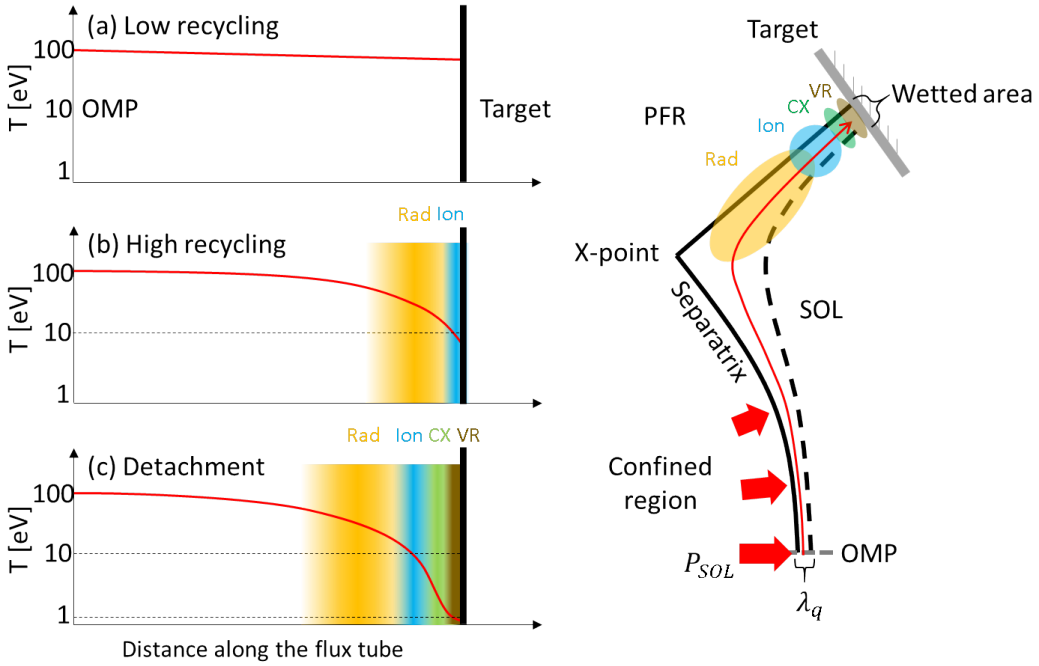

FIGURE 3.3: Parallel temperature profile and volume processes in (a) low recycling, (b) high recycling and (c) detached regimes. The regions of impurity radiation, ionization, charge exchange and volumetric recombination are marked by 'Rad', 'Ion', 'CX' and 'VR', respectively.

For a given divertor geometry, the collisionality in the divertor can be increased either by increasing the upstream density or by inducing a power sink and cooling the plasma. A commonly used method is to seed impurities, e.g. nitrogen (N), neon (Ne), and argon (Ar), into the plasma, which leads to a power loss via line radiation and bremsstrahlung. The impurity radiation power can be calculated by a collisional-radiative model [57, 58],

$$P_{rad} = n_e^2 c_Z L_Z, \tag{3.8}$$

where n_e is the electron density, $c_Z = n_Z/n_e$ the concentration of the impurity specie, L_Z the effective radiative cooling rate which strongly depends on the electron temperature. Figure 3.4 shows the rate L_Z for nitrogen, neon and argon as a function of the electron temperature. Nitrogen radiates mainly

in the region with a temperature around 10 eV, e.g. in the divertor. Neon and argon radiate in the SOL with a temperature of dozens of electronvolt, while argon also radiates partly in the confinement region. In this thesis, we focused on the divertor region, so nitrogen was chosen as the impurity specie in simulations and experiments.

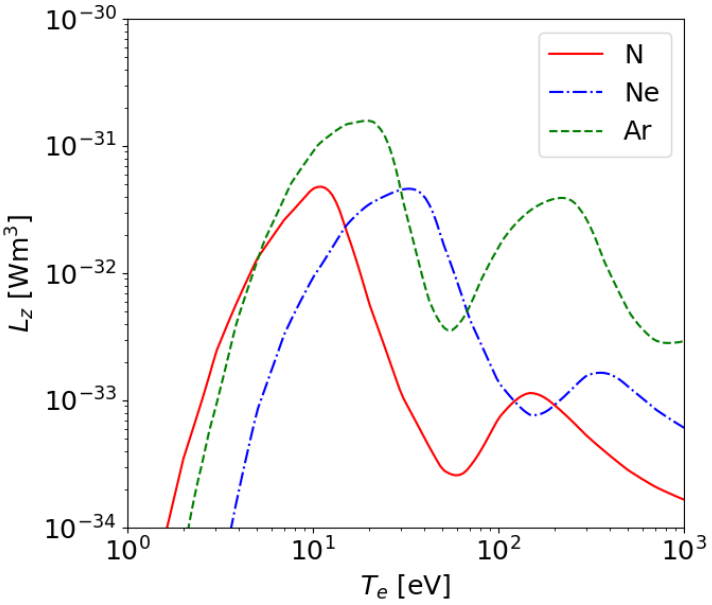

FIGURE 3.4: Effective radiative cooling rates for nitrogen (N), neon (Ne) and argon (Ar) as a function of electron temperature. Taken from the ADAS data base [59].

When the plasma density in the divertor is sufficiently high, the recycled neutral particles are mainly ionized in the region near the target, resulting in an further increased density and decreased temperature there. The newly ionized particles are transported back to the target and recycled again. Recycling and ionization thus promote each other and form a positive feedback. The particle flux to the target is enhanced dramatically and sustained mainly by the ionization source near the target. In the collisional divertor region, the power transport is dominated by conduction, and a significant temperature difference can be found between the upstream position and the target. The high impurity radiation and the deuterium ionization loss in such a high-density and low-temperature divertor can lead to a reduction of the power deposited on to the target. This situation is called 'high recycling regime' or 'conduction limit regime' [56]. In present-day tokamak devices, this regime is usually sufficient to keep the target heat load below the material limits.

When the power to the recycling region is reduced further, there is not enough power to sustain so many ionization reactions. The ionization rate decreases with power, resulting in a reduction of density and particle flux at

the target. Such a roll-over phenomenon of the particle flux is regarded as a characteristic feature of the so-called 'divertor detachment'. The temperature in the divertor region also decreases with power. When the temperature is below 5 eV, charge exchange collisions become dominant and enhance cross-field transport. This cools the plasma further and reduces its pressure, which drops below the upstream one. Such a pressure loss is another characteristic signature of the divertor detachment. When the temperature is around 1 eV, volumetric recombination is setting in, leading to a further reduction of particle flux and pressure at the target.

The degree of detachment (DOD) [60] is defined by comparing the target particle flux obtained in experiment or simulation to that estimated from the Two-point model [56],

$$\mathrm{DOD} = \frac{\Gamma_{TPM}}{\Gamma_{exp/sim}} \approx \frac{cn_u^2}{\Gamma_{exp/sim}} \tag{3.9}$$

where c is a constant and n_u is the electron density at the upstream position. The degree of detachment is much larger than 1 for a detached target [20, 61].

The detachment process is usually inhomogeneous at the target. The higher density in the region near the strike point usually leads to higher recycling there. Thus, the detachment sets in near the strike point and then broadens towards the outer part of divertor. A detachment of the strike point is called 'partial detachment', while a detachment of the whole target is called 'complete detachment' [61, 62].

3.4 Drifts

In the direction perpendicular to the magnetic field lines, drifts of charged particles arise in the presence of a perpendicular or time-varying electric field or a gradient of the magnetic field. The effects of drifts in a tokamak plasma are complex and nonlinear. Experiments have shown that drifts influence the plasma behaviour in many aspects, including the redistribution of the density, the L-H transition power threshold, or the power and particle asymmetries between low-field and high-field sides and the approach to divertor detachment [20, 29, 32].

In the fluid picture, drifts of charged particles are presented by averaged drift velocities. In a static system, there are two types of drift velocities: the diamagnetic and the E×B drift. The diamagnetic drift velocity is charge-dependent and relates to the pressure gradient,

$$\vec{v}_{dia,a} = \frac{\vec{B} \times \nabla p_a}{q_a n_a B^2} \tag{3.10}$$

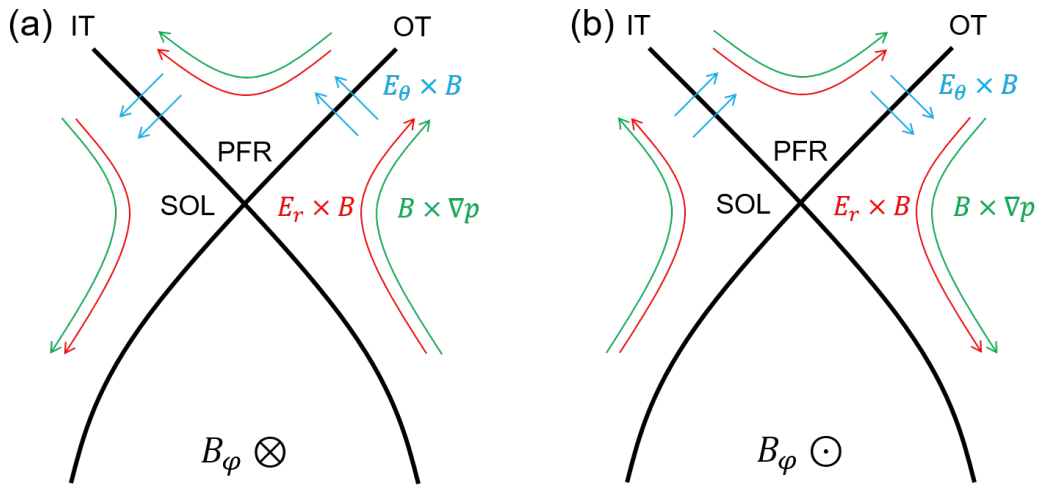

FIGURE 3.5: Directions of diamagnetic ($B \times \nabla p$) and $E \times$B drifts in the SOL and private flux region with (a) forward and (b) reversed toroidal fields.

where p_a, q_a and n_a are the pressure, electric charge and density of the fluid specie. The E×B drift velocity is ambipolar and relates to the electric field perpendicular to the magnetic field line,

$$\vec{v}_{E\times B} = \frac{\vec{E} \times \vec{B}}{B^2} \tag{3.11}$$

In the SOL, the radial and poloidal electric field can be approximated by [56]

$$E_r \approx -\frac{3\nabla_r T_e}{e} \tag{3.12}$$

$$E_\theta \approx -\frac{B_\theta}{B}\left(\frac{0.71\nabla_\parallel T_e}{e} + \frac{\nabla_\parallel p_e}{e n_e}\right) \tag{3.13}$$

Figure 3.5 shows the main directions of diamagnetic and E×B drifts in the SOL and private flux region. In high-recycling and detached divertors, the poloidal drift near the divertor legs can reverse sign due to the changes of temperature and density distributions. In recent years, numerical simulations with drifts activated successfully reproduce part of the high-field-side/low-field-side asymmetries observed in experiments [21, 30, 31]. However, the treatments of numerical instability and missing physics need still to be improved.

3.5 Alternative divertor configurations

The divertor configuration development aiming at optimizing power and particle exhaust has been an active area of fusion research since the 1970s [11]. Different from the standard single null divertor (SN) configuration, many al-

ternative divertor configurations (ADCs) were proposed. These concepts may be able to mitigate the power and particle loads by increasing the plasma-wetted area at the divertor target and modifying the transport and dissipative channels [11]. There are also other means to improve the power and particle exhaust, e.g. divertor closure, target plate electric biasing, liquid metal targets and moving divertor plates [63, 64, 65]. However, these methods are not the main subject of this thesis. Here, we focus on the alternative magnetic configurations.

According to experiments and simulations in the single null configuration, the outer divertor target receives more power and is more difficult to detach [20]. For this reason, the modifications in alternative divertor configurations mainly focuse on the outer divertor. According to Eq. 3.6, there are the following ways to reduce the power flux density at the divertor target: decreasing the power fraction to the outer divertor target f_{tar} by adding additional targets; increasing the power dissipation fraction f_{dis}; increasing the plasma-wetted area at the target via increasing R_t; increasing cross-field transport, and consequently, λ_{int}. In the following sections, we briefly introduce the various alternative divertor configurations proposed in recent years, focusing on the snowflake and X-divertor configurations related to this thesis.

3.5.1 Snowflake divertor

With additional poloidal magnetic field coils, a higher-order poloidal field null can be obtained instead of the standard (first-order) one. The configurations with second and third-order nulls are called snowflake (SF) [13] and cloverleaf [66] configurations. In these configurations, the weak poloidal field around the nulls is supposed to modify the power and particle transport in the divertor region. Snowflake divertors have been implemented in several tokamaks, such as TCV, NSTX, and DIII-D. The cloverleaf configuration has been demonstrated in TCV. More details on the snowflake configuration can be found in the review paper Ref. [14].

Figure 3.6 shows a simple comparison between the single null and snowflake configurations. In the snowflake configuration, the second-order null (the poloidal field and its gradient are both zero) creates a hexagonal separatrix and four divertor legs, reminiscent of a snowflake. In the vicinity of the second-order null, the poloidal magnetic field scales as the square of the distance from the null ($B_\theta \propto r^2$). This leads to the formation of a large area of weak poloidal field near the second-order null.

In practice, it is hard to achieve an exact second-order null. The second-order null rather splits into two nearby first-order nulls, and the magnetic field properties are determined by their simultaneous actions. The weak-field

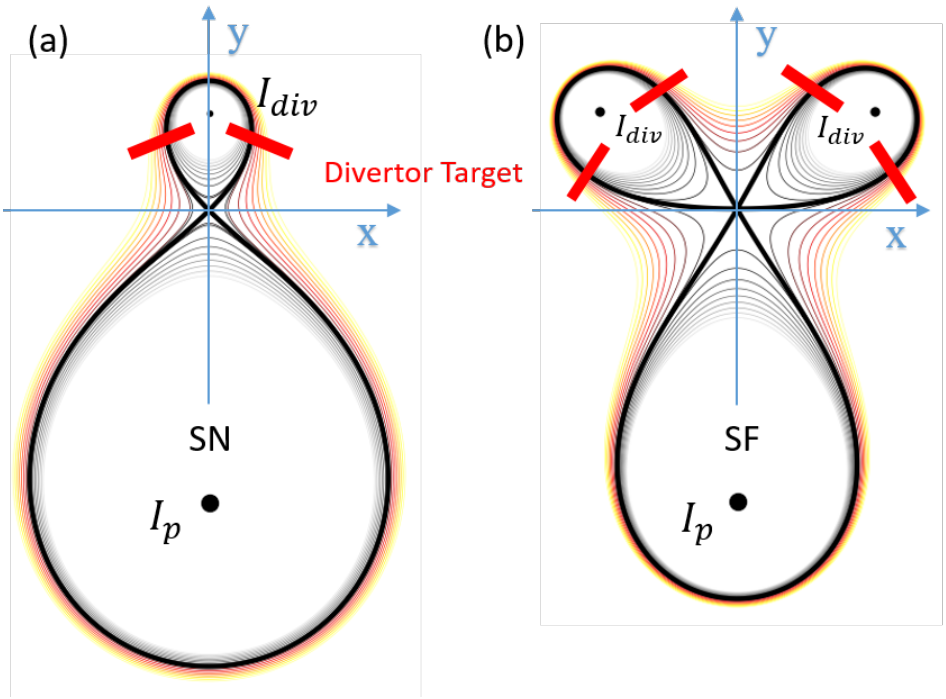

FIGURE 3.6: The magnetic structures in (a) a single null and (b) an exact snowflake configurations.

area can be maintained if the distance between the two nulls is small enough [14]. These two nulls are usually called the primary and secondary X-points. Configurations with a secondary X-point located in the private flux region, high-field side SOL and low-field side SOL of the primary X-point are called snowflake plus (SF^+), high-field side snowflake minus (HFS SF^-) and low-field side snowflake minus (LFS SF^-), respectively (see Fig. 3.7).

One of the potential benefits of a snowflake configuration is the capability to distribute the power and particle flux between the divertor legs. This can occur through a variety of possible mechanisms: drifts, flute-like and ballooning instabilities, axisymmetric convection (a churning mode), and magnetic field stochastization [14]. The sharing of power and particle flux is highly desirable as it allows to fully realize the snowflake divertor potential in reducing divertor target loads and facilitating the divertor detachment.

As mentioned in section 3.2, the power exhaust problem is more serious in the low-field side divertor (outer divertor), so we focus on the low-field side snowflake minus (LFS SF^-) configuration (see Fig. 3.7 (c)) in this thesis. If the distance between the primary and secondary separatrices is less than the power fall-off length λ_q at their upstream positions, the low-field side SOL is split into two parts and connected to two strike points ('SP2' and 'SP4' in Fig. 3.7 (c)). The power to the low-field side divertor can be mainly shared

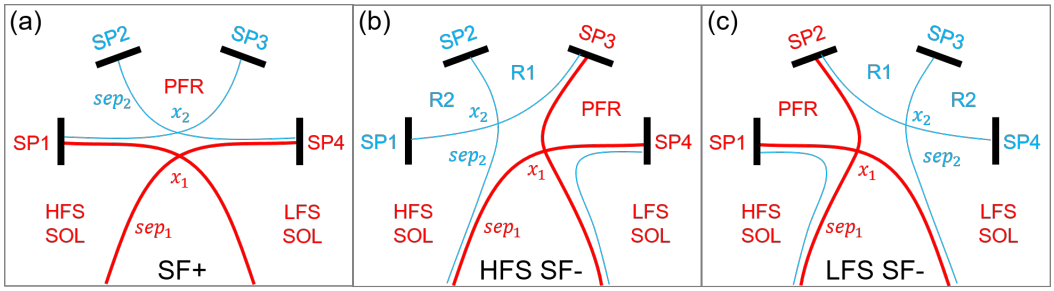

FIGURE 3.7: The geometries of (a) snowflake plus (SF^+), (b) high-field side snowflake minus (HFS SF^-) and low-field side snowflake minus (LFS SF^-) configurations. The primary and secondary separatrices are plotted in red and blue, respectively.

by these two strike points. Two additional private flux regions ('R1' and 'R2' in Fig. 3.7 (c)) are created between the additional divertor legs. Since the primary divertor leg (from the primary X-point 'X_1' to 'SP2') is surrounded by two private flux regions ('PFR' and 'R1' in Fig. 3.7 (c)), additional cross-field transport is expected and can contribute to an increased integral power fall-off length λ_{int}. By choosing a proper distance between the primary and secondary X-points ('X_1' and 'X_2'), the maximum parallel power flux densities ($q_{\parallel,max,SF}$) around the two strike points ('SP2' and 'SP4') can be equal. In this case, λ_{int} is estimated as [19]

$$\lambda_{int,SF} = (\lambda_q + 1.64S)\frac{1 + 5.0S/\lambda_q}{1 + 2.5S/\lambda_q} \tag{3.14}$$

Compared to a single null configuration with the same upstream power fall-off length λ_q, the maximum power flux density can be reduced by a factor of $\frac{1+2.5S/\lambda_q}{1+5.0S/\lambda_q}$ in the LFS SF^- configuration.

As introduced in the previous section, the connection length is a crucial parameter for the transport in the SOL, strongly depending on the poloidal magnetic field. In the snowflake configuration, the dramatically increased connection length in the vicinity of the X-points are supposed to lead to a larger temperature drop between the upstream position and the target. A longer residence time of a certain parcel of plasma on its way to the target could enhance the volumetric processes such as radiation losses [14].

In the past ten years, a series of experiments in snowflake configurations were carried out at the TCV tokamak [15, 16, 17]. For the snowflake plus configuration where the secondary X-point is located in the private flux region of the primary X-point (see Fig. 3.7 (a)), the ratio of the power load on the secondary strike point ('SP3' in Fig. 3.7 (a)) to that on the primary one ('SP4' in Fig. 3.7 (a)) can reach up to 10 %, depending on the distance between

the separatrices. With the similar impurity concentration, up to 15 % more radiation in the snowflake plus configuration than in the single null configuration was found. The radiation region in the snowflake plus configuration is significantly larger [15]. For the LFS SF^- case, the power flux sharing between two strike-points at the outer target was observed. The power fraction and the peak heat flux can be balanced by adjusting the position of the secondary X-point [15]. This is a demonstration of the benefits of the snowflake minus configuration to the snowflake plus and single null configurations [15, 17].

3.5.2 X-divertor

The basic idea behind the X-divertor (XD) configuration [11] is to flare the magnetic field lines in the divertor region, by creating another X-point near the target. This extra X-point is created with an extra pair of poloidal field coils with opposite currents (see Fig. 3.8 (b)). The field lines diverge as moving from the main plasma X-point to the target, while the lines converge in a single null configuration. The significant flux expansion may increase the plasma-wetted area and consequently, reduce the peak power flux at the target. However, the gain of plasma-wetted area is limited by the angle between the magnetic field line and the divertor plate, since the fraction of toroidally wetted-area at the target strongly decreases for shallow field line angles due to the 'fish scale' structure of the target tiles [11, 19].

In the X-divertor configuration, the increased flux expansion and connection length from the primary plasma X-point to the target can also contribute to isolating the plasma better from the divertor target and enhancing the impurity entrainment and radiation in the divertor region while reducing the impurity level in the main plasma. The plasma temperature at the target plate could be substantially reduced, leading to less material erosion and impurity generation [11].

Due to the current in the additional poloidal field coils, a non-axisymmetric variation in the magnetic field is introduced at the divertor plate and large enough to cause 'hot spots' [12]. This may bring additional engineering difficulties in X-divertor configuration.

3.5.3 Other alternative divertor configurations

A configuration with 'multiple standard divertors' may be able to distribute the power among those divertors and thus reduce the power into a specific divertor [67]. The most common configuration of this concept is the double null (DN) configuration with two (upper and lower) standard divertors. The double null configuration is applied in several tokamaks such as ASDEX Upgrade, DIII-

D, and EAST. Triple and quadrupole divertors were also implemented and studied in TCV [68] and PDX [69], respectively.

'Long-legged divertors' can offer a plasma-material interface far away from the main plasmas. Recently, a new long-legged concept called Super-X divertor [70] was proposed by locating the divertor targets at the largest possible radius and introducing a high poloidal flux expansion at the target as in the X-divertor configuration. The Super-X divertor configuration is implementing in the MAST Upgrade tokamak [71, 72]. The larger divertor volume and plasma-wetted area, longer connection length, and better baffling in the Super-X divertor may be able to increase the radiation and momentum loss in the divertor and reduce the power flux and temperature at the target. Meanwhile, it may also stabilize the detachment front far away from the main plasma [11, 71, 72].

3.5.4 Alternative divertor configurations for the divertor in ASDEX Upgrade

At the ASDEX Upgrade (AUG) tokamak, an modification of the upper divertor is currently prepared to study various alternative divertor configurations experimentally in a machine with a high heating power compared to its size.

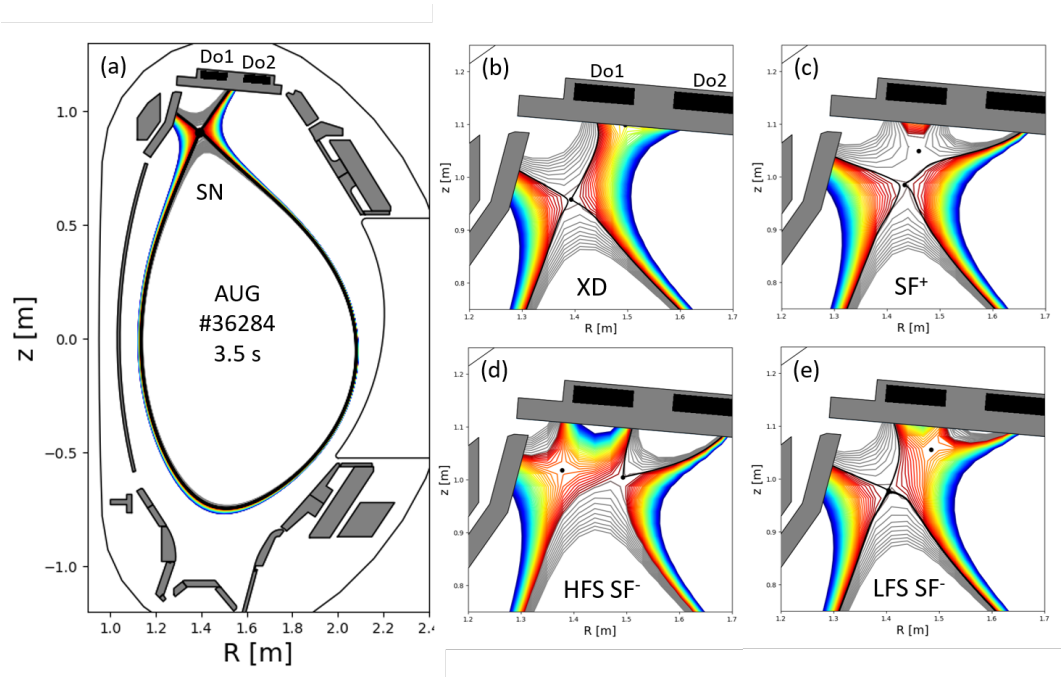

FIGURE 3.8: Various divertor configurations in the future upper divertor in AUG created by the additional poloidal field coils Do1 and Do2. Colors indicate the poloidal magnetic flux function. Reproduced from [19].

By adding a pair of in-vessel coils with opposite currents close to the plasma, a variety of configurations of the upper divertor is possible [19], as shown in Fig. 3.8. By increasing the currents in the coils, the flux surfaces are pulled apart and at some point a secondary X-point forms between the coils and moves towards the main plasma [19]. When this X-point is close to the target, the configuration can be referred as a X-divertor configuration. When the secondary X-point moves inside the plasma, various snowflake configurations (SF^+, HFS SF^- and LFS SF^-) can be achieved depending on the relative position of the secondary X-point and the primary separatrix.

For the planning of this hardware modification the 3D edge transport code EMC3-EIRENE [73] was used. EMC3-EIRENE is an indispensable tool to model 3D effects in the SOL transport. However, volumetric recombination and drifts were not implemented in the code when the divertor modification was planned (Volumetric recombination was added in the EIRENE part of the code very recently). Volumetric recombination and drifts were required to reproduce important features of the experimentally diagnosed SOL plasma in single null configuration, e.g. divertor detachment [20, 61]. The access to detachment will be an important criterion to evaluate the suitability of the different configurations for a reactor that will need to operate at least partially in that regime. Therefore, simulations with a code including volumetric recombination and drifts, like SOLPS, are strongly required [74].

Chapter 4

The SOLPS code package

The SOLPS (Scrape-Off Layer Plasma Simulation) code package [27, 28] is a combination of the two-dimensional multi-fluid plasma transport code, B2.5, and the three-dimensional kinetic Monte Carlo neutral particle transport code EIRENE [75].

In the last two decades, the code B2.5 was developed by the fusion community (notably research groups at IPP Garching and St. Petersburg State Polytechnical University) based on B2 [76]. The SOLPS versions using B2.5 are marked as SOLPS5.x. In order to unite the most recent advances in both the fluid and neutral codes, the ITER Organization has sponsored the development of a new package, named SOLPS-ITER [28], which couples the parallelized version of the EIRENE code with the B2.5 fluid plasma solver from the SOLPS5.2 package [77]. The code package also includes tools for grid generation ('DG' and 'Carre'), and various scripts for running, maintaining and post-processing the simulations. In the SOLPS-ITER package, the numerical algorithms and implementation of drifts were improved. In addition to this, the stronger pre-processing and post-processing tools make it more convenient to set and analyze a simulation. The SOLPS-ITER code is the principal plasma boundary simulation tool for ITER [28, 78].

Since the master version of SOLPS-ITER was released one year after the beginning of this thesis, SOLPS5.0 was applied in simulations without drifts in chapters 5 and 6, while SOLPS-ITER was used for comparison with experimental data in chapter 7 and simulations with drifts in chapter 8.

4.1 Model equations

The basic aspects of the edge plasma model are obtained by considering the fluid equations of particle, momentum, and energy conservation for both the electron and ion fluids as given by the Braginskii equations [76, 79]. For the

sake of brevity, a simplified set of equations for a purely hydrogenic plasma are given in the following while the more detailed multi-fluid equations can be found in the SOLPS manual [80].

The continuity equations have the form

$$\frac{\partial n_{i,e}}{\partial t} + \nabla \cdot (n_{i,e}\vec{v}_{i,e}) = S^p_{i,e}, \tag{4.1}$$

where $n_{i,e}$ and $\vec{v}_{i,e}$ are the ion and electron densities and fluid velocities, respectively. The particle source terms $S^p_{i,e}$ include ionization, charge exchange and recombination.

The momentum equations are given by

$$\begin{aligned}\frac{\partial(m_{i,e}n_{i,e}\vec{v}_{i,e})}{\partial t} + (\nabla \cdot \vec{v}_{i,e})(m_{i,e}n_{i,e}\vec{v}_{i,e}) = -\nabla p_{i,e} + q_{i,e}n_{i,e}(\vec{E} + \vec{v}_{i,e} \times \vec{B}) \\ -\vec{F}_{i,e} - \vec{R}_{i,e} + \vec{S}^m_{i,e},\end{aligned} \tag{4.2}$$

where $m_{i,e}$ are the ion and electron masses, $p_{i,e} = n_{i,e}T_{i,e}$ the pressures, $T_{i,e}$ the temperatures, $q_{i,e}$ the charges, $\vec{E}$ the electric field, $\vec{B}$ the magnetic field, $\vec{R}_{i,e}$ the friction force with $\vec{R}_e = -\vec{R}_i$ and $\vec{F}_{i,e} = \nabla \cdot \Pi_{i,e}$ the viscous force with the viscous tensor

$$\Pi_{\alpha\beta} = -\eta \left(\frac{\partial v_\alpha}{\partial x_\beta} + \frac{\partial v_\beta}{\partial x_\alpha} - \frac{2}{3}\delta_{\alpha\beta}\nabla \cdot \vec{v} \right), \tag{4.3}$$

where η is the viscosity. The momentum source $\vec{S}^m_{i,e}$ contains effects of external momentum exchange, e.g., with neutrals.

Summing Eqs. 4.2 over all species and neglecting the inertia and viscous terms of electron ($\eta_e/\eta_i \sim \sqrt{m_e/m_i} \ll 1$), one obtains the total momentum equation

$$\frac{\partial m_i n_i \vec{v}_i}{\partial t} + (\nabla \cdot \vec{v}_i)(m_i n_i \vec{v}_i) = -\nabla p + \vec{j} \times \vec{B} - \vec{F}_i + \vec{S}^m_i, \tag{4.4}$$

where $\vec{j}$ is the total current density

$$\vec{j} = q_i n_i \vec{v}_i + q_e n_e \vec{v}_e \tag{4.5}$$

and p is the total static pressure

$$p = p_i + p_e = n_i T_i + n_e T_e. \tag{4.6}$$

The ion and electron internal energy equations can be written in the form

$$\frac{\partial}{\partial t}\left(\frac{3}{2}p_{i,e}\right) + \nabla\cdot\left(\frac{3}{2}p_{i,e}\vec{v}_{i,e} + \vec{q}_{i,e}\right) + (\Pi_{i,e}\cdot\nabla)\cdot\vec{v}_{i,e} + p_{i,e}\nabla\cdot\vec{v}_{i,e} = Q_{i,e} \quad (4.7)$$

where $\vec{q}_{i,e}$ are the ion and electron heat fluxes, and $Q_{i,e}$ the volumetric heating terms.

In order to close the set of equations, transport coefficients are needed for calculating the particle and heat fluxes. However, the perpendicular transport coefficients derived from experimental measurements are orders of magnitude larger than those predicted by the collisional transport theory. The perpendicular transport is found of turbulent nature and labeled anomalous [29, 56]. In SOLPS, anomalous effects are induced by replacing the classical perpendicular particle and heat fluxes with anomalous fluxes [81]. The anomalous ion diffusivity (D^{AN}), ion and electron thermal conductivities ($\chi^{AN}_{i,e}$) and electric conductivities (σ^{AN}) are used to close the fluid equations and create the plasma background. Then drifts (see Eqs. 4.12 and 4.13) are computed based on the local pressure, plasma potential and magnetic field gradients. These drifts in turn change the distribution of plasma parameters and affect anomalous fluxes depending on the gradients of plasma parameters. Thus, a self-consistent treatment of anomalous transport and drifts in the edge plasma is achieved [82].

In the two-dimensional fluid code B2.5, the above mentioned equations are written on a curvilinear orthogonal discrete coordinate system assuming toroidal symmetry [75], i.e. a two-dimensional mesh aligned to the magnetic flux surfaces as shown in Fig. 4.1. The x (poloidal) coordinate varies along flux surfaces and the y (radial) coordinate perpendicular to them. The z coordinate represents the toroidal direction. Quantities in the poloidal direction contain two components which are parallel and perpendicular to the magnetic field line. E.g. the poloidal velocity is given by $v_x = v_\parallel B_x/B + v_\perp B_z/B$.

The discrete equations used in SOLPS are a result of a reasonable trade-off between the physical accuracy and the numerical stability [77]. The ion particle flux in the poloidal (x) and radial (y) directions can be written as

$$\Gamma_{i,x,y} = n_i v_{i,x,y} = \Gamma^{(diff)}_{i,x,y} + \Gamma^{(conv0)}_{i,x,y} + \Gamma^{(drift)}_{i,x,y} + \Gamma^{(current)}_{i,x,y}. \quad (4.8)$$

The first terms on the rhs are the diffusive fluxes

$$\Gamma^{(diff)}_{i,x,y} = -D^{AN}\frac{1}{h_{x,y}}\frac{\partial n_i}{\partial x, y}, \quad (4.9)$$

where D^{AN} is the anomalous diffusivity, and h_x, h_y the cell lengths in poloidal and radial directions, respectively.

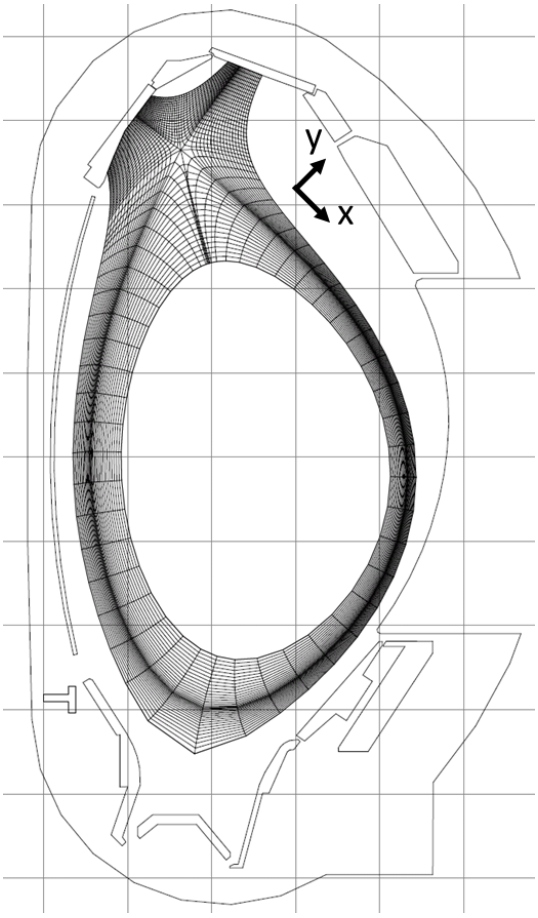

FIGURE 4.1: The two-dimensional mesh of B2.5.

The second terms are the convective fluxes independent of drifts and currents. The poloidal flux relates to the poloidal projection of the parallel velocity and the Rhie and Chow upwind correction velocity [83],

$$\Gamma_{i,x}^{(conv0)} = (b_x v_{i,\parallel} + v_i^{(corr)}) n_i \tag{4.10}$$

where $b_x = B_x/B$ is the ratio of the poloidal component to the total magnetic field. Since the radial (y) direction is perpendicular to the magnetic surface, the radial projection of the parallel velocity is zero, i.e. $\Gamma_{i,y}^{(conv0)} = 0$ if there is no radial anomalous velocity assumed.

The third terms are the convective fluxes driven by the E×B and diamagnetic drifts

$$\Gamma_{i,x,y}^{(drift)} = \Gamma_{i,x,y}^{(E\times B)} + \Gamma_{i,x,y}^{(dia)} \tag{4.11}$$

where

$$\Gamma_{i,x}^{(E\times B)} = -\frac{B_z n_i}{B^2 h_y}\frac{\partial \phi}{\partial y};\ \Gamma_{i,y}^{(E\times B)} = \frac{B_z n_i}{B^2 h_x}\frac{\partial \phi}{\partial x} \tag{4.12}$$

with ϕ the electrostatic plasma potential and

$$\Gamma_{i,x}^{(dia)} = -\frac{B_z}{eB^2 h_y}\frac{\partial\left(n_i T_i\right)}{\partial y};\ \Gamma_{i,y}^{(dia)} = \frac{B_z}{eB^2 h_x}\frac{\partial\left(n_i T_i\right)}{\partial x}. \tag{4.13}$$

Since the continuity equation only depends on the divergence of the particle flux and not on the actual value itself, in the numerical procedure the diamagnetic drift fluxes are replaced by effective fluxes [77] which have approximately the same divergence. This is done in order to improve the numerical stability, while it preserves the result. When we discuss the role of the diamagnetic drift later on in chapter 8, however, we compute the fluxes according to Eq. 4.13 by post-processing the converged solution.

The last terms on the rhs of Eq. 4.8 are the convective fluxes related to currents caused by anomalous transport (j^{AN}), inertia (j^{in}) and viscosity (j^{vis})

$$\Gamma_{i,x,y}^{(current)} = \frac{1}{e}\left(j_{x,y}^{AN} + j_{x,y}^{in} + j_{x,y}^{vis}\right). \tag{4.14}$$

By solving the reduced equations of density, momentum, internal energy and current, we can obtain five main plasma parameters (n_i, $v_{\parallel,i}$, T_i, T_e, ϕ) and derive various variables based on them to describe the SOL plasma under consideration.

4.2 Boundary conditions

In B2.5, the boundary conditions are implemented as boundary sources defined only in the boundary cells of the computational grids [75].

At the innermost radial simulation boundary (the core boundary), the boundary conditions are usually given by prescribing values or gradients of density, parallel velocity, temperature and potential, or alternatively fluxes of particles, momentum, energy and current. At the outermost radial simulation boundary, i.e. the outer boundary of the SOL and private flux region, the conditions are usually given by parameter decay lengths or leakage fluxes. In most cases, the boundary conditions at the core and outer boundaries are set according to experimental measurements.

At the material surface boundary (divertor targets), the situation becomes more complicated. Since the electrostatic sheath and the magnetic presheath are both collisionless and contain complicated kinetic effects, the B2.5 fluid equations for the bulk plasma are no longer valid in these regions. At present, the code assumes that the parallel ion velocity is at least the local sound speed

at the entrance of the magnetic presheath,

$$c_s = \sqrt{\frac{T_e + \gamma_i T_i}{m_i}}, \tag{4.15}$$

where γ_i is the ratio of the specific heats ($\gamma_i = 5/3$ for adiabatic flow).

4.3 Physics of neutral particles

In B2.5-EIRENE coupled simulations, the neutral particle transport, the interaction between plasma, neutrals and material surfaces (reflection, re-emission, pumping) and the atomic and molecular volumetric processes (e.g. ionization, charge-exchange, dissociation and the volumetric recombination of single charged ions to neutrals) are modelled by the 3D kinetic Monte Carlo neutral transport code EIRENE [84]. The coupling procedure between the plasma fluid and Monte Carlo neutrals is implemented by passing data arrays in both directions. The fluid code B2.5 delivers a plasma background to EIRENE, on which the neutral trajectories are computed. The associated particle, momentum and energy sources are deduced by EIRENE and inserted into the source terms in the fluid equations in B2.5 [75].

The EIRENE code solves a multi-species set of coupled Boltzmann-type equations in arbitrary 3D geometries. The Boltzmann-type equation is generalized from its original single species form with a bi-linear collision kernel for elastic collisions, to one with a more complicated collision integral which also represents atomic and molecular reactions by inducing an identifier defining the ionization or excitation stage of a particle [75, 84].

The interaction between neutrals and the material surface is implemented by adding a reflection kernel

$$C_w = p_{wf} C_{wf} + p_{wt} C_{wt} + p_{wa} C_{wa}. \tag{4.16}$$

The reflection kernel C_w is decomposed into kernels related to fast particle reflection C_{wf}, thermal particle re-emission C_{wt} and particle absorption C_{wa} with respective probabilities $p_{wf} + p_{wt} + p_{wa} = 1$ [84]. The fast particle reflection probability p_{wf} is calculated by the reflection databases produced with the TRIM code and its extensions [85]. The thermal particle re-emission is typically treated as a Maxwellian flux distribution at the surface temperature. The particle absorption probability p_{wa} can be used to define pumping surfaces with a pumping speed

$$S = p_{wa} A \sqrt{\frac{T}{2\pi m}} \tag{4.17}$$

where A is the area of the pumping surface.

Besides the complete kinetic Monte Carlo description offered by EIRENE, a simpler and faster neutral fluid model is also available as a standalone version within B2.5 [75]. The neutral species is then treated just like the other plasma species. Since all simulations in this thesis applied the EIRENE code, i.e. the complete kinetic Monte Carlo description for neutrals, we do not discuss such a fluid neutral approach in detail here.

4.4 Setup for a snowflake configuration

In B2.5, the storage and delivery of data are based on 2D arrays. This requires a block-shaped computational grid as shown in Fig. 4.2. For a single null configuration, the physical grids are mapped to this computational grid by cutting the the 'CORE' and 'PFR' regions at the X-point and setting the same radial resolution for them.

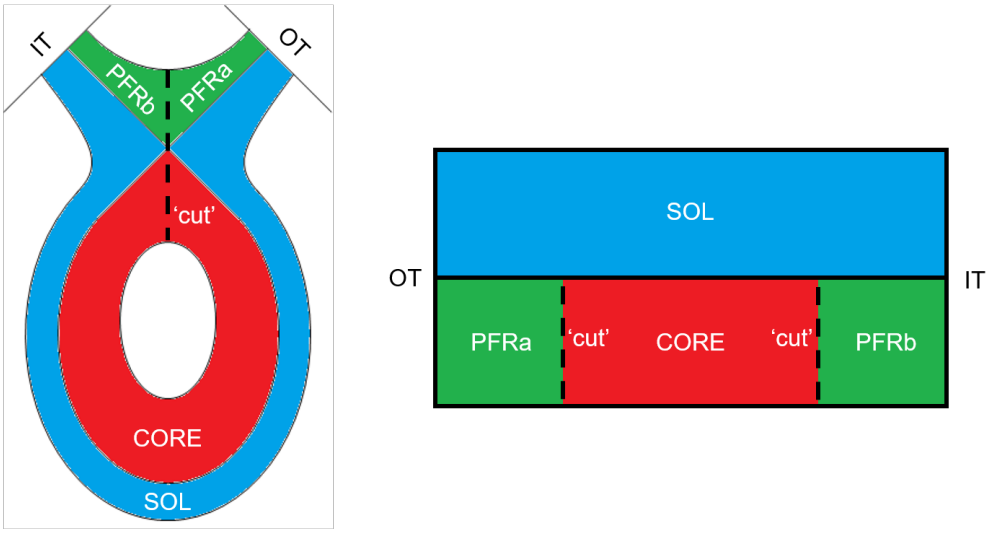

FIGURE 4.2: The block-shaped computational map of B2.5 for a single null divertor configuration.

In a snowflake configuration, due to the existence of the secondary X-point, the topology and therefore the mapping to a block-shaped computational grid is much more difficult. Because the standard grid generator tool of the SOLPS package, 'carre', is not able to generate grids for snowflake topology, such a configuration was never simulated by SOLPS before this thesis.

In this thesis, this technical requirement was met by fulfilling different constraints on the grid resolution and mapping the spatial snowflake grid to the computational map in an appropriate way [74]. The grids for snowflake configurations were not produced using the grid generator tool 'carre', but with the

one developed for EMC3-EIRENE [73] after adapting it to the requirements of SOLPS. A grid for a low-field side snowflake minus (LFS SF$^-$) configuration is shown in Fig. 4.3. It consists of six regions to which we refer as 'confinement region' (CORE, red), 'near-SOL' (NEARSOL, blue), 'far-SOL' (FARSOL, brown), 'private flux region' (PFR, green), and 'remote areas' one (R1, magenta) and two (R2, black). In order to map the physical grids to a block-shaped computational grid, the PFR, FARSOL, and R1 regions are divided into two sub-regions each. The radial resolution of the R2 region is as large as that of the CORE and NEARSOL together, and the poloidal resolution of the R2 region is as large as that of the FARSOLb and R1b together (cf. Fig. 4.4). The radial resolution of the R1 regions is equal to that of the FARSOL regions. The inner target (IT), as well as the primary (OT_1) and secondary (OT_2, OT_3) outer ones, are shown in Fig. 4.4 as vertical lines.

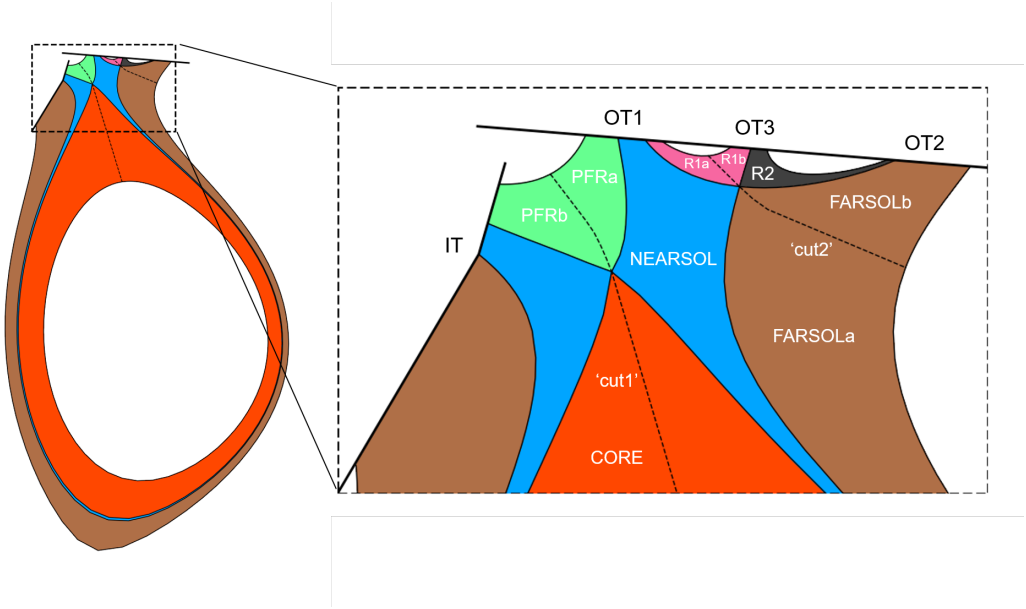

FIGURE 4.3: Physical simulation grids for a low-field side snowflake minus (LFS SF$^-$) configuration.

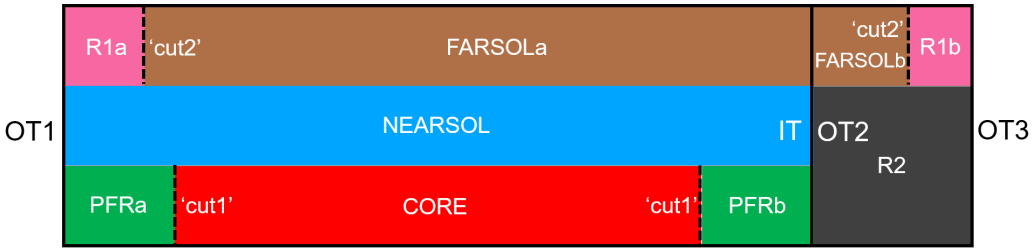

FIGURE 4.4: Block-shaped computational grid for the snowflake configuration in Fig. 4.3.

With such a new type of grids for B2.5 and the corresponding triangle grids for EIRENE (see Fig. 4.5), as well as modified pre-processing and post-processing tools in the code, SOLPS simulations for the snowflake configurations became feasible for the first time.

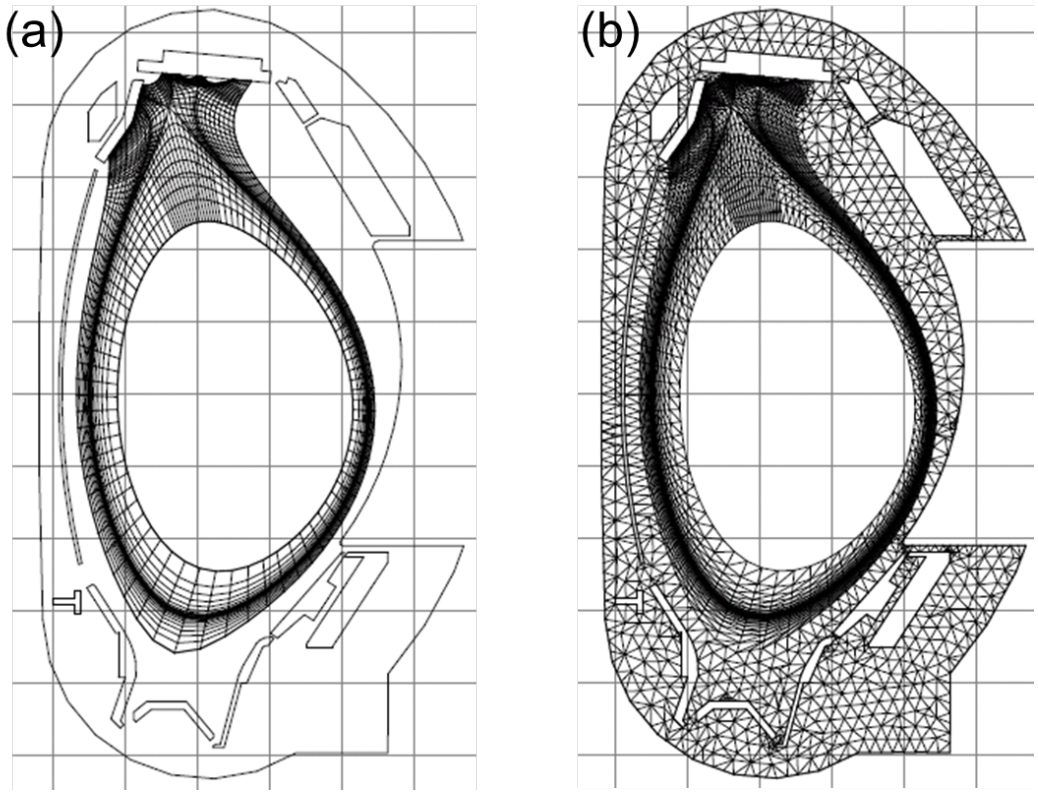

FIGURE 4.5: The two-dimensional meshes of (a) B2.5 and (b) EIRENE for a LFS SF^- configuration.

Chapter 5

SOLPS simulations comparing the single null and alternative divertor configurations

Starting with this chapter, the results of this thesis are presented. As introduced in Chapter 3, alternative divertor configurations (ADCs) have potential advantages for the power exhaust problem. Numerical modeling is an important method for studying the SOL and divertor physics, especially the interaction with divertor detachment. With the modifications discussed in Chapter 4, the SOLPS code has been successfully applied for simulating a low-field side snowflake minus (LFS SF^-) configuration for the first time. This made it possible to study such a configuration in detail. In this chapter, we compare the simulations for the single null (SN), the X-divertor (XD) and the LFS SF^- configurations with the same external input parameters. Part of this chapter's content has been published in [74, 86]. In chapter 6, the evolution of divertor detachment in the snowflake configuration is studied by scanning impurity seeding rates in the simulation. In chapter 7, the SOLPS code is applied to predict the performance of the future alternative divertor configurations based on the experimental measurements in the present upper single null divertor in AUG. In chapter 8, the effect of drifts in the snowflake divertor is presented.

5.1 Simulation setup

The changes in the magnetic configuration can impact the power and particle transport in the divertor. This can result in a different divertor power and particle distribution and divertor detachment compared to that in the standard single null configuration. The physical mechanisms for such differences are complicated, and it is important to choose proper variants and invariants

when comparing different divertor configurations. As a start, we focus on the geometry effects and keep other inputs of the simulations the same for all configurations. For this purpose, the computational grids in Fig. 5.1 were constructed. They are all based on the planned upper divertor (design stage 2018) in AUG but with different currents in the in-vessel coils to achieve the different configurations. In the grids for the X-divertor, an extra X-point is located near the outer target resulting a large poloidal flux expansion there. In the snowflake grids, a secondary X-point is located in the low-field side SOL dividing it into near and far-SOL regions connected to the areas around outer target 1 and 2 (OT1 and OT2), respectively. In addition to that the two remote regions R1 and R2 are connected to a third strike point at the outer target 3 (OT3).

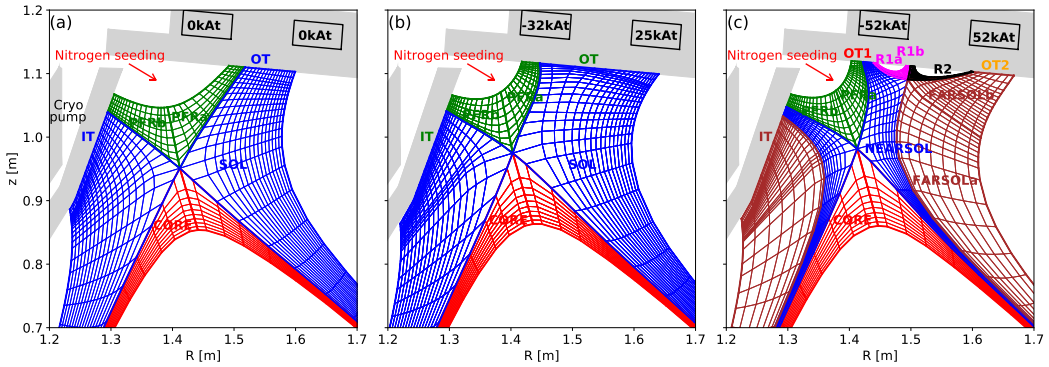

FIGURE 5.1: Physical simulation grids of the (a) single null (SN), (b) X-divertor (XD) and (c) low-field side snowflake minus (LFS SF^-) geometries. Currents in the additional poloidal field coils are indicated.

In the simulations for the three configurations, the heating power at the innermost radial boundary is set to $P_{core} = 5$ MW. The deuterium ion (D^+) density at the innermost radial boundary is adjusted to achieve a density of 3×10^{19} m^{-3} at the separatrix at the outer mid-plane. Spatially and temporally constant transport coefficients are chosen as $D^{AN} = 0.2$ m^2/s and $\chi_e^{AN} = \chi_i^{AN} = 0.6$ m^2/s. The transport coefficients are similar to those in SOLPS simulations for ITER ($D^{AN} = 0.3$ m^2/s and $\chi_e^{AN} = \chi_i^{AN} = 1.0$ m^2/s) [87]. Nitrogen gas (N_2) is puffed as impurity into the private flux region (red arrow in Fig. 5.1) at a rate of $\Phi_{N_2,PFR} = 5.0 \times 10^{20}$ s^{-1}, corresponding to 7.0×10^{21} electrons per second. This magnitude is comparable with typical experimental values for detached AUG lower single null discharges [58, 61].

The atomic and molecular reactions activated in this simulation include ionization, charge exchange and recombination of deuterium atoms, ionization and recombination of nitrogen atoms, as well as dissociation of deuterium and nitrogen molecules (see Tab. 5.1). The nitrogen-deuterium charge exchange re-

action is assumed to be negligible here because of its non-resonant character, while nitrogen-nitrogen charge exchange is neglected due to the small concentration $n_{N^{1+}}/n_{D^+}$ in the confinement region and SOL. Ions that leave the grid across the outermost radial grid boundary or hit the target as well as neutrals hitting the main chamber wall are fully recycled into the simulation domain as neutrals at all surfaces, except for the cold ones of the cryo pump (see Fig. 5.1) where a total recycling coefficient of 90 % was assumed. The remaining 10 % are absorbed by the pump. This value corresponds to a pumping speed of about 50 m^3/s, for which the pump is designed. The fraction of fast and thermal particle reflection as well as the energy reflection coefficient are calculated by the TRIM and SDtrimSP database reflection models and included in EIRENE [85].

Reaction	Type
$D + e^- \longrightarrow D^+ + 2e^-$	Ionization
$D + D^+ \longrightarrow D^+ + D$	Charge exchange
$D + D^+ \longrightarrow D + D^+$	Elastic collision
$D^+ + e^- \longrightarrow D + \gamma$	Recombination
$D_2 + e^- \longrightarrow D_2^+ + 2e^-$	Ionization
$D_2 + D^+ \longrightarrow D_2^+ + D$	Charge exchange
$D_2 + D^+ \longrightarrow D_2 + D^+$	Elastic collision
$D_2 + e^- \longrightarrow 2D + e^-$	Dissociation
$D_2 + e^- \longrightarrow D^+ + D + 2e^-$	Ionizing dissociation
$D_2^+ + e^- \longrightarrow D + D^+ + e^-$	Dissociation
$D_2^+ + e^- \longrightarrow 2D^+ + 2e^-$	Ionizing dissociation
$D_2^+ + e^- \longrightarrow 2D + \gamma$	Recombining dissociation
$N + e^- \longrightarrow N^+ + 2e^-$	Ionization
$N^+ + e^- \longrightarrow N + \gamma$	Recombination
$N_2 + e^- \longrightarrow 2N + e^-$	Dissociation

TABLE 5.1: The atomic and molecular reactions activated in the simulations.

5.2 Divertor behaviour

The same input parameters and transport coefficients result in similar density, temperature and total pressure profiles at the outer mid-plane in all configurations (see Fig. 5.2). The power fall-off length λ_q at the outer mid-plane is about 3 mm, which is a typical value in AUG experiments [5].

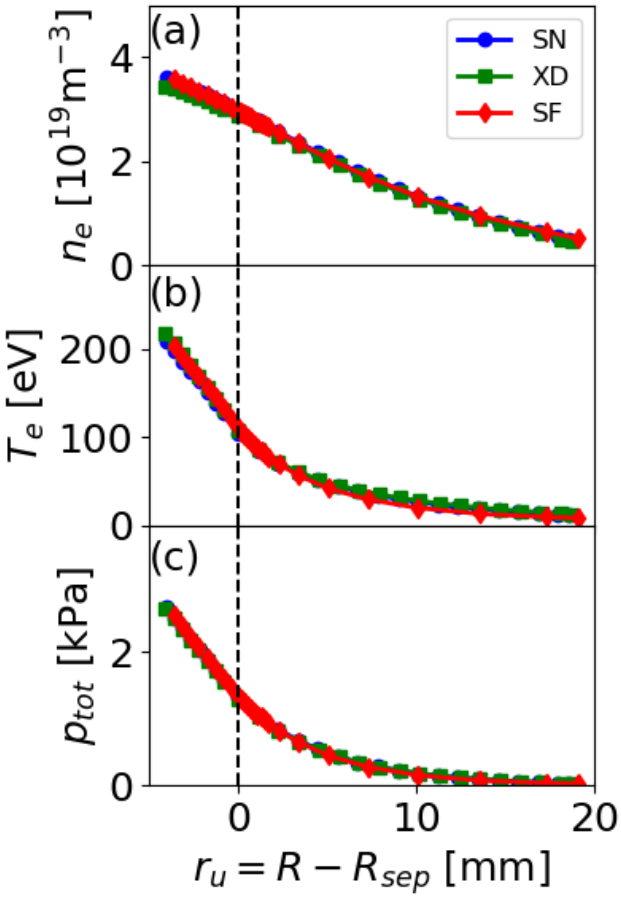

FIGURE 5.2: (a) Electron density, (b) electron temperature and (c) total pressure profiles at the outer mid-plane as a function of the distance to the (primary) separatrix.

The plasma parameters in the divertor are closely related to the upstream ones. The similar upstream (OMP) profiles in Fig. 5.2 facilitate the identification of the effects of the divertor geometry. Since the main difference in these three configurations is in the outer divertor, here we concentrate on the comparison in this region. The outer target profiles of parallel power flux density, electron density, temperature and total pressure in these three configurations are compared in Fig. 5.3. For convenience, the radial coordinates at the target were mapped to the outer mid-plane. Note that the poloidal magnetic flux expansion between upstream and target $f_x = \delta r_t / \delta r_u$ is a strong function of the target coordinate, such that the same upstream interval δr_u can correspond to a very different δr_t at the target. In the single null case, the temperature is above 1 eV along the whole outer target and the maximum value is about 16 eV located at $r_u \approx 3.5$ mm. Except for the small region around the strike point ($0 < r_u < 1$ mm), no pressure loss is found between the outer mid-plane

and the target. This indicates that nearly the whole outer target is attached in the single null configuration.

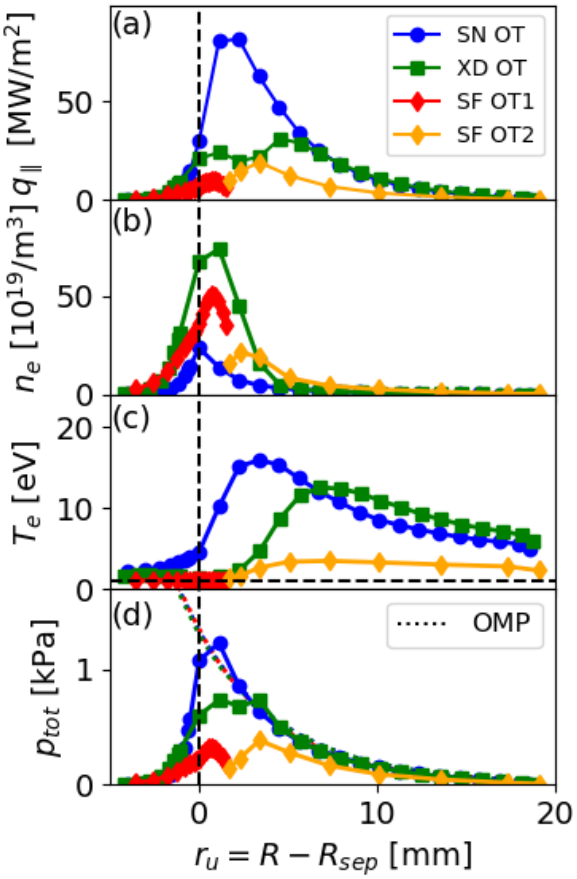

FIGURE 5.3: (a) Parallel power flux density, (b) electron density, (c) electron temperature and (d) total pressure profiles at the outer divertor targets. The target coordinate was mapped to the radial coordinate r_u at the outer mid-plane shown on the horizontal axis. Plot (d) also shows the upstream total pressure (dotted lines) compared to that at the target (solid lines).

As introduced in section 3.5, the large poloidal flux expansion near the secondary X-point in the X-divertor configuration and the SOL splitting effect of the secondary X-point in the snowflake divertor configuration can reduce the maximum power flux at the outer target. In addition to this, the connection length from the outer mid-plane to the outer target is larger in the alternative divertor configurations than that in the single null configuration, especially near the secondary X-point in the snowflake one (see Fig. 5.4 at $r_u \approx$1.7 mm). The larger connection length leads to a lower temperature and higher density in the divertor as visible in Fig. 5.3. In the X-divertor, the maximum parallel power flux density is reduced by 63 % compared to that in the single null case.

In the region $0 < r_u < 2$ mm, the density is high, and the temperature is low (about 1.5 eV). A pressure loss can be seen in this region, indicating that this part of the target is detached. However, in the outer part of the target ($r_u > 6$ mm), the temperature is similar to that in single null, and the target pressure is similar to that at the outer mid-plane. This means that the outer target is partially detached in the X-divertor. In the snowflake divertor, the maximum parallel power flux density is 78 % lower than that in the single null case. This value is also 68 % lower than that predicted by the SOL splitting model [19] introduced in chapter 3. Such a further reduction of power fluxes is caused by the enhanced radiation as it will be discussed in the next section. The temperature is below 1 eV at OT1 and about 3 eV at OT2. Meanwhile, significant pressure losses were found at nearly the entire surface of both outer targets. This indicates that OT1 and OT2 are both completely detached in the snowflake configuration.

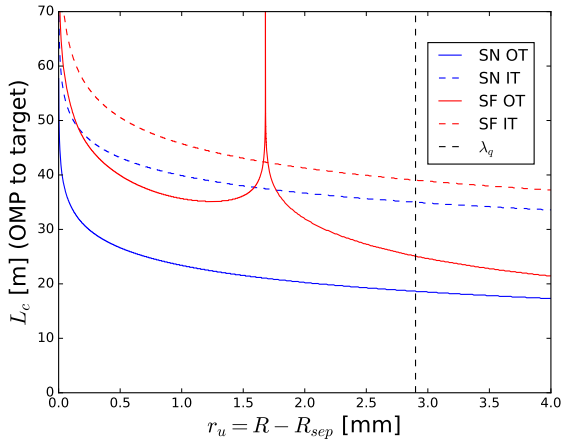

FIGURE 5.4: Connection length L_c of field lines at different radii from the outer mid-plane to the inner (dashed line) and outer (solid line) targets in the LFS SF^- (red) and SN (blue) configurations. The vertical dashed line indicates the power fall-off length λ_q. Taken from [74].

5.3 Radiation and volumetric recombination

In order to study the physical reason for the stronger detachment in the alternative divertor configurations, poloidal cross-sections of electron density, electron temperature and radiation power density in the different divertors are plotted in Fig. 5.5. Compared to the single null case, regions with higher densities and lower temperatures were found around the primary outer strike point in the alternative divertor configurations. In the X-divertor, this region

is located between the strike point and the secondary X-point just in front of the outer target. In the snowflake divertor, the region is larger and expanding from OT1 to the zone between the primary and secondary X-points where high radiation power densities were found (see Fig. 5.5 (i)).

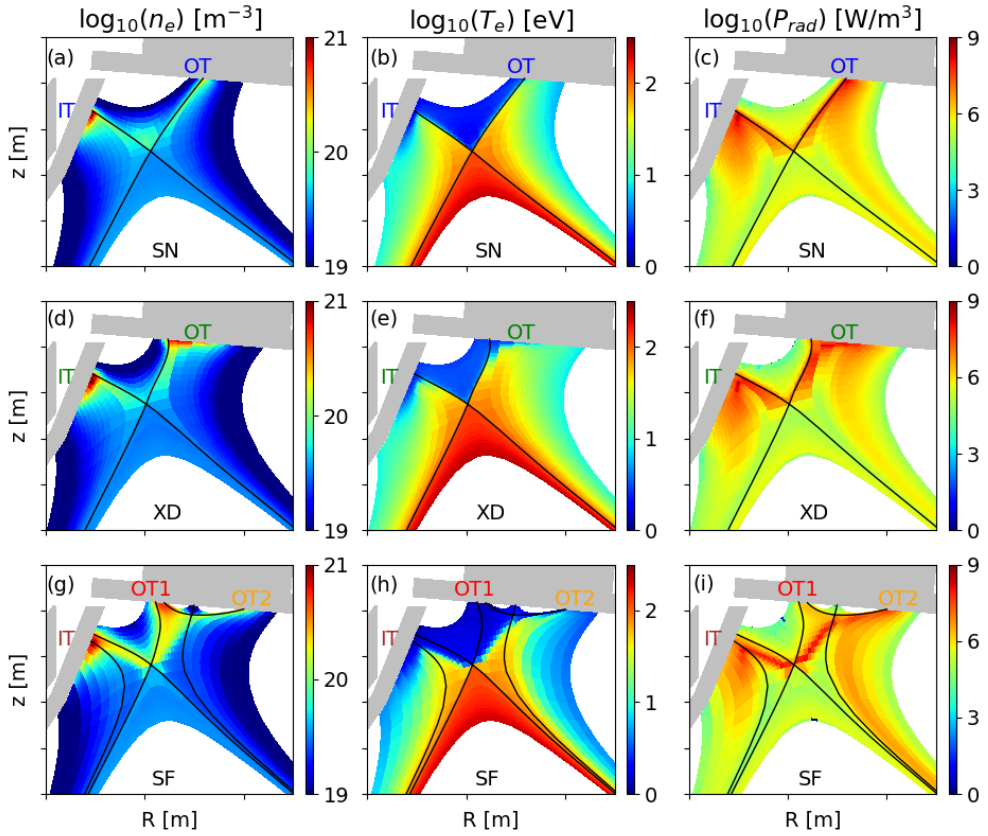

FIGURE 5.5: Simulation results of (a,d,g) electron density, (b,e,h) electron temperature and (c,f,i) radiation power losses in the divertor region. The top row (a-c) shows the single null divertor, the middle row (d-f) the X-divertor and the lower row (g-i) the snowflake divertor.

Figure 5.6 compares the power balance among these three configurations. Compared to the single null case ($f_{rad,SN} \approx 71$ %), the radiation fractions are larger in the X-divertor ($f_{rad,XD} \approx 79$ %) and the snowflake cases ($f_{rad,SF} \approx 88$ %), contributing to a further power reduction at the targets. In addition to this, the higher radiation fraction in the X-divertor and snowflake divertor configurations was achieved with slightly lower radiation power and impurity concentration in the confinement region.

As introduced in section 3.3, the power loss due to the nitrogen impurity radiation can be expressed by $P_{rad} = n_e^2 c_N L_N$, where $c_N = n_N/n_e$ is the nitrogen concentration and L_N the effective radiative cooling rate of nitrogen

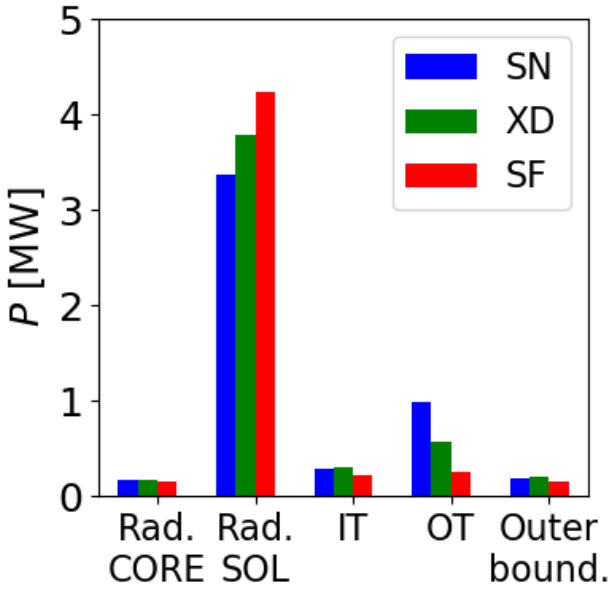

FIGURE 5.6: Integrated power of radiation in the regions of CORE and SOL, at the inner and outer targets and leaving the outermost simulation boundary.

which is strongly depending on electron temperature and maximum around 10 eV (see Fig.3.4). The larger connection length and poloidal flux expansion in the alternative configurations lead to higher densities and lower temperatures in the divertor region and in consequence, enhance the radiation power loss. We here define the radiation volume of nitrogen as the volume where the electron temperature is between 5 and 15 eV. Figure 5.7 (a) and (b) show the radiation volume in the single null and snowflake configurations, respectively. In the snowflake divertor, an additional radiation volume is found in the high-density region between the primary and the secondary X-points. This results in the additional high-radiative region in Fig. 5.5 (i) and higher total radiation power in the snowflake case.

Besides the radiation, the volumetric recombination is expected to further reduce the power to the target by reducing the flux of charged particles. However, the volumetric recombination is only significant in regions with a high density and a temperature lower than about 1 eV. The higher density and lower temperature at the targets in alternative divertor configurations make it easier to reach this condition. As a result, the total volumetric recombination rates in the single null, X-divertor and snowflake cases are 5.0×10^{20} s^{-1} (1 % of the ion flux to the OT), 3.5×10^{21} s^{-1} (7 % of the ion flux to the OT) and 5.7×10^{21} s^{-1} (24 % of the total ion flux to OT1 and OT2), respectively. The enhanced volumetric recombination in the alternative divertor configurations can contribute to the momentum removal in the SOL and the achievement of

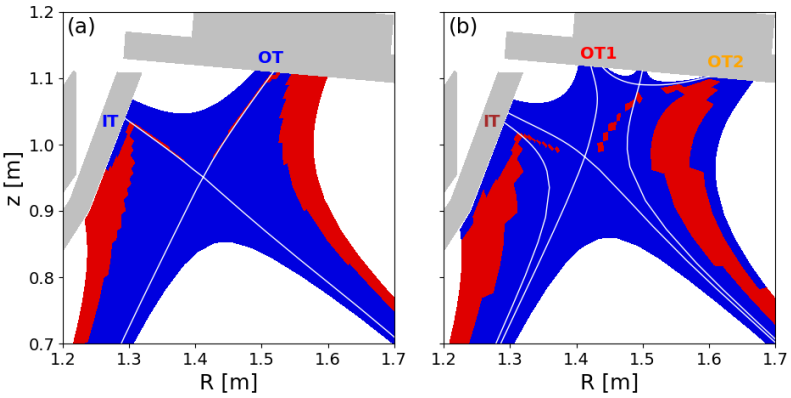

FIGURE 5.7: The radiation volume (red) with a electron temperature between 5 to 15 eV in the (a) single null and (b) snowflake configurations.

the divertor detachment.

5.4 Summary

In this chapter, we compared the SOLPS simulation results between the single null (SN) and alternative divertor configurations (ADCs). It is found that the alternative divertor configurations, especially the low-field side snowflake minus (LFS SF^-) configuration, show advantages in reducing target power loads and achieving divertor detachment. Since other input parameters were the same in the simulations, it is concluded that the changes in the magnetic configuration are the main reason for the different divertor performances. Apart from the effects predicted by a simple analytical SOL-splitting model, the enhanced radiation and volumetric recombination are considered to play important roles in the reduction of the power and particle fluxes to the target and the achievement of divertor detachment in the snowflake configuration.

The fact that the radiation contributes substantially to the power dissipation in the snowflake divertor motivates the study of the effect of radiation on power exhaust and divertor detachment more in detail. For this reason, we compare the evolution of divertor detachment in the single null and snowflake configurations with an impurity seeding scan in the next chapter.

Chapter 6

Impurity seeding scan

The simulation results in chapter 5 showed that, with the same nitrogen seeding rate, the target loads are lower in the snowflake (LFS SF^-) than in the single null (SN) configuration. Substantial differences in the power and particle dissipation, via radiation and volumetric recombination were found between these two configurations. Based on this result, some additional questions are investigated in this chapter. The questions of the snowflake configuration include (1) whether the effects described in chapter 5 rely on a specific range of nitrogen seeding rate; (2) whether the evolution of the divertor detachment, e.g. asymmetries between the inner and outer targets, is different; (3) whether divertor detachment without confinement degradation is achievable. In order to study these questions, we analyzed the evolution of divertor conditions in the snowflake configuration with a variation of the nitrogen seeding rate and compared it to the single null reference.

This chapter is divided into 2 parts: Section 6.1 compares the evolution of divertor detachment in the single null and snowflake configurations. A detailed analysis of power and particle balances in the SOL is shown in section 6.2.

6.1 Evolution of divertor detachment

The simulation grids used here are the same as in Figs. 5.1 (a) and (c). The spatially constant transport coefficients, input power and the database for the atomic and molecular reactions are also the same as those used in chapter 5. Nitrogen gas is puffed into the private flux region at a puffing rate scanned from 1.4×10^{21} to 1.4×10^{22} e^-/s. Since the divertor conditions are sensitive to the upstream density, variation in the upstream density with nitrogen seeding rates can make the comparison in the divertor difficult. In order to exclude the influence of the upstream density and focus on the effects in the divertor region, the D^+ density is adjusted to achieve a separatrix electron density of

$n_{e,sep} = 3 \times 10^{19}$ m^{-3} with 2 % accuracy at the outer mid-plane (OMP) in all cases within the scan.

As introduced in chapter 3, the divertor detachment features a roll-over of target particle flux, a pressure loss between the upstream position and the target and a sufficiently low target temperature. The detachment process can be understood as follows. With increasing nitrogen seeding, the target temperature decreases due to the power loss via impurity radiation. The collisionality increases near the target. More recycling neutrals are ionized near the target and transported back. The density and particle flux at the target increase until the remaining power is insufficient for maintaining such a large number of ionization processes. When more nitrogen is puffed, the particle flux decreases and shows a roll-over phenomenon. Before the roll-over, the total pressure at the target is similar to that at the upstream position. The target is attached. After the roll-over, the target temperature and density decrease simultaneously, and the momentum of ions is removed via charge exchange collisions, cross-field transport and volumetric recombination. A pressure loss is found between the upstream position and the target, which is a typical feature of divertor detachment.

The detachment process is usually inhomogeneous along the target. For illustrating the power exhaust problem, we here focus on the position where the target parallel power flux density is maximal in the lowest-seeding case ($\Phi_{N_2} = 1.4 \times 10^{21}$ e$^-$/s). In the snowflake case, this position at the outer target is located at OT1 (see Fig. 5.1 (c)). In both configurations, the flux tube connected to maximum power flux is about 1 mm away from the separatrix at the outer mid-plane ($r_u \approx 1$ mm $\approx 1/3\lambda_q$). We analyze the same position in the whole scan.

Figure. 6.1 depicts the evolution of some key parameters due to the variation of nitrogen seeding rate, comparing between the simulations for the two configurations. Plotted are the parallel D^+ particle fluxes, pressure loss ratios $(p_{up}-p_{tar})/p_{up}$ between the total pressure at the upstream position p_{up} and the target p_{tar} and electron temperatures at the inner and outer divertor targets. Each target shows the above-mentioned evolution from the attached to the detached regime. However, there are some remarkable differences between the two configurations. We divide the following analysis into two parts. (1) The low seeding rate cases prior to the particle flux roll-over occurs at outer target in the single null configuration ($\Phi_{N_2} = 1.4$–4.2×10^{21} e$^-$/s). In this part, we focus on whether the snowflake configuration can achieve an earlier divertor detachment compared to the single null configuration. (2) The high seeding rate cases after the particle flux roll-over at the outer target in the single null configuration ($\Phi_{N_2} \geq 4.9 \times 10^{21}$ e$^-$/s). In this part, we focus on the question whether the snowflake configuration still shows advantages when the target in

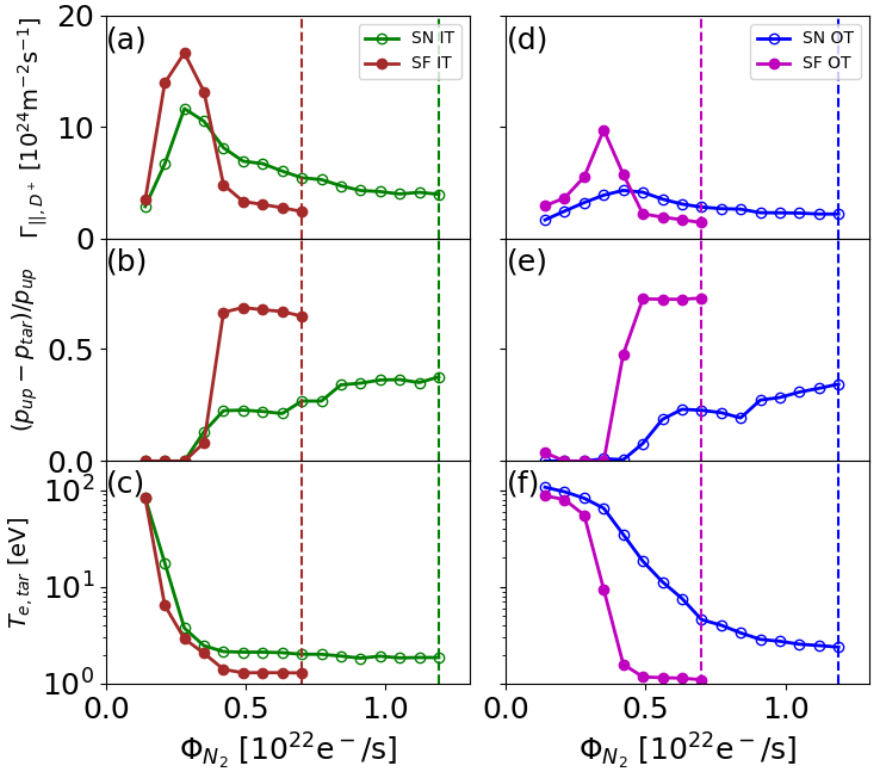

FIGURE 6.1: (a, d) Parallel deuterium ion flux density at the target, (b, e) the pressure loss fraction, (c, f) electron temperature at the targets. The left column shows the inner target and the right one shows the outer target. These quantities are for a flux tube at a fixed $r_u \approx 1$ mm in the whole scan. The impurity seeding rates at which the upstream pressure degradation occurs and the simulation is ended are marked by vertical dashed lines

the single null configuration is also detached. We are particularly interested in the divertor performance just before the upstream pressure degradation which could lead to a confinement degradation.

6.1.1 Low-seeding cases

As shown in Fig. 6.1, the inner targets detach at similar seeding rates (2.8×10^{21} e$^-$/s) in the single null and snowflake configurations. However, the snowflake case shows a higher maximum particle flux density, a larger pressure loss and a lower target temperature. The reason for this will be discussed in section 6.2.

At the outer target, the D^+ particle flux in the single null case increases moderately and shows a roll-over at a seeding rate of about 4.9×10^{20} e$^-$/s. However, the D^+ particle flux in the snowflake case increases faster and shows

an earlier beginning of detachment at a seeding rate of about 3.5×10^{20} e^-/s. After that, a much larger pressure loss and lower target temperature are found in the snowflake configuration.

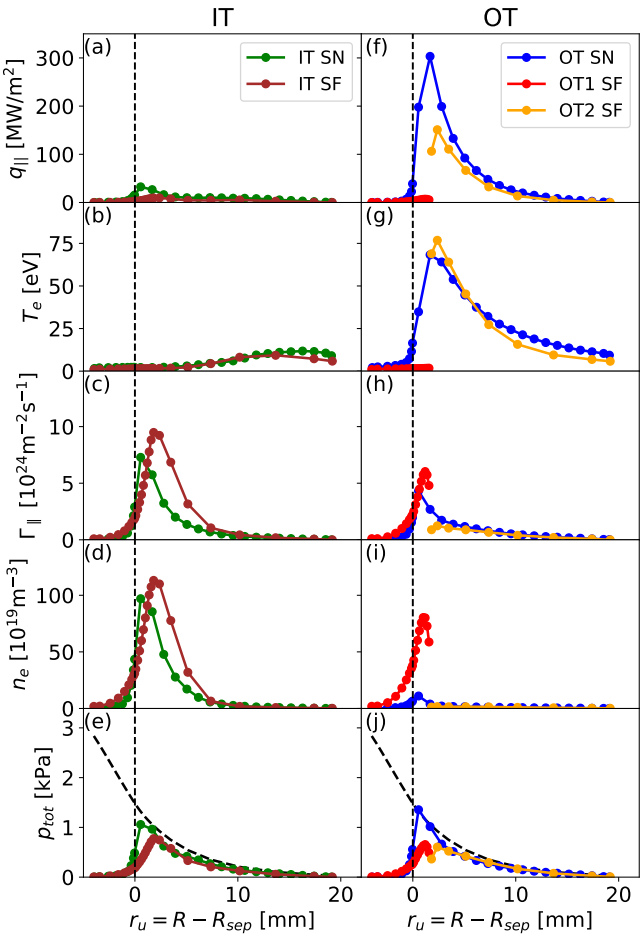

FIGURE 6.2: Inner (left column) and outer (right column) target profiles of (a,f) parallel power fluxes, (b,g) electron temperature, (c,h) parallel ion particle fluxes, (d,i) electron density and (e,j) total pressure in the snowflake and single null divertor configurations at a nitrogen seeding rate of 4.2×10^{21} e^-/s. The total pressure at the outer mid-plane are also shown in (e,j) by the dashed lines.

Figure 6.2 shows the target profiles of parallel power fluxes, electron temperature, parallel ion particle fluxes, electron density and total pressure at a seeding rate of 4.2×10^{21} e^-/s, just before the roll-over at the outer target in the single null configuration.

At the inner target in both configurations, the power fluxes and temperatures are low, and pressure losses can be seen near the strike point. This indicates a partial detachment. However, the position of the peaks in the particle flux and density profiles are further away from the inner strike point

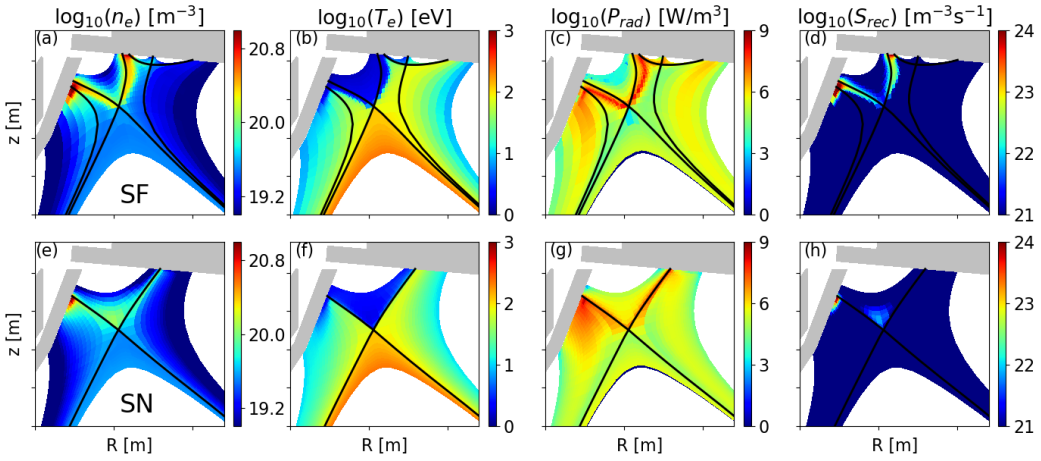

FIGURE 6.3: Two-dimensional distributions of (a) electron density, (b) electron temperature, (c) radiation power density and (d) volumetric recombination rate in the snowflake (upper row) and single null (lower row) divertor configurations at a nitrogen seeding rate of 4.2×10^{21} e^-/s.

in the snowflake configuration compared to that in the single null case. The pressure loss region is also radially wider in the snowflake case. Figure 6.3 compares the poloidal cross-sections of electron density, electron temperature, radiation power and volumetric recombination rate. The high-density and low-temperature region near the inner strike point is larger in the plots for the snowflake divertor. Comparing Fig. 6.3 (d) and (h), one can also find a higher volumetric recombination rate in the inner divertor in the snowflake configuration. These findings imply that the snowflake configuration also shows advantages for the detachment in the inner divertor.

In Fig. 6.2, much lower power fluxes, lower temperatures and higher densities are found at the OT1 in the snowflake configuration compared to the single null case. A substantial pressure loss can be seen there, while the target pressure in the single null case still keeps similar to the one at the outer midplane. This indicates that the OT1 in the snowflake case is already detached while the OT in the single null case is still attached. In Fig. 6.3 (a) and (b), a high-density, low-temperature region forms near OT1 in the snowflake configuration. At the same time, substantially higher radiation and volumetric recombination rates are seen in this region. A quantitative analysis will be given later in section 6.2.

6.1.2 High-seeding cases

In Fig. 6.1, when more nitrogen is seeded, the particle flux and the target temperature at the analyzed position drop quickly in the snowflake configuration. The fraction of the pressure loss increases and reaches more than 70 % (see

Fig. 6.1 (e)). The high radiation region moves to the primary X-point. Finally, when the seeding rate exceeds about 7.0×10^{21} e^-/s, the high radiation region moves into the confinement region near the primary X-point, resulting in a decrease of the upstream pressure which could lead to a confinement degradation [37, 88]. In the single null configuration, the changes of the particle flux, the pressure loss and the target temperature are slower than the ones in the snowflake configuration. Finally, at a seeding rate of about 1.2×10^{22} e^-/s, a sudden drop of the target temperature occurs, accompanied by the occurrence of a high radiation region around the X-point and a upstream pressure degradation. This kind of sudden drop of the target temperature was also found in experiments [89] and previous simulations [37]. The pressure loss ratios are about 40 % in the single null configuration before the upstream pressure degradation.

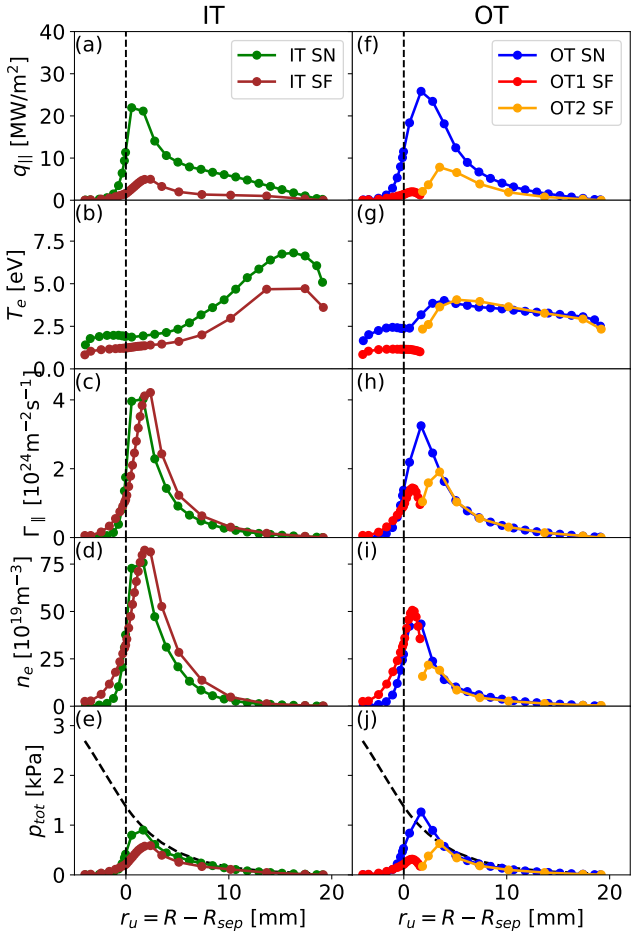

FIGURE 6.4: Same as Fig. 6.2 but at nitrogen seeding rates shortly before the upstream pressure degradation (7.0×10^{21} e^-/s for the snowflake configuration and 1.19×10^{22} e^-/s for the single null configuration).

Due to the upstream pressure degradation, the separatrix density can no longer be fixed, so it does not make sense to continue this scan to higher seeding rates. What we are interested in here is the divertor performance just before the upstream pressure degradation. Similar to Figs. 6.2 and 6.3, Figs. 6.4 and 6.5 show a comparison of the target profiles and two-dimensional distributions between the single null and snowflake configurations. We compare the case with $\Phi_{N_2} = 7.0 \times 10^{21}$ e$^-$/s in the snowflake configuration to the case with $\Phi_{N_2} = 1.19 \times 10^{22}$ e$^-$/s in the single null configuration as indicated by the vertical dashed lines in Fig. 6.1.

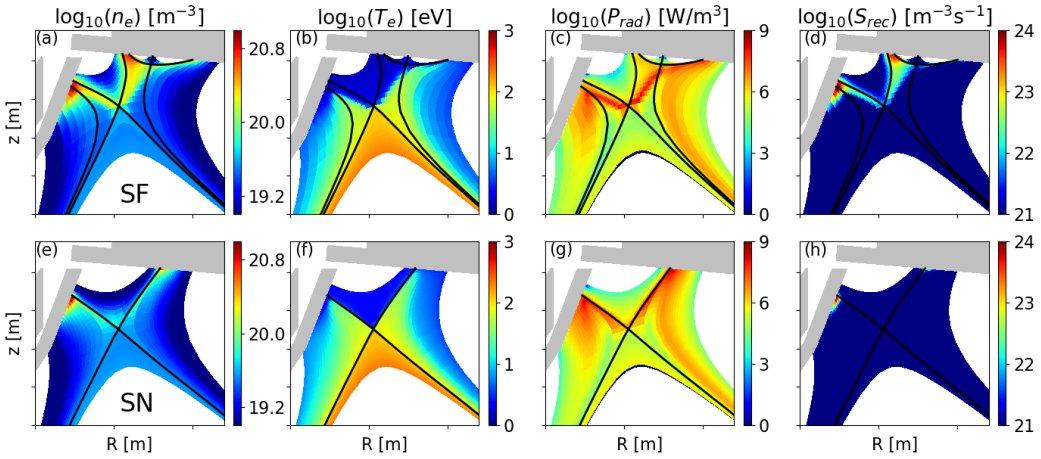

FIGURE 6.5: Same as Fig. 6.3 but at nitrogen seeding rates shortly before the upstream pressure degradation (7.0×10^{21} e$^-$/s for the snowflake configuration and 1.19×10^{22} e$^-$/s for the single null configuration).

At the outer targets, the maximum parallel power flux in the snowflake case is 70 % lower than that in the single null case. One can also see a lower temperature, parallel particle flux and total pressure at OT1 and the inner part of OT2. An additional high radiation region between the primary and the secondary X-points and higher volumetric recombination can be seen in the snowflake case in Fig. 6.5. These indicate that the snowflake configuration can achieve lower target power and particle loads and a higher degree of detachment [10] (DOD$\propto n_u^2/\Gamma_{D^+,tar}$, see section 3.3) before the upstream pressure degradation compared to the single null one. This implies that the snowflake configuration could extend the operational window towards higher fusion performance with acceptable divertor target loads, which is one of the most important motivations for the study of alternative divertor configurations.

6.2 Power and particle balances in the SOL

In order to study the reason for the above-observed differences between the single null and snowflake configurations, the evolution of the power and particle balances during the scan was analyzed. A simple sketch of the simulation grid is shown in Fig. 6.6. For convenience, we mark the SOL region from the outer mid-plane to the inner divertor target as MI and that to the outer target(s) as MO. For each SOL region from the outer mid-plane to divertor targets, the power and particle (here we focus on the main plasma ion species D^+) balances can be written as

$$P_{tar} = P_{up} - P_{out} - P_{rad}, \tag{6.1}$$

$$\Phi_{tar} = \Phi_{up} - \Phi_{out} + S_{ion} - S_{rec}, \tag{6.2}$$

respectively, where P_{tar} and Φ_{tar} are the integrated power and D^+ ion particle fluxes reaching the divertor target in the corresponding interval, $P_{up} = P_{core} + P_{omp}$ and $\Phi_{up} = \Phi_{core} + \Phi_{omp}$ are those into the region of interest radially from the confinement region or poloidally from the outer mid-plane, P_{out} and Φ_{out} are those fluxes across the outer boundary of the simulation grid or across the divertor leg into the private flux region. P_{rad} is the total radiation power, S_{ion} and S_{rec} the total volumetric ionization and recombination rates in this region, respectively.

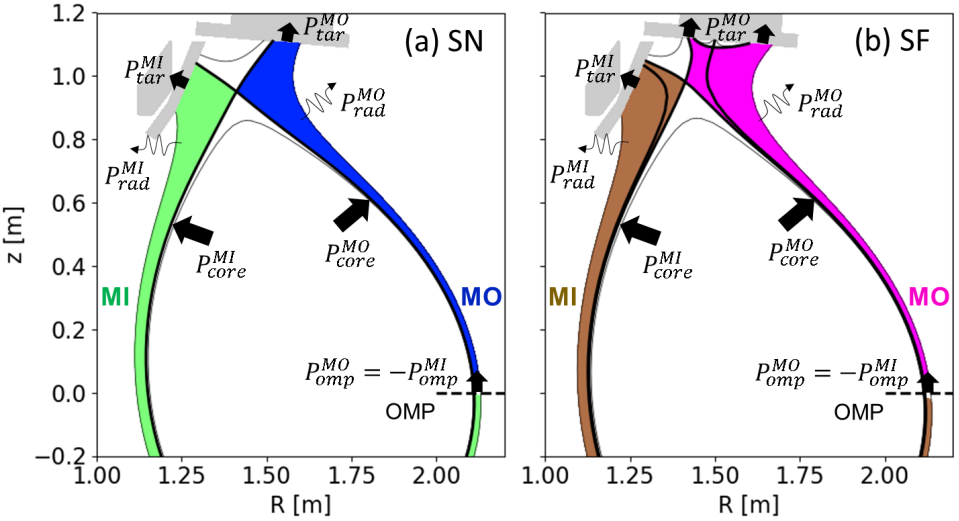

FIGURE 6.6: Power balance in the SOL for (a) single-null (SN) and (b) low-field side snowflake minus (LFS SF^-) geometries.

Figure 6.7 shows the evolution of P_{tar}, P_{up} and P_{rad} with varying nitrogen seeding rates in the regions of MI and MO. P_{out} is not shown here because it is less than 5 % of P_{up}, and there is nearly no difference between the single

null and snowflake configurations. In order to figure out the scrape-off layer splitting effect in MO of the snowflake configuration, the quantities in the near and far-SOL regions MO1 and MO2 are also shown separately (dashed red and orange lines) in addition to the sum of them (solid purple lines).

Figure 6.8 compares Φ_{tar}, S_{ion} and S_{rec} in the regions defined as in Fig. 6.7. In most cases during the scan, the recycling near the targets is quite high, and Φ_{up} and Φ_{out} are negligible compared to S_{ion}. Since the volumetric recombination is a typical feature of divertor detachment, we show it here although its value is small.

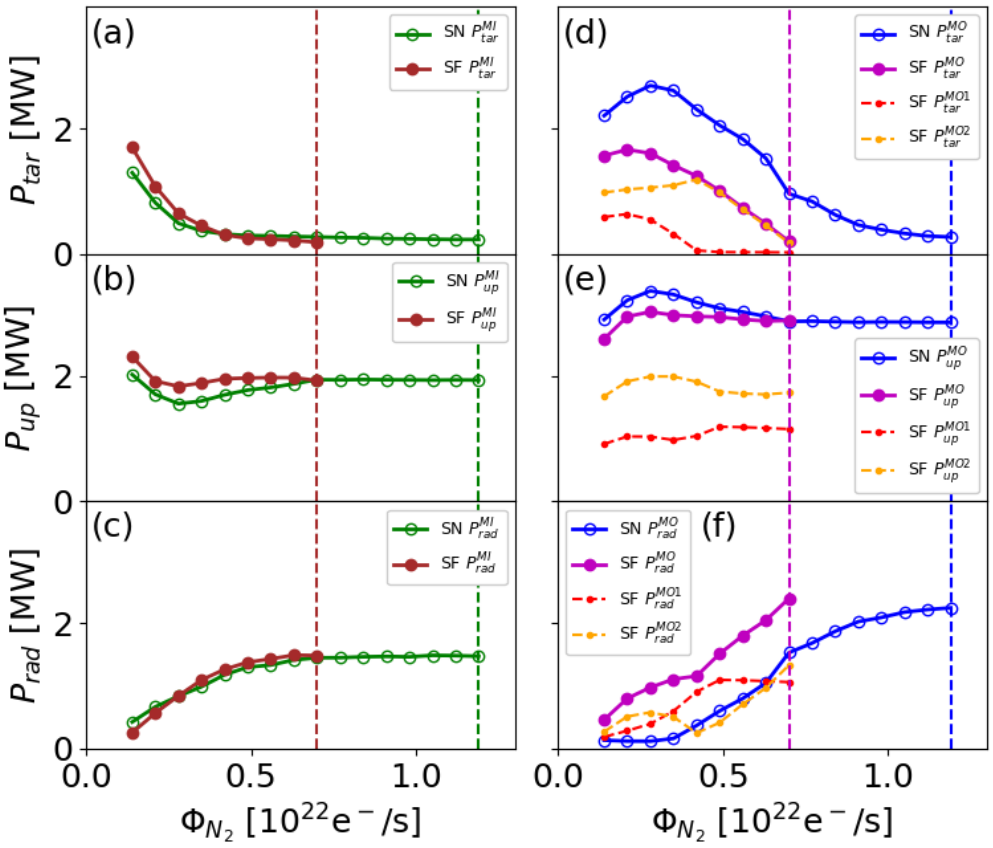

FIGURE 6.7: A comparison of the power balances in the single null and snowflake configurations. (a, d) The power flux reaching the divertor target, P_{tar}; (b, e) the power flux from the confinement region and the outer mid-plane, $P_{up} = P_{core}+P_{omp}$; (c, f) total radiation power, P_{rad} in the regions MI (left column) and MO (right column). The impurity seeding rates at which the upstream pressure degradation occurs are marked by the vertical dashed lines.

In the single null configuration, comparing Fig. 6.7 (b) and (e), one can find that the power from the upstream position into the inner divertor is lower

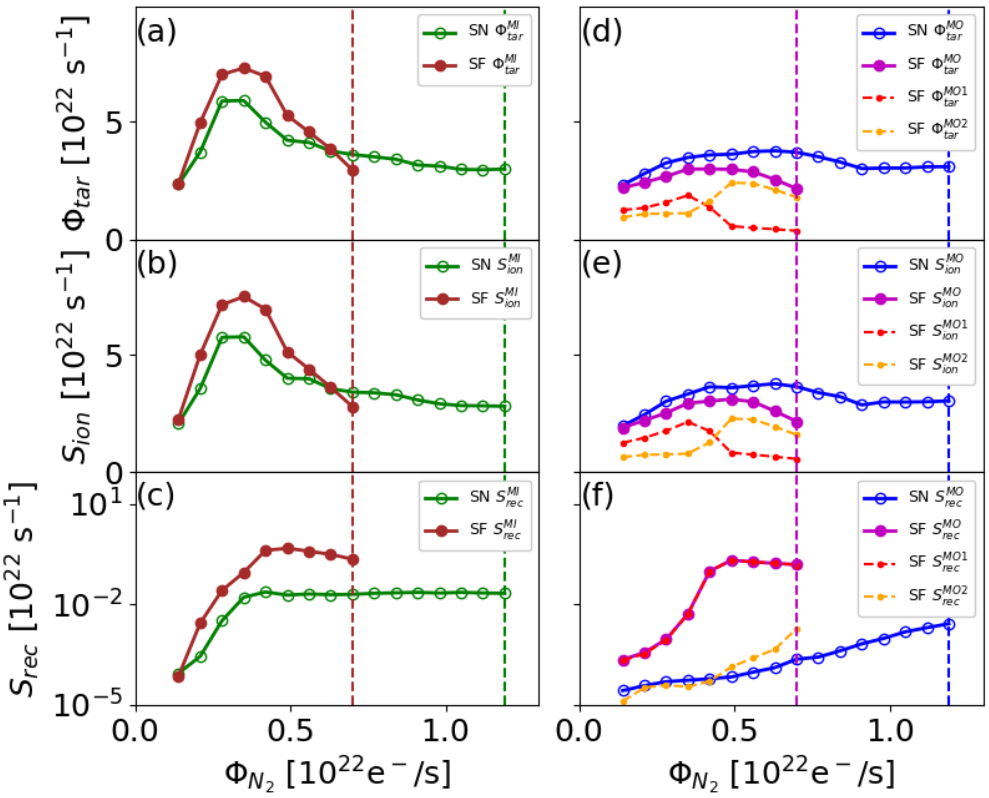

FIGURE 6.8: The particle balance. (a) Integral deuterium ion particle flux at the target, Φ_{tar}; (b) total ionization source, S_{ion}, and (c) total volumetric recombination source, S_{rec} in the regions MI (left column) and MO (right column).

than that into the outer one ($P_{up}^{MI} < P_{up}^{MO}$). This asymmetry between the inner and outer divertors has been widely observed in tokamak experiments [56]. In scans of upstream density or impurity seeding rate, the inner target usually shows an earlier onset and a higher degree of detachment [20]. The underlying physics has not been completely understood so far. The main reason could be explained by the effect of drifts and the ballooning nature of the edge plasma transport combined with the difference between the connection lengths from the outer mid-plane to the inner and outer divertor targets [37]. The drifts are not included in the simulations in this chapter but will be discussed in chapter 8.

In the snowflake configuration, the power distribution between P_{up}^{MO} and P_{up}^{MI} is more balanced compared to the single null case, i.e. slightly lower $P_{up,SF}^{MO}$ than $P_{up,SN}^{MO}$ and slightly higher $P_{up,SF}^{MI}$ than $P_{up,SN}^{MI}$. The reason could be that the existence of the secondary X-point in the low-field side SOL increases the connection length in this region (see Fig.5.4) and reduces the difference

between the connection lengths to the inner and outer targets. In the following, we discuss the power and particle balance in the SOL regions from the outer mid-plane to the inner target (MI) and to the outer target (MO) separately.

6.2.1 Inner divertor

As shown in Fig. 6.7, the radiative dissipation in the inner divertor P_{rad}^{MI} increases with the increasing nitrogen seeding rates, leading to less power to the inner target, lower temperature and higher density there. The ionization rate becomes higher in the high-density region and further increases the density. Due to this positive feedback loop, the ionization particle source increases quickly and dominates the particle flux to the target (see cases with $\Phi_{N_2} = 1.4$–2.8×10^{21} e^-/s in Fig. 6.8 (a) and (b)). As introduced in section 3.3, such a situation is named high-recycling regime. As discussed in Ref. [90], with increasing recycling in the inner divertor, a reversed convective power flow from the inner divertor to the outer one develops (i.e. P_{omp}^{MO} in Fig.6.6 increases), resulting in a decrease of P_{up}^{MI} and an increase of P_{up}^{MO} (see Fig. 6.7 (b) and (e)). This contributes to a further decrease of the integrated power flux to the inner divertor target.

When more impurities are puffed ($\Phi_{N_2} > 3.5 \times 10^{21}$ e^-/s), more power is radiated before reaching the ionization region in front of the divertor target. The rest of the power becomes too low to sustain so many ionization processes, such that S_{ion}^{MI} decreases. Since Φ_{tar}^{MI} is dominated by S_{ion}^{MI}, Φ_{tar}^{MI} also decreases and shows a roll-over feature (see Fig. 6.8 (a)), which is considered to be a signature of divertor detachment. Different from that in section 6.1, Φ_{tar} is the particle flux integrated over the target surface. The roll-over of Φ_{tar} indicates the detachment feature of the whole target but not a specific flux tube. In other simulation studies [90], the volumetric recombination also plays an important role in the roll-over of the particle flux. However, in this scan, the temperature in the divertor is still higher than the typical value for the volumetric recombination (1 eV), so the volumetric recombination rate is still relatively small (see Fig. 6.8 (c)).

In the snowflake configuration, the integrated target particle flux ($\Phi_{tar,SF}^{MI}$) rolls over at a similar seeding rate as the one in the single null configuration. However, the maximum ionization source during the scan is larger in the snowflake case (see Fig. 6.8 (b)). In addition to that, the target power flux ($P_{tar,SF}^{MI}$) decreases faster and becomes slightly lower than $P_{tar,SN}^{MI}$ in Fig. 6.7 (a) before the upstream pressure degradation. This implies that the snowflake configuration also influences the power exhaust in the inner divertor. On the one hand, the connection length to the inner target is slightly longer in the snowflake configuration (see Fig. 5.4). On the other hand, the interaction be-

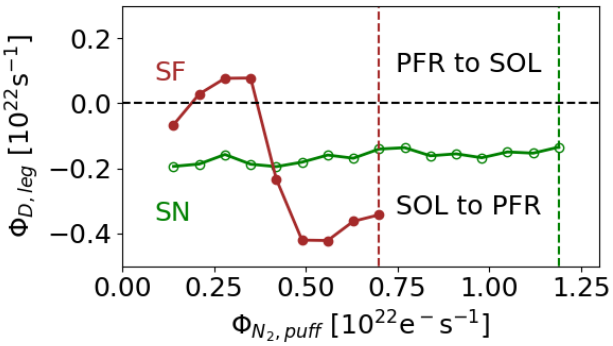

FIGURE 6.9: The neutral flux across the inner divertor leg. Positive values are for a flux from the private flux region into the SOL.

tween the inner and outer divertors via neutral particles can also contribute to the lower power flux at the inner target.

Figure 6.9 shows the neutral deuterium particle flux across the inner divertor leg. In the single null case, the values are negative, indicating a net neutral particle flux from the SOL to the private flux region. The inner divertor usually enters the high recycling regime earlier than the outer divertor in the single null configuration. Part of the recycled neutrals from the inner divertor travel through the private flux region and increase the ionization source in the outer divertor, which is considered to play an important role for the outer divertor detachment [90]. However, in the snowflake case, the outer target OT1 enters the high recycling regime nearly simultaneously with the inner target (see Fig. 6.8 (a) and (d) where the roll-over occurs at $\Phi_{N_2} = 3.5 \times 10^{21}$ e$^-$/s). The neutral flux from the outer divertor remits the flux from the inner divertor or even reverses it, as shown in Fig. 6.9 at low seeding rates. The neutral flux into the inner divertor increases the ionization source, contributing to the faster increase of $S^{MI}_{ion,SF}$ in Fig. 6.8 (b) and the broader profiles of the particle flux and density in Fig. 6.2 (c) and (d). After OT1 achieves a high degree of detachment ($\Phi_{N_2} > 4.9 \times 10^{21}$ e$^-$/s), the recycling there returns to a low level. Then the neutral flux reverses its direction and becomes even stronger than that in the single null case where the recycling is still high in the outer divertor. This leads to a faster decrease of $S^{MI}_{ion,SF}$ and $\Phi^{MI}_{tar,SF}$ at the inner target in the snowflake divertor in Fig. 6.8 (a) and (b) compared to the single null reference. The stronger neutral flux leaving the SOL in the snowflake case is beneficial for achieving a higher volumetric recombination rate near the inner target, as shown in Fig. 6.8 (c) and Fig. 6.5 (d). Thus, the different detachment evolution in the outer divertors could cause different behaviours in the inner divertors in these two configurations.

In order to test this hypothesis, the numerical experiment was carried out

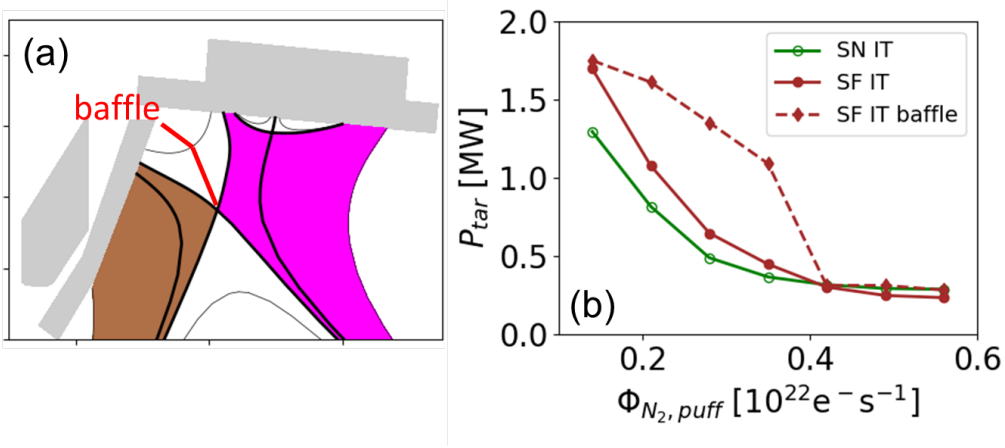

FIGURE 6.10: (a) The baffle in the private flux region of the snowflake divertor. (b) The integrated power at the inner target. The solid lines show the cases without a baffle, while the dashed line show that with a baffle in the snowflake divertor.

by introducing an artificial baffle in the private flux region in the snowflake grids. The baffle shown in Fig. 6.10 (a) prevents the neutral particle transport between the inner and outer divertor while it is not interacting directly with the plasma. Obviously such a target can only exist in simulations. The evolution of the power at the inner target P_{tar}^{MI} in the presence of the baffle is shown in Fig. 6.10 (b). Compared to the case without baffle, the power at the inner target $P_{tar,SF}^{MI}$ decreases slower in the case with baffle and finally shows nearly no difference from that in the single null case $P_{tar,SN}^{MI}$ at high seeding rates ($\Phi_{N_2} \geq 4.2 \times 10^{21}$ e$^-$/s).

6.2.2 Outer divertor

In the outer divertor, the two magnetic configurations behave dramatically different, especially in the near SOL. As shown in chapter 5, the larger connection length and radiation volume lead to a substantially higher total amount of radiation and volumetric recombination in the snowflake configuration. Together with the SOL splitting effect, this results in a substantially lower target power load compared to the single null configuration. The power and particle balances in the SOL region from the outer mid-plane to the outer targets (MO) are shown in the right columns in Figs. 6.7 and 6.8. The lower target power flux, the earlier roll-over of the target particle flux, as well as the higher radiation and volumetric recombination rates in the whole range of the nitrogen seeding scan, can be seen clearly in the snowflake case compared to the single null case.

In the single null configuration, during the scan from $\Phi_{N_2} = 1.4 \times 10^{21}$ e$^-$/s to 2.8×10^{21} e$^-$/s, the power into the MO region $P_{up,SN}^{MO}$ increases due to the

reversed power flow from the high-recycling inner divertor. Since the temperature in the outer divertor is still high, the radiation rate remains low (see Fig. 6.7 (f)). As a result, the power flux to the outer target $P^{MO}_{tar,SN}$ increases. After the particle flux roll-over at the inner target ($\Phi_{N_2} > 3.5 \times 10^{21}$ e$^-$/s), the reversed power flow becomes weaker and $P^{MO}_{up,SN}$ decreases to the value at the beginning of the scan. When the temperature is low enough, the radiation power starts to increase and to reduce $P^{MO}_{tar,SN}$ further. The integrated particle flux at the target ($\Phi^{MO}_{tar,SN}$) is dominated by the ionization source ($S^{MO}_{ion,SN}$) and shows a roll-over at a seeding rate of about 6.3×10^{21} e$^-$/s. Since the temperature at the outer target is still above 1 eV, the volumetric recombination is still relatively small, $\Phi^{MO}_{tar,SN}$ cannot be reduced further and stays nearly constant until the upstream pressure degradation sets in (see Fig. 6.8 (d)).

In the snowflake configuration, the larger connection length results in a lower temperature in the outer divertor region. The temperature reaches the radiation window at a lower nitrogen seeding rate. The larger radiation volume enhances the total radiation power, especially in the high-density region near OT1. As shown in Fig. 6.7 (f), the total radiation power in the near-SOL region (MO1) ($P^{MO1}_{rad,SF}$) increases quickly with the nitrogen seeding and leads to a quick drop of power flux to OT1 (see Fig. 6.7 (d)). The ionization source ($S^{MO1}_{ion,SF}$) in Fig. 6.8 (d) increases in the high recycling regime and then decreases because of the lack of power. The roll-over of $\Phi^{MO1}_{tar,SF}$ occurs at a similar seeding rate as the roll-over at the inner target. The high recycling behaviour at OT1 tends to cancel the reversed power flux from the inner divertor. As shown in Fig. 6.7 (b), $P^{MO1}_{up,SF}$ is nearly constant and not influenced by the evolution in the inner divertor. The larger connection length, lower temperature and higher density also enhance the volumetric recombination significantly in the MO1 region (see Fig. 6.8 (f)), which contributes to the further reduction of $\Phi^{MO1}_{tar,SF}$. The total volumetric recombination rate is more than one magnitude higher than the one in the single null configuration.

In the far-SOL region (MO2), the enhancement of the connection length is not so large as that in the near SOL (MO1). However, the radiation volume is still larger than that in the single null case due to the flux flaring. At low seeding rates, some radiation is found in the far SOL near OT2 (see Figs. 6.3 (c) and 6.7 (f)) due to the larger volume with suitable temperature. When the temperature near OT1 drops into the interval where nitrogen strongly emits radiation, the radiation in the far SOL decreases slightly. Since the target temperature near the strike point at OT2 is still high, the recycling there is low, and the ionization source $S^{MO2}_{ion,SF}$ does not change that much. After the detachment of OT1, the temperature is too low for nitrogen to radiate, and the radiation region expands to MO2. As shown in Fig. 6.7 (f), the radiation power $P^{MO2}_{rad,SF}$ increases again due to the contribution from the region around

the secondary X-point (see Figs. 6.5 (c)). The integrated power ($P_{tar,SF}^{MO2}$) and temperature at OT2 decrease as a consequence. The recycling at OT2 increases as shown by $\Phi_{tar,SF}^{MO2}$ in Fig. 6.8 (d). The integrated target particle flux at OT2 shows a roll-over at a seeding rate about 4.9×10^{21} e^-/s, later than at OT1 while still earlier than at the outer target in the single null configuration.

In an open single null divertor, it is typically quite hard to achieve detachment at the outer part of the outer target. The high recycling region and radiation are more concentrated near the strike point, and it is difficult to reduce the power flux and temperature to a sufficiently low value in the far SOL. In our scan, it is found that the hot outer part of OT can even encumber the detachment in the inner part. The temperature decreases slowly with the seeding scan and cannot reach a suitable value for volumetric recombination before upstream pressure degradation sets in. In the snowflake configuration, the outer targets OT1 and OT2 are separated. The inner part of the outer target (OT1) is not influenced by the outer one (OT2) directly. So OT1 can achieve a high degree of detachment with considerable volumetric recombination at a lower seeding rate. At the same time, the larger radiation volume and the expanded radiation region near the secondary X-point contribute to a reduction of the power flux and temperature at OT2, leading to an earlier detachment compared to the single null case. This is also one of the advantages of the low-filed side snowflake minus configuration found in this scan.

6.3 Summary

In this chapter, we compared the simulations in the single null (SN) and low-field side snowflake minus (LFS SF^-) configurations with a nitrogen impurity seeding rate scan. Compared to the single null reference with similar upstream densities, the snowflake cases showed higher radiative power fractions in the whole scan. This proves the robustness and universality of the findings in chapter 5. The outer targets in the snowflake configuration, especially the one connected to the primary X-point (OT1), detached at a lower nitrogen seeding rate compared to the single null reference. In addition to that, the earlier detached outer target could also influence the neutral particle flux in the private flux region between the inner and outer divertor, contributing to a lower power flux at the inner target. Although upstream pressure degradation, which could lead to a confinement degradation, was also found in the snowflake configuration at sufficiently high seeding rates, lower power loads and pressures at the targets, i.e. a higher degree of divertor detachment, were achieved before the degradation sets in.

Chapter 7

Predictions for the future ASDEX Upgrade divertor based on experimental data

In the simulations presented in previous chapters, we were interested in the effect of the geometry alone, while keeping the assumptions on transport simple. For this reason, we assumed spatially and temporarily constant transport coefficients. This facilitates the achievement of similar upstream profiles in various divertor configurations. Since the upstream parameters influence the divertor condition directly, it is important to keep the upstream profiles similar when studying the effect of the divertor geometry. In addition to that, simulations with spatially constant transport coefficients are numerically more stable. However, a precise fit to experimental measurements requires spatially varying transport coefficients, especially for H-mode discharges with a transport barrier at the edge of the confinement region. The transport coefficients in these barriers can be one order of magnitude lower than those in the SOL [91]. In this chapter, the transport coefficients were adjusted iteratively in SOLPS-ITER to match recent AUG H-mode experiments in upper single null configuration. With the same transport coefficients, predictions of the performance of alternative divertor configurations (ADCs) in the future upper divertor were made.

7.1 Experiments and simulations setup

The goal of the experiments was to characterise the upper single null configuration in AUG and to prepare the upper divertor upgrade. The experiment was carried out with a plasma current of $I_p = 0.8$ MA and a toroidal magnetic field of $B_T = +2.5$ T ($\vec{B} \times \nabla B$ ion drift pointed to the upper divertor).

The time evolution of the main plasma parameters is shown in Fig. 7.1. The electron cyclotron resonance heating (ECRH) power was constant at 2.5 MW during the entire flattop phase, and the neutral beam injection (NBI) heating power was ramped in three steps to 2.5, 5.0 and 7.5 MW as shown in Fig. 7.1 (b). The deuterium was fueled from the lower divertor roof baffle at the beginning of the discharge, leading to the slightly decreasing line integrated density shown in Fig. 7.1 (c). The main impurity was nitrogen, puffed in previous discharges that still remained in the machine. The confinement factor based on the IPB98(y,2) scaling [92] was $H_{98} \approx 1$ and type-I ELMs visible in the H_α emission signals indicate that the discharge was in H-mode. We chose a stable time phase from 3.1 s to 3.9 s for the comparison with SOLPS simulations.

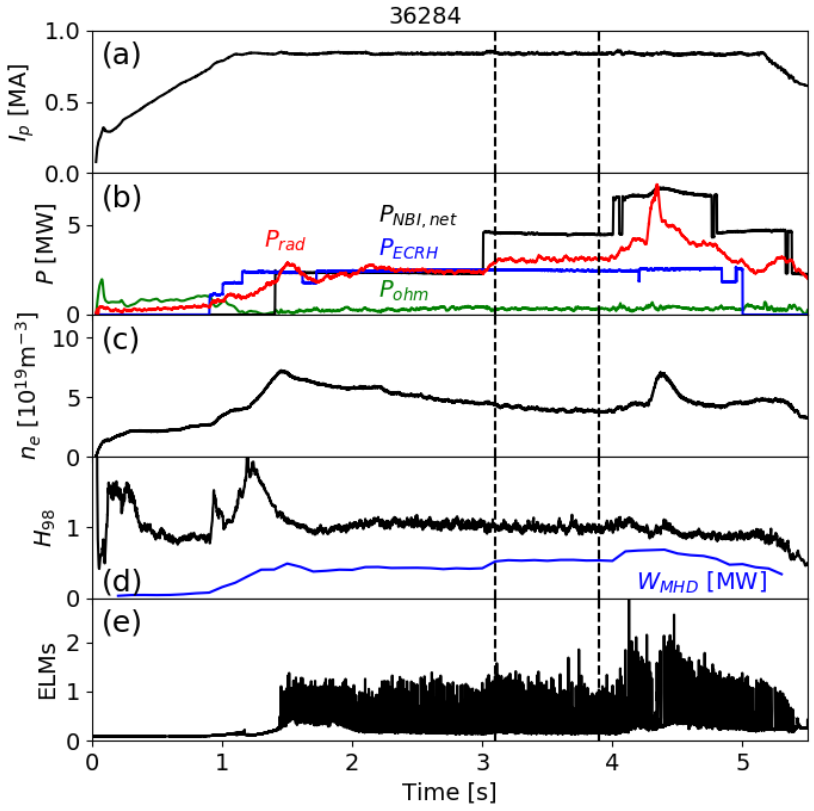

FIGURE 7.1: Time evolution of (a) plasma current, (b) heating and radiation power, (c) core line integrated density, (d) H_{98} confinement factor and plasma stored energy W_{MHD} and (e) H_α emission measured by the fast camera. The time phase between the vertical dashed lines was used for the comparison with SOLPS simulations.

The magnetic equilibrium at 3.5 s and important diagnostics are shown in Fig. 7.2 (a). The computational grids for the SOLPS simulation were generated based on the experimental equilibrium (see Fig. 7.2 (b)). The injection positions of D_2 and N_2 in the simulations were the same as in the experiments.

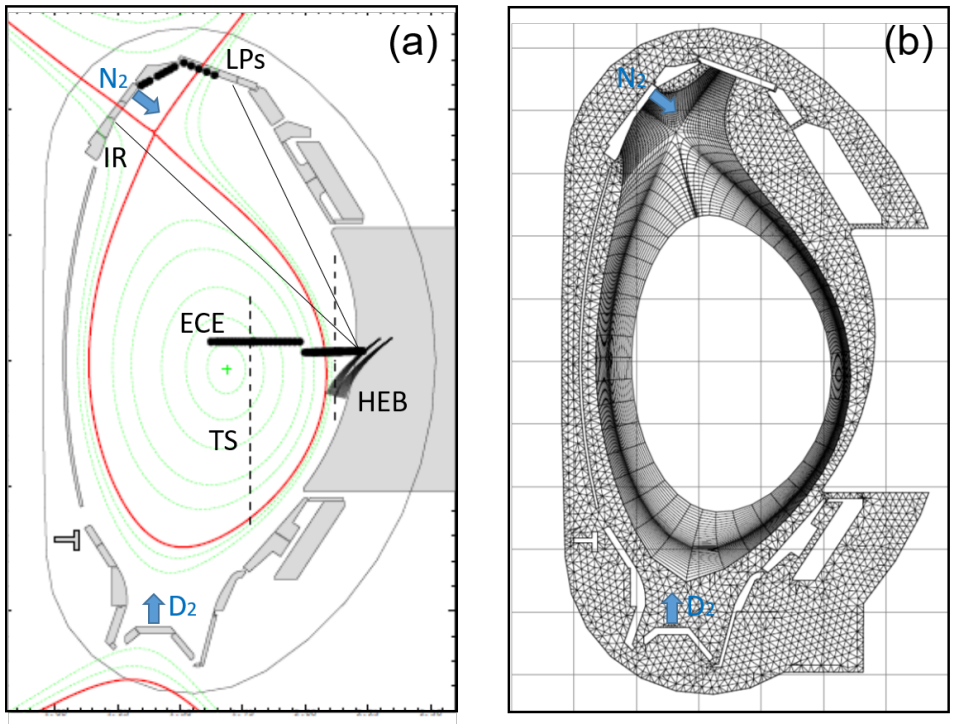

FIGURE 7.2: (a) The poloidal cross-section of the experimental equilibrium and positions of important diagnostics. (b) The SOLPS grids generated based on (a).

Figure 7.3 (a–c) shows the electron density, electron temperature and ion temperature measured during 3.1–3.9 s. The radial coordinates were mapped to the outer mid-plane (OMP). The electron density and temperature were measured by Core Thomson Scattering (CTS) and Electron Cyclotron Emission Radiometry (ECE, only for temperature) in the confinement region and by Helium Beam (HEB) emission spectroscopy and Edge Thomson Scattering (ETS) in the SOL. The ion temperature was measured by Charge-eXchange Recombination Spectroscopy (CXRS). The profiles calculated by the Integrated Data Analysis (IDA) [93], a tool combining several diagnostics in a coherent way, are also shown for reference. Figure 7.3 (d–e) shows the profiles of the electron density, temperature and ion saturation current measured by Langmuir Probes (LPs) at the outer target. Since the equilibrium in this experiment was moved down compared to the standard upper single null experiments in AUG to meet the requirements of the divertor upgrade, there was no Langmuir probe array around the inner strike point (see Fig. 7.2 (a)). However, the Infrared Camera (IR) was able to view both inner and outer targets simultaneously but with a reduced temporal resolution. Figure 7.4 shows the power flux perpendicular to the targets averaging over time intervals containing ELMs. Both targets were attached, while the perpendicular power flux at the inner target was lower due to the larger flux expansion there.

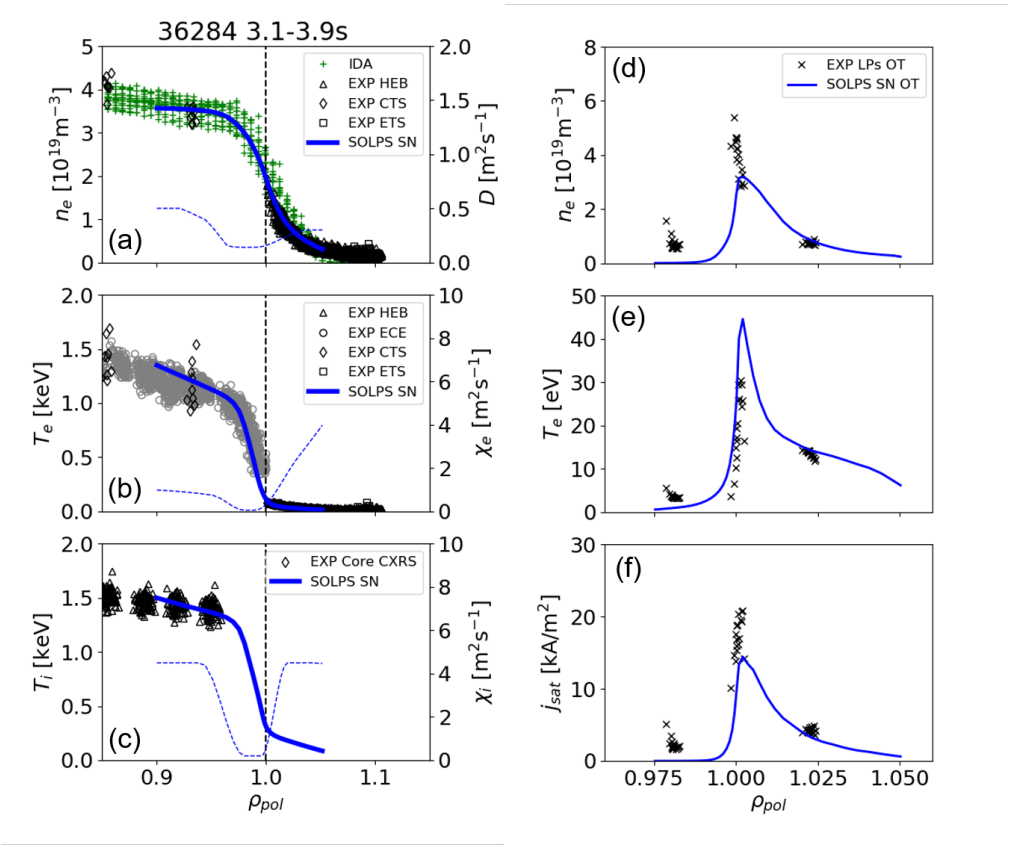

FIGURE 7.3: Outer mid-plane profiles of (a) electron density, (b) electron temperature, (c) ion temperature and outer target profiles of (d) electron density, (e) electron temperature, (f) ion saturation current, comparing between the experimental measurements and the SOLPS simulation. The blue solid and dashed curves show the parameter profiles reproduced by SOLPS and the transport coefficients used in the simulations, respectively.

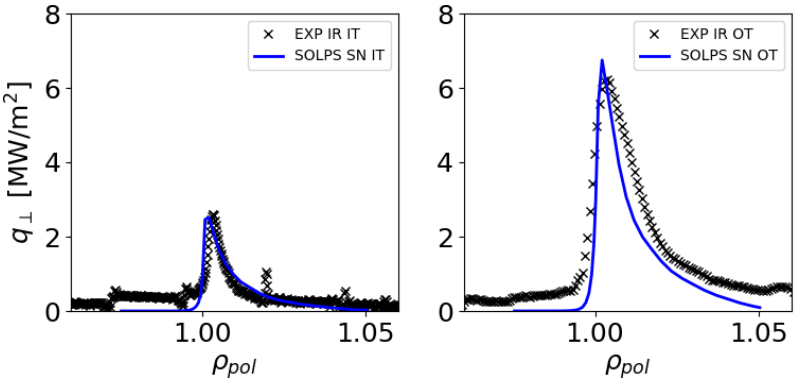

FIGURE 7.4: Power flux perpendicular to the inner (left) and outer (right) target from IR measurements and SOLPS simulations.

In the SOLPS simulations, the radially varying transport coefficients, boundary conditions and gas puffing rates were adapted iteratively to achieve the best overall fit of the experimental measurements at both the outer mid-plane and targets (see the solid curves in Fig. 7.3 and Fig. 7.4).

7.2 Extrapolation to the future upper divertor

The installation of the in-vessel divertor coils in the upper divertor is accompanied by a modification of the inner and outer targets (cf. Figs. 7.5 (a) and (b)). Before analysing the effect of different magnetic configurations, we should analyze the effect of the target geometry, e.g. the different divertor leg length and poloidal tilting angle at the target. For this purpose, we compared the SOLPS simulations in single null configuration with different target geometries shown in Figs. 7.5 (a) and (b).

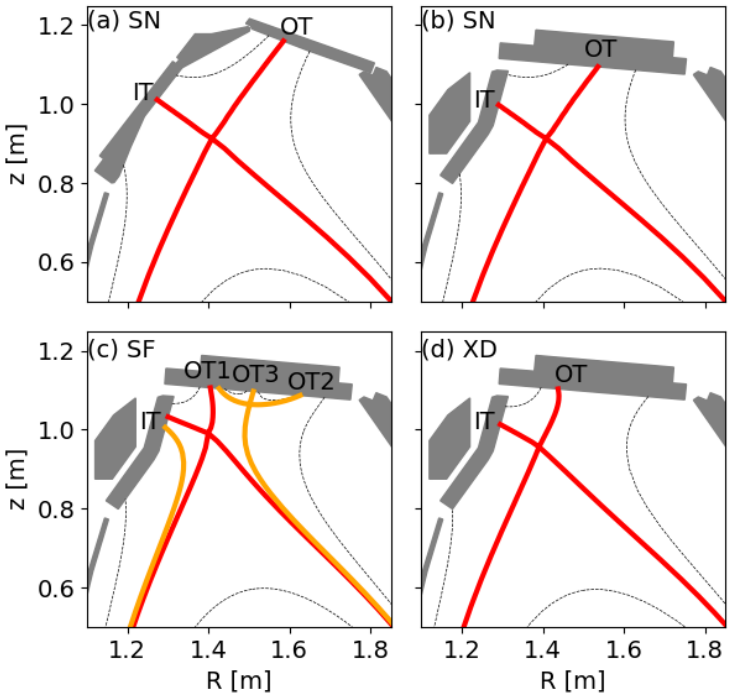

FIGURE 7.5: The steps of extrapolation. (a) The upper single null configuration with the present upper divertor targets in AUG. (b) The upper single null configuration, (c) the low-field side snowflake minus (LFS SF^-) configuration and (d) the X-divertor (XD) configuration with the future upper divertor targets.

Figures 7.6 (a–c) compare the upstream profiles in the simulations with the present and the future upper divertor target structures. The similar profiles indicate that the target geometry nearly has no impact on the upstream parameters in such plasma conditions.

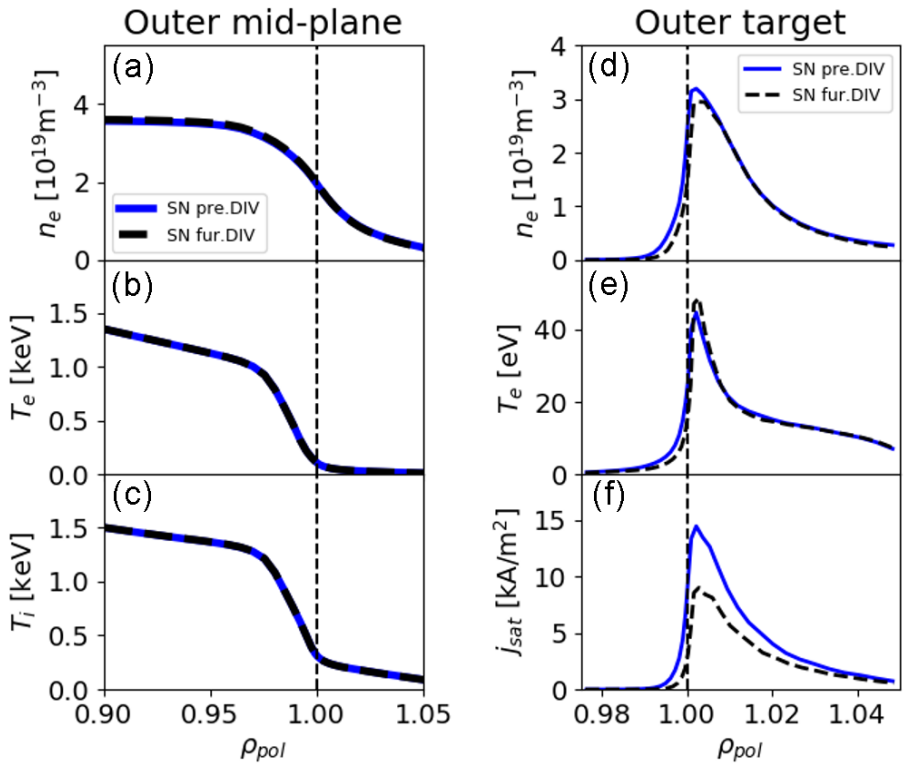

FIGURE 7.6: Same as Fig. 7.3, but comparing between the simulations in single null configuration with the present (blue) and future (black) divertor targets.

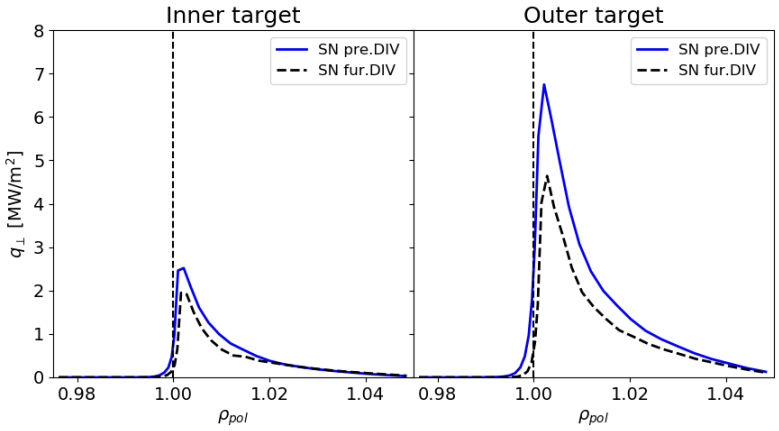

FIGURE 7.7: Same as Fig. 7.4, but comparing between the simulations in single null configuration with the present (blue) and future (black) divertor targets.

In Figs. 7.6 (d) and (e), the maximum density is slightly lower and the maximum temperature is slightly higher at the future outer target. This is due to the slightly shorter outer divertor leg in the future target geometry (cf. Fig. 7.5 (a) and (b)) which leads to a slightly shorter connection length given

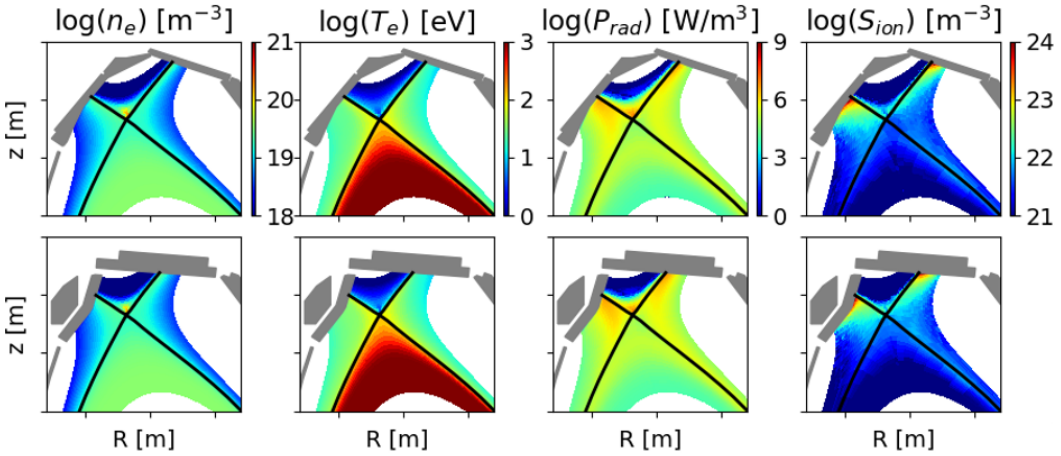

FIGURE 7.8: Two-dimensional distribution of electron density, electron temperature, radiation power, total pressure and ionization rate in the single null configuration with the present (upper row) and future (lower row) divertor targets.

the magnetic pitch is unchanged (see Eq. 3.2). The ion saturation current in Fig. 7.6 (f) and the power flux perpendicular to the target in Fig. 7.7 are both lower at the future targets. Since the target density and temperature are only slightly different for these two target geometries, the reduction of the power fluxes is caused by the target geometry effect and not by the change of recycling. As introduced in Eq. 3.6 in section 3.2, the poloidal angle between the poloidal projection of the magnetic field line and the target plate can directly influence the plasma-wetted area and in consequence, the quantities perpendicular to the target. As shown in Fig. 7.5 (b), the poloidal angle is smaller for the future inner and outer targets, resulting in a lower power flux perpendicular to the targets. Figure 7.8 shows a comparison of electron density, electron temperature, radiation rate, total pressure and ionization source in the divertor region. The divertor conditions turn out to be similar in the simulations with the present and future divertor targets.

In order to predict the performance of alternative divertor configurations in the future upper divertor, the simulations in single null configuration were extrapolated to those in the snowflake and X-divertor configurations by using the same transport coefficients, boundary conditions and gas puffing rates.

7.2.1 Snowflake divertor

In the following, we show the extrapolation for a snowflake divertor. As shown in Fig. 7.5 (b) and (c), the target geometries were kept the same while the magnetic configuration was changed from single null to a low-field side snowflake minus (LFS SF$^-$) configuration. The electron density profiles at the outer mid-

plane in these two configurations are compared in Fig. 7.9 (a). The snowflake case shows higher electron densities in the confinement region compared to the single null case. As mentioned in section 3.5, the two nearby X-points in the snowflake configuration modify the magnetic pitch angle and influence the particle transport. In Fig. 7.9 (b) and (c), the upstream profiles of electron and ion temperatures are found similar in both confinement region and SOL in these two configurations.

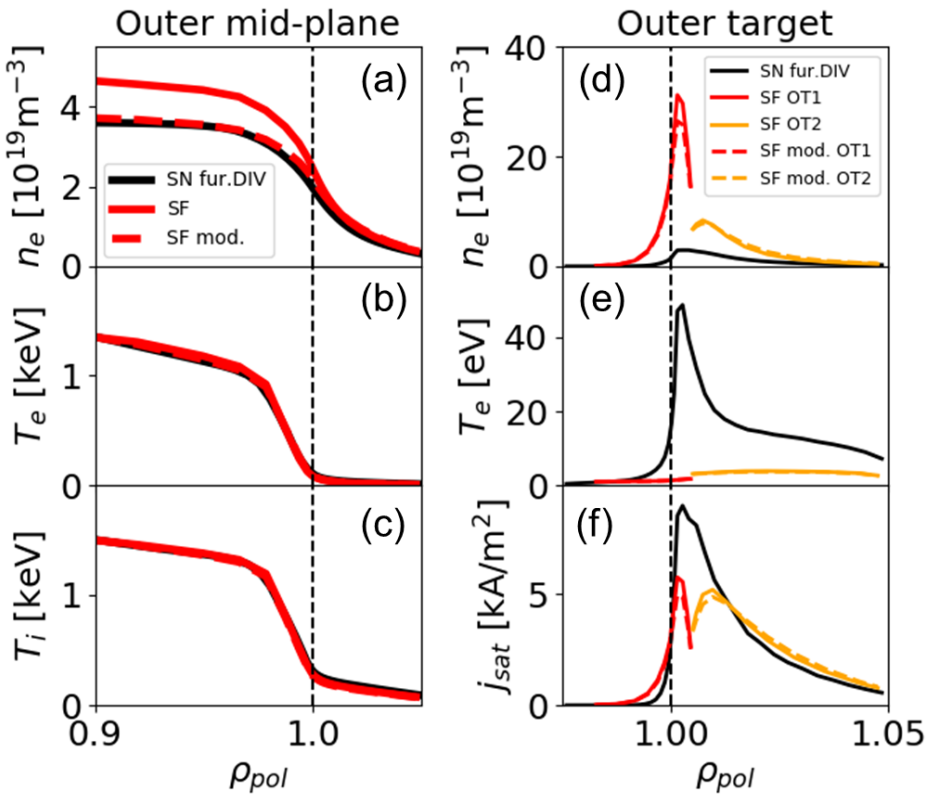

FIGURE 7.9: Same as Fig. 7.3, but comparing between the simulations in the single null and snowflake configurations with the future target geometry. The black solid lines show the single null case. The red (outer mid-plane and OT1) and orange (OT2) solid lines show the snowflake case with the same transport coefficients as the single null case, while dashed lines show the case with modified transport coefficients in the confinement region to achieve similar upstream profiles.

At the outer target, the snowflake case shows substantially higher density and lower temperature compared to the single null case (see Fig. 7.9 (d) and (e)). In the two-dimensional cross-sections shown in Fig. 7.10, a region with high density, low temperature and high radiation rate forms near the primary X-point, similar to the X-point radiator found in the lower single null experiments in AUG and JET [94]. As a result, the power fluxes are reduced by about one order of magnitude at both inner and outer targets compared to

the single null case (see Fig. 7.11). The smaller magnetic pitch angle near the X-points in the snowflake configuration could facilitate the maintenance of the strong poloidal temperature gradient near the radiator. This could also be an attractive benefit of the snowflake divertor configuration and is foreseen to be tested in future experiments. The ionization regions are located near the targets in the single null case, while they move to the X-points and become weaker in the snowflake configuration (cf. Figs. 7.8 and 7.10). The lower ion saturation currents shown in Fig. 7.9 (f) also indicate lower ion particle fluxes at the outer targets in the snowflake case.

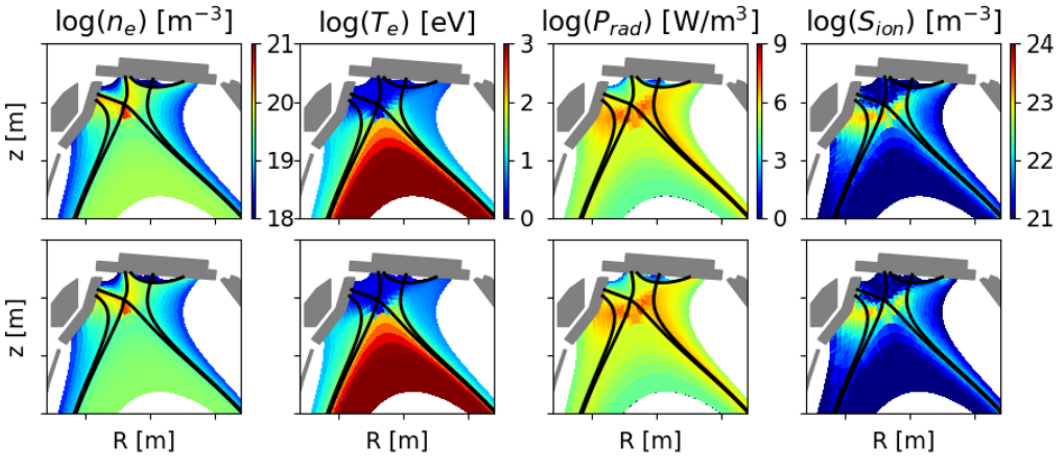

FIGURE 7.10: Same as Fig. 7.8, but the upper row shows the snowflake case with the same transport coefficients as those used in the single null cases, while the lower row shows the case with modified transport coefficients to achieve similar upstream profiles.

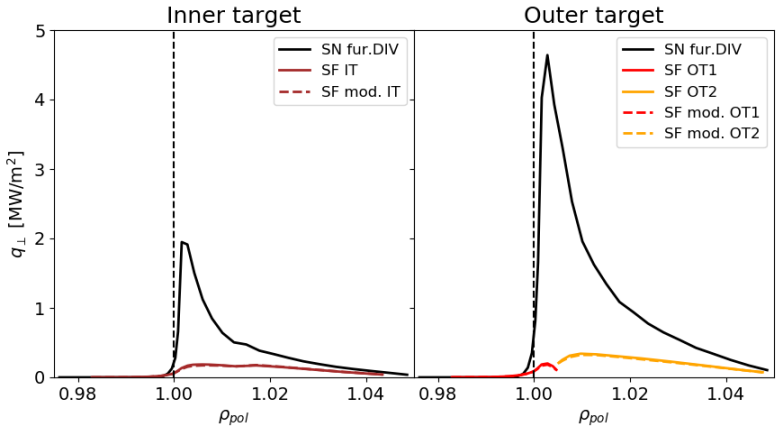

FIGURE 7.11: The power fluxes at the (a) inner and (b) outer divertor targets. The meaning of color and line-style is the same as Fig. 7.9.

In order to study the influence of the higher upstream density in the confinement region, the transport coefficients in the snowflake case are adjusted to achieve a similar density profile to the one in the single null case. The profiles at the outer mid-plane and the target are shown in Figs. 7.9 and 7.11 by dashed lines. Comparing these two snowflake cases, no significant change is found at the target. This means that the different divertor conditions in the single null and snowflake simulations are not caused by the higher density in the confinement region.

Analysis of power and pressure balances

Compared to SOLPS5.0, the SOLPS-ITER code package contains more powerful post-processing scripts. This makes it possible to analyze the power and pressure balances between the upstream and downstream positions in detail. In a flux tube, the differences of power flux and pressure between the upstream position and the target are caused by various mechanisms, e.g. cross-field (radial) transport, volume processes, viscosity and forces. The full expressions of the power and momentum transport in SOLPS are introduced in chapter 4. In numerical simulations, there are also terms caused by boundary conditions and numerical corrections. However, in converged cases with proper settings, the numerical terms are usually negligible.

Figures 7.12 (a) and (b) show the radial profiles of the upstream and target power fluxes in the single null and snowflake configurations, respectively. The upstream power flux relates to the power from the confined region transported radially into the flux tube. Figures 7.12 (c) and (d) show the power sinks integrated over the flux tube from the outer mid-plane to the outer targets. The term 'radial transport' indicates that the power flux transported radially into the private flux region or to the chamber wall. The term 'volume processes' refers to the power dissipated via volume processes (mainly via impurity radiation). The rest of the terms corresponds to the power loss related to the velocity gradient (see Eq. 4.7), viscosity and friction.

In the single null case, the parallel power flux to the target is reduced by about 50 % in the flux tube near the separatrix. Figure 7.12 (c) indicates that the reduction is mainly caused by radial transport into the private flux region. In the far SOL region, all power sinks are so small that there is nearly no difference between the upstream and target profiles. In the snowflake case, the upstream power flux profile is similar to that in the single null configuration. However, the power fluxes are much lower at the whole outer target including OT1 and OT2. As shown in Fig. 7.12 (d), the power sink is dominated by volume processes which are much higher than that in the single null case. Most of the power is dissipated in the high-radiative region near the X-points

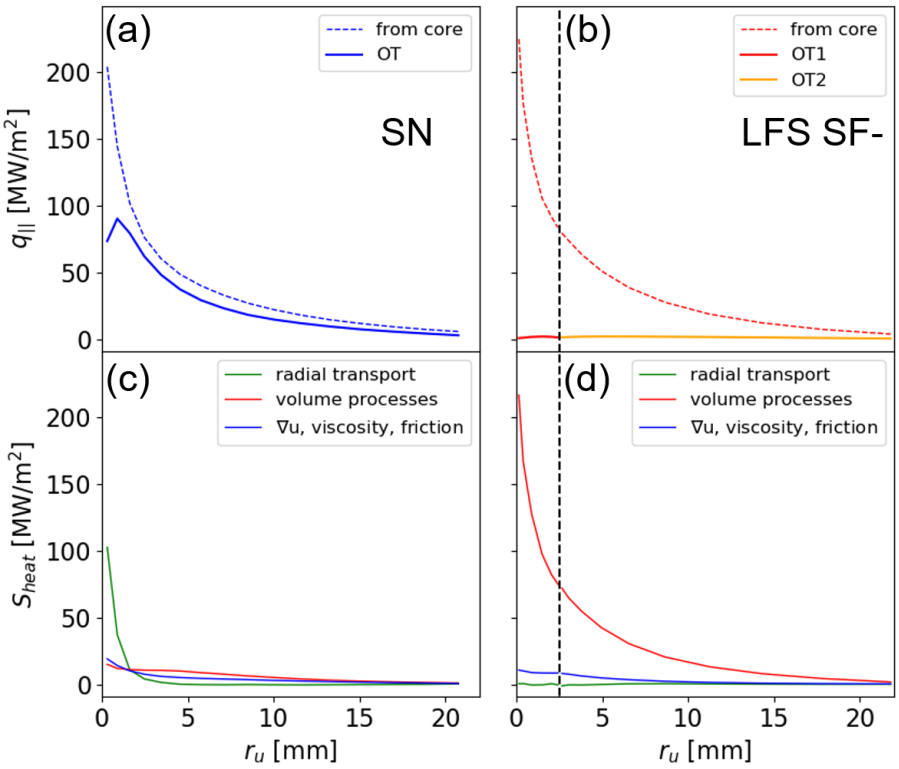

FIGURE 7.12: Power balance between the outer mid-plane and outer targets as function of the radial distance from the separatrix at the outer mid-plane.

shown in Fig. 7.10. Since the power from the upstream position is dissipated before entering the divertor region, the power transported into the private flux region (the sink due to 'radial transport') is quite low in the snowflake configuration.

Figure 7.13 (a) shows radial profiles of the total pressure at the outer mid-plane and the outer target in the single null configuration. The pressure sinks are shown in Fig. 7.13 (c). In the region close to the separatrix, a pressure loss between the outer mid-plane and outer target is found. This is mainly due to radial transport into the private flux region. Since the temperature in the outer divertor region is higher than 10 eV, the charge exchange and volumetric recombination rates are very low compared to the ionization rate. As a result, the pressure sink related volume processes is small. In the region $1 < r_u < 5$ mm, the pressure at the outer target is even slightly higher than that at the outer mid-plane. This is found to be caused by parallel viscosity.

In the single null case, the ionizing region is close to the target (see Fig. 7.8), and there is no significant particle source from the outer mid-plane to the ionization front. The particle flux is nearly stagnated in the upstream region

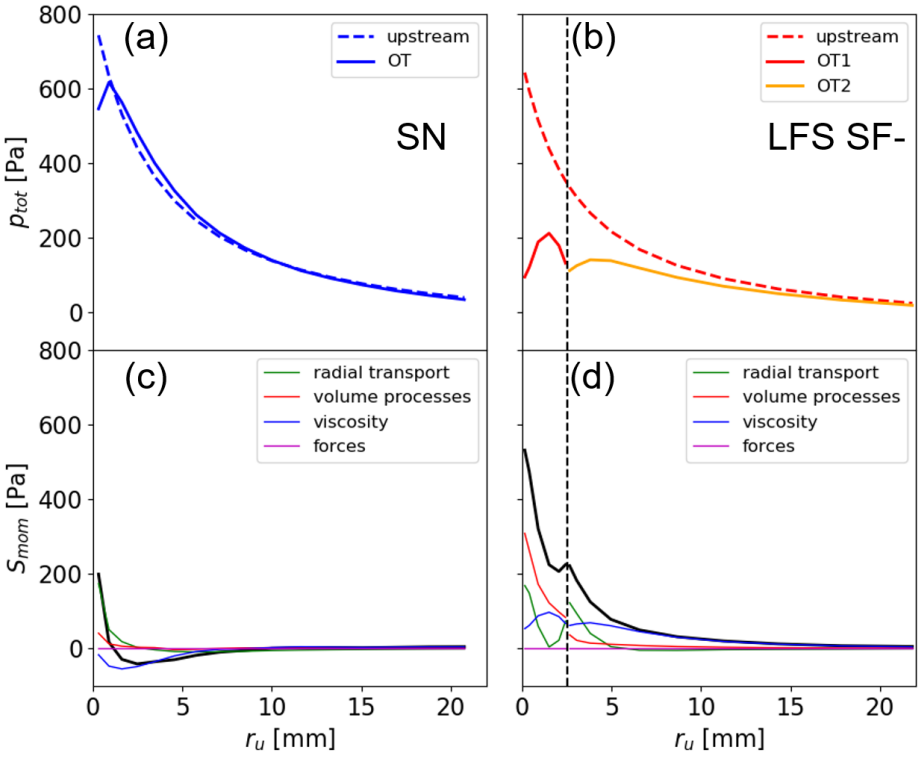

FIGURE 7.13: Pressure balance between the outer mid-plane and outer targets. The black lines in (c) and (d) show the total pressure sink. The radial position of the secondary separatrix in the snowflake configuration is shown by the verticle dashed lines in (b) and (d).

and accelerated to the local sound speed at the target to fulfil the sheath condition. The nonlinear acceleration (the parallel velocity profile along the flux tube features a concave function) results in a source of pressure via parallel viscosity. The sink related to forces is small because the effects of friction and thermal forces are nearly cancelled when summing over all species. In the far SOL region, there is nearly no difference between the pressure at the outer mid-plane and the outer target in the single null configuration.

The pressure analysis in the snowflake configuration is shown in Figs. 7.13 (b) and (d). A substantial pressure loss can be seen along the whole target plate, indicating that the target is detached. Since the density is high and the temperature is sufficiently low in the outer divertor, the charge exchange and volumetric recombination rates are much higher than those in the single null case. As shown in Fig. 7.13 (d), the volumetric processes play an important role for the pressure drop. Besides this, the existence of the secondary separatrix causes an additional pressure removal via radial transport into the regions R1

and R2 (see Fig. 4.3) across the secondary divertor legs. In the snowflake case, the ionizing region moves to the region around the primary X-point (see Fig. 7.10), and the large ionization particle source impact the flows in the divertor region. Compared to the single null case, the sound speed at the target is lower due to the lower target temperature. The parallel velocity profile shows a convex function near the ionizing region, causing an integrated pressure sink related to parallel viscosity.

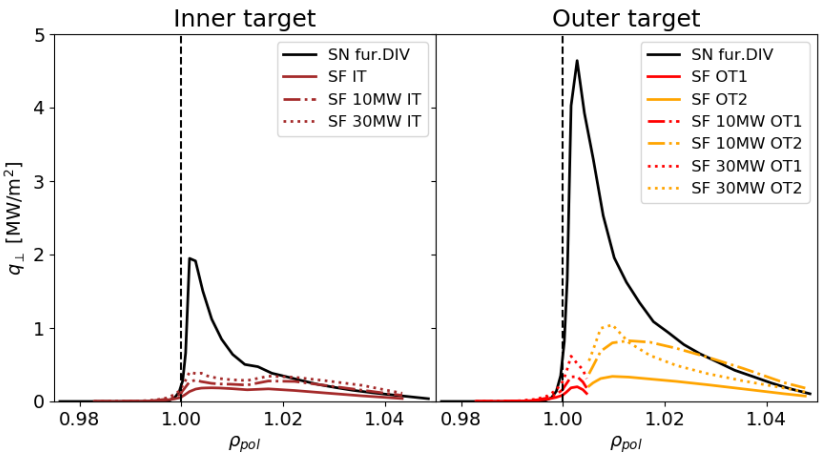

FIGURE 7.14: The power fluxes at the (a) inner and (b) outer divertor targets. The dash-dot and dotted lines show the snowflake cases with input power of 10 MW and 30 MW, respectively.

In order to test the performance of the snowflake configuration at higher heating power, we increased the input power at the innermost radial boundary to 10 MW and 30 MW. The target power fluxes are shown in Fig. 7.14, comparing with the above-analyzed single null and snowflake cases. Although the input power (30 MW) is reaching the maximum heating power of AUG (see Tab. 2.1 in chapter 2), the maximum power flux perpendicular to the outer target in the snowflake configuration is still a factor of 4 lower than that in the single null configuration. This means the snowflake divertor (LFS SF$^-$) can allow to operate at a much higher heating power and may extend the operational window in the future devices. It should be pointed out that the increased input power also results in a factor of 2 higher separatrix density in the simulation. The higher upstream density also contributes to the reduction of the power flux at the target.

7.2.2 X-divertor

For completeness, the X-divertor configuration in the future upper divertor (see Figs. 7.5 (d)) is also studied. The simulation results are shown in Figs. 7.15,

7.16 and 7.17.

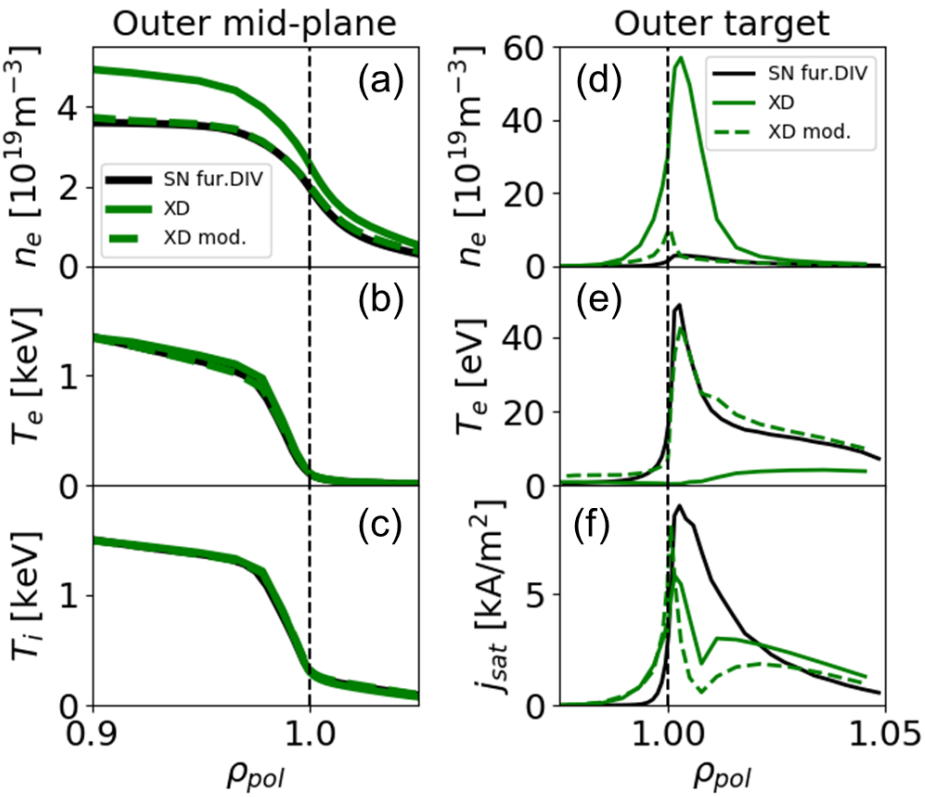

FIGURE 7.15: Same as Fig. 7.9, but comparing between the simulations for single null (black) and X-divertor (green) configurations in the future upper divertor. The green solid lines show the X-divertor case with the same transport coefficients and gas puffing rates as those in the single null case, while the dashed lines show the X-divertor case where the transport coefficients and fueling rates are modified to achieve similar upstream profiles as those in the single null case.

Comparing to the single null case with the same transport coefficients and gas puffing rates, the simulation predicts higher electron densities at the outer mid-plane in the X-divertor configuration (see Fig. 7.15 (a)). Different from the snowflake case shown in the previous section, the density in the X-divertor case is higher not only in the confinement region, but also in the SOL. Since the fueling rates are kept the same, the additional particle source for the higher density in the SOL is the ionization of the recycling particles (see the plot of ionization rates in the upper row in Fig. 7.17). At the outer target, the maximum electron density reaches 5.7×10^{20} m^{-3} which is a factor of 19 higher than that in the single null case (see Fig. 7.15 (d)). This is a result of the combination of the higher upstream density and the effect of the divertor configuration. A reference simulation for the X-divertor with the pump switched off predicted a density in the confinement region reaching the Greenwald density limit [95].

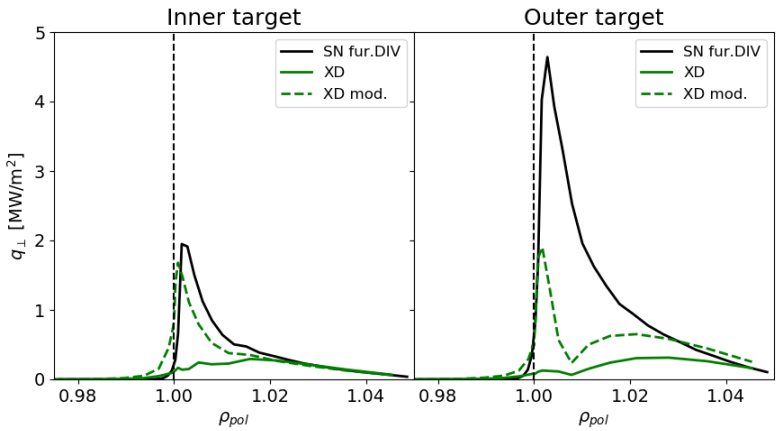

FIGURE 7.16: Power flux perpendicular to the inner (left) and outer (right) target. Similar to Fig. 7.15

For this reason, the pump could be essential in the future experimental operation for density control. In Fig. 7.15 (e), the target temperature is about 1 eV near the strike point, i.e. much lower than that in the single null case, indicating a partially detached outer target in the X-divertor case. Compared to the single null case, the maximum power fluxes shown in Fig. 7.16 are reduced by factors of 7 and 15 at the inner and outer targets, respectively.

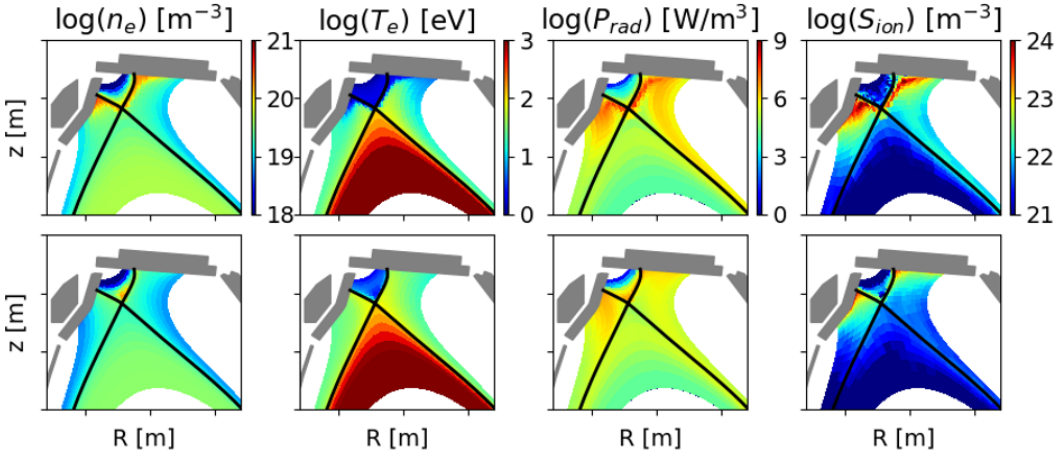

FIGURE 7.17: Same as Fig. 7.10, but for the XD configuration. The upper row shows the X-divertor case with the same transport coefficients as those used in the single null simulations, while the lower row shows the case with modified transport coefficients and fueling rate to achieve similar upstream profiles.

In order to exclude the influence of the enhanced upstream density, we modified the transport coefficients and fueling rates in the above X-divertor case to achieve similar upstream profiles as those in the single null case. The

results are shown by the dashed lines in Figs. 7.15 and 7.16 and in the lower row in Fig. 7.17. The radiation and ionization rates are both lower compared to the above X-divertor case. The maximum electron density at the outer target is 1.0×10^{20} m^{-3}, which is much lower than the case above. The temperature at the outer target is similar to that in the single null case, showing an attached outer target. The power fluxes are higher than those in the above X-divertor case but still lower than those in the single null case.

7.3 Summary

In this chapter, we applied the SOLPS-ITER code package to predict the plasma conditions in alternative divertor configurations (ADCs) in the future upper divertor in AUG. The transport coefficients, boundary conditions and gas puffing rates in the simulations are selected to reproduce the experimentally measured profiles in the upper single null configuration in AUG. Using the same input parameters, the plasma conditions in the single null case were then extrapolated to those in the low-field side snowflake minus (LFS SF$^-$) and the X-divertor configurations. Similar as in chapter 5, the simulation results showed much lower power loads at the divertor targets in these alternative divertor configurations, especially in the snowflake case. This confirms the findings in the previous chapters and makes an optimistic prediction for the power exhaust performance of the alternative divertor configurations in the future upper divertor in AUG.

Chapter 8

Drifts effects

In the previous chapters, drifts were not included in the simulations. On the one hand, the previous chapters focus on the effect of divertor configurations. Drifts can influence the power loads at the divertor targets [21, 30, 31], but the effect is moderate for the power exhaust problem. On the other hand, SOLPS simulations with drifts are numerically very expensive, especially in a snowflake geometry. With more boundaries, grid cells and numerical instabilities, the simulation for a snowflake configuration typically takes at least twice as long as that for a single null configuration. However, in order to provide a more complete physical understanding of the snowflake configuration, the effect of drifts should be studied more or less. In experiments in single null configuration, drifts were considered to contribute to a detachment asymmetry between the inner and outer divertor and a modification of the cross-field transport [20, 21]. Besides, in the snowflake configuration, one of the main benefits is its capability to distribute power and particle fluxes among its strike points. Drift, e.g. increasing radial cross-field transport, are expected to play an important role in this [11]. For example, in EMC3-EIRENE simulations for the snowflake configuration in TCV, the modelling without drifts [16, 22] underestimated the heat flux at the secondary strike point by about one order of magnitude compared to experimental measurements [15]. In a subsequent work [23], a qualitative explanation for the activation of the secondary strike point was found by computing drift terms on the plasma background given by EMC3-EIRENE. However, a quantitative and self-consistent simulation is still missing.

For the simulations in chapters 5 and 6, the SOLPS5.0 code package was applied since the SOLPS-ITER package was still developing while these studies were carried out. At the end of 2018, the first commonly available version of SOLPS-ITER was released. Compared to SOLPS5.0, the SOLPS-ITER code package contains a more complete description of the drifts. A speed-up method [96] developed recently made it possible to achieve faster convergence of the

simulations. This makes it more convenient to study drift effects in a self-consistent simulation. In this chapter, the first SOLPS-ITER simulation for the low-field side snowflake minus (LFS SF$^-$) configuration with drifts fully activated is presented and compared to a reference without drifts. Part of the content of this chapter has also been published in [97].

8.1 Simulation setup

In this work, the simulation grids for the plasma is very similar to the one used in chapters 5 and 6, while a triangle mesh (see Fig. 4.5) for kinetic neutrals required by SOLPS-ITER is added. Diamagnetic and E×B drifts, as well as ion fluxes caused by forces related to viscosity, ion-neutral friction and inertia are all fully activated. As introduced in chapter 4, the equations are chosen according to Ref. [77] where a reasonable trade-off was made between physical accuracy and numerical stability. Figure. 8.1 shows the coordinates for the low-field side snowflake minus grids. The x (poloidal) and y (radial) directions in the different regions of the grid are marked by the black and white arrows, respectively. The arrows point into the positive direction, along which the cell index increases.

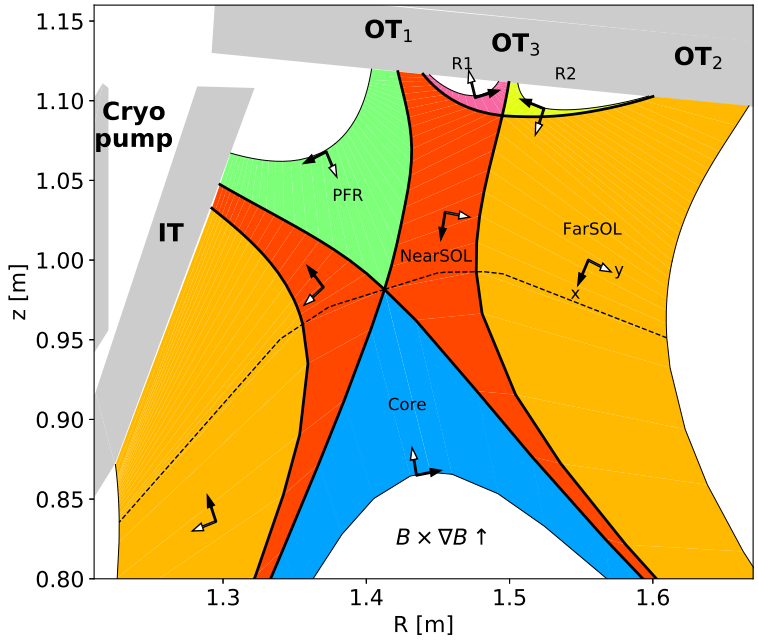

FIGURE 8.1: The low-field side snowflake minus (LFS SF$^-$) divertor configuration simulated in this work. The black and white arrows point into the positive x (poloidal) and y (radial) directions, respectively. The divertor entrance is marked by the dashed line. Taken from [97].

The plasma is assumed to be pure deuterium. The deuterium ion density and the electron and ion temperatures are fixed at the innermost simulation boundary at 2×10^{19} m^{-3} and 200 eV, respectively. Spatially constant diffusive particle and heat transport coefficients are chosen as $D_n^{AN} = 0.5$ m^2/s and $\chi_e^{AN} = \chi_i^{AN} = 1.0$ m^2/s, respectively, resulting in the radial profiles depicted in Fig. 8.2 with a temperature decay length of about 10 mm in the near SOL. This decay length is a typical value in AUG attached discharges [53]. The toroidal magnetic field points into the paper leading to an upward $\vec{B}\times\nabla B$ ion drift towards the upper divertor.

8.2 Simulation results

In order to show the effect of drifts clearly, here we compare the case with drifts activated to a reference case without drifts but with the same input parameters otherwise.

The density, temperature, pressure and potential profiles at the outer mid-plane (OMP) in these two cases are shown in Fig. 8.2. Compared to the non-drift case with the same particle diffusion coefficient $D_n^{AN} = 0.5$ m^2/s (green dashed line in Fig. 8.2 (a)), the density profile in the drift case (blue solid line in Fig. 8.2 (a)) is flatter due to the drift effect on the radial transport. The different upstream density then makes the comparison at the target difficult. For this reason, the particle transport coefficient in the non-drift case is increased to $D_n^{AN} = 1.0$ m^2/s to achieve similar upstream density, temperature and pressure profiles (black dashed line in Fig. 8.2), while χ_e^{AN} and χ_i^{AN} are kept at 1.0 m^2/s. The power balance in the simulations with and without drifts are summarised in Table 8.1. It is found that the integral radial power flux cross the innermost boundary (Q_{core}) and leaving the outermost boundary (Q_{wall}) are both slightly higher in the non-drifts case, while the power to the targets (Q_{tar}) are similar. This means that the global power balance is similar in these two case.

In the case with drifts, the potential radially increases inside the separatrix and decreases in the far-SOL, which causes the radial electric field to change its sign (pink line in Fig. 8.2 (d)).

Figure 8.3 shows the profile of the poloidal ion particle flux caused by drifts at the outer mid-plane. The poloidal E×B and diamagnetic fluxes are shown by blue and green dashed lines, and the flux ($\Gamma_{drift,x} = \Gamma_{E\times B,x} + \Gamma_{dia,x}$) is plotted by the black solid line. Near the primary separatrix ($r_u = 0$), $\Gamma_{E\times B,x}$ and $\Gamma_{dia,x}$ have opposite signs and tend to cancel each other. In the far-SOL, $\Gamma_{E\times B,x}$ and $\Gamma_{dia,x}$ are pointing into the same direction and lead to an anticlockwise poloidal flux, i.e. poloidally from the high-field side to the

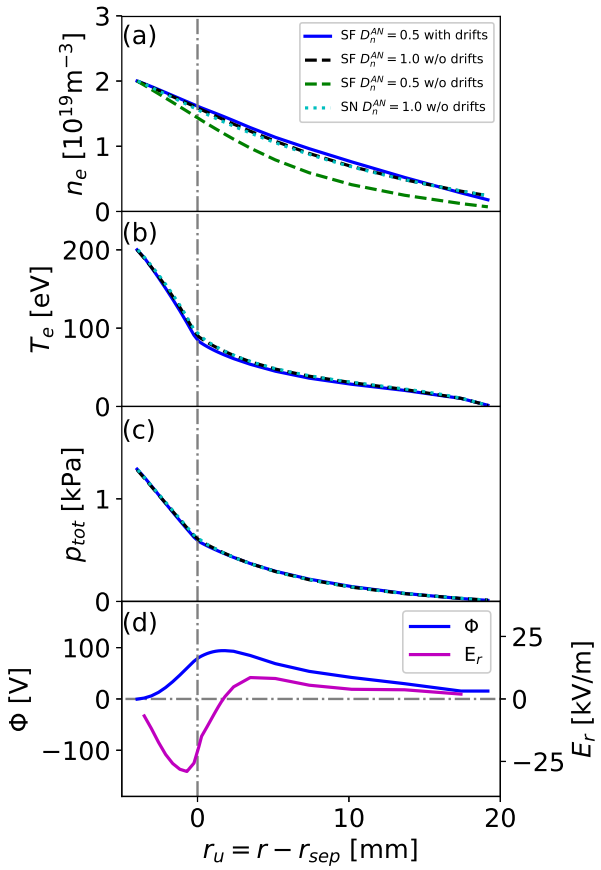

FIGURE 8.2: (a) Electron density, (b) electron temperature, (c) total pressure, (d) plasma potential and radial electric field profiles at the outer mid-plane. Profiles in the drift case are shown by solid lines, and those in non-drift cases are shown by dashed lines. Taken from [97].

low-field side along the poloidal coordinate in the SOL.

To investigate how drifts impact the divertor target power loads, we show the distribution of the total drift particle flux in the divertor region in Fig. 8.4, and the target profiles of the parallel power flux, electron density, electron temperature, total pressure and current in Fig. 8.5. The target profiles are compared with those in the case without drifts (shown by black dashed lines). Figures 8.4 (a) and (b) show the poloidal and radial projections of the total drift flux. In the SOL, the poloidal drift is mainly transporting particles from the high-field side to the low-field side where it is split between the outer targets OT1 and OT2. Since the particle fluxes lead to a convective term in the power flux expression [77], it is expected that the drifts have an impact on the power flux too. This is indeed seen in Figs. 8.5 (a) and (f) which show a lower energy flux at the inner target and higher ones at OT1 and OT2 near

Power [MW]	With drifts ($D_n^{AN} = 0.5$ m^2/s)	Without drifts ($D_n^{AN} = 1.0$ m^2/s)
$\mathbf{Q_{core}}$	1.91	2.01
$\mathbf{Q_{wall}}$	-0.74	-0.85
$\mathbf{Q_{tar}}$	-1.01	-1.04
$\mathbf{Q_{rad}}$	-0.13	-0.10

TABLE 8.1: Power balance in the simulations with and without drifts. Q_{core} is the power flux through the innermost radial boundary and Q_{wall} is the one leaving the plasma through the outermost radial boundary of the regions FARSOL, PFR, R1 and R2. Q_{tar} is the total power to the divertor targets IT, OT1, OT2 and OT3. Q_{rad} is the total radiation power. Taken from [97].

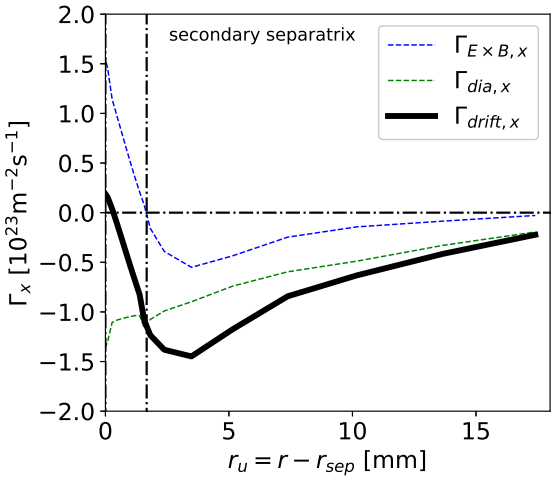

FIGURE 8.3: Poloidal particle fluxes caused by drifts at the outer mid-plane. The poloidal E×B and diamagnetic fluxes are shown by blue and green dashed lines, respectively. The total drift flux is shown by the black solid line. Taken from [97].

the strike points in the drift case. Near the inner target, the large poloidal temperature gradient leads to poloidal electric field and a strong radial outward drift flux (see Fig. 8.4 (b)). It pushes the high density region near the inner strike point towards the far-SOL and cools down the outer part of the inner target, which can be seen in Figs. 8.5 (b) and (c). A region of high density and low temperature in the high-field side far-SOL is seen in the 2D plot in Figs. 8.6 (a) and (b), in contrast to the non-drift case (Figs. 8.6 (c) and (d)).

In the high-field side SOL of the snowflake configuration, the E×B and diamagnetic drifts act quite similar to those in a single null geometry [21, 61], while in the low-field side SOL, the situation becomes more complicated. The drifts not only simply enhance the integrated power flux to the outer targets,

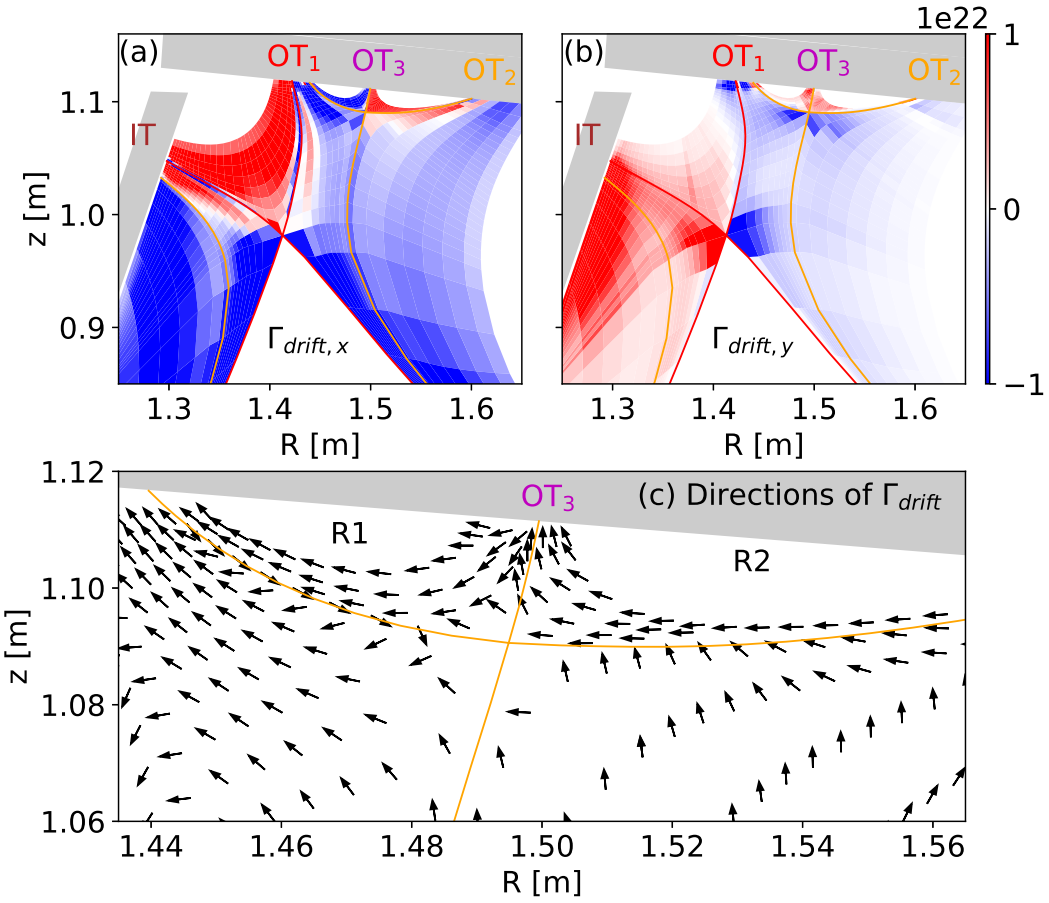

FIGURE 8.4: (a) Poloidal and (b) radial projections of the total drift particle flux in the divertor region. (c) The direction of the total drift flux in the region near OT_3. Taken from [97].

but also have an impact on the distribution of the power to the three intervals (OT1, OT2 and OT3) along the outer target. As shown in Fig. 8.5 (f), due to the radial inward drift in the low-field side SOL (see Fig. 8.4 (b)), more power is transported to OT1 while the outer part of OT2 receives slightly less power compared to the non-drift case. The region near OT3 is magnified in Fig. 8.4 (c), and the arrows point into the direction of the total drift flux. Due to the radial flux across the OT2 divertor leg and the poloidal flux from OT2 to OT3 in the region R2, the peak value of the power flux at OT3 increases by a factor of 4 and becomes comparable to that at OT2. Such an activation of OT3 was observed experimentally in TCV [15, 16] and qualitatively explained by computing drift terms on the plasma background given by EMC3-EIRENE simulations [23]. In the region R1, the poloidal drift flux from OT3 to OT1 partly counteracts the increase of power flux to OT3 and contributes to a small peak in the outer part of the OT1 power flux profile ($s_{ot} \approx 22$ mm). In the

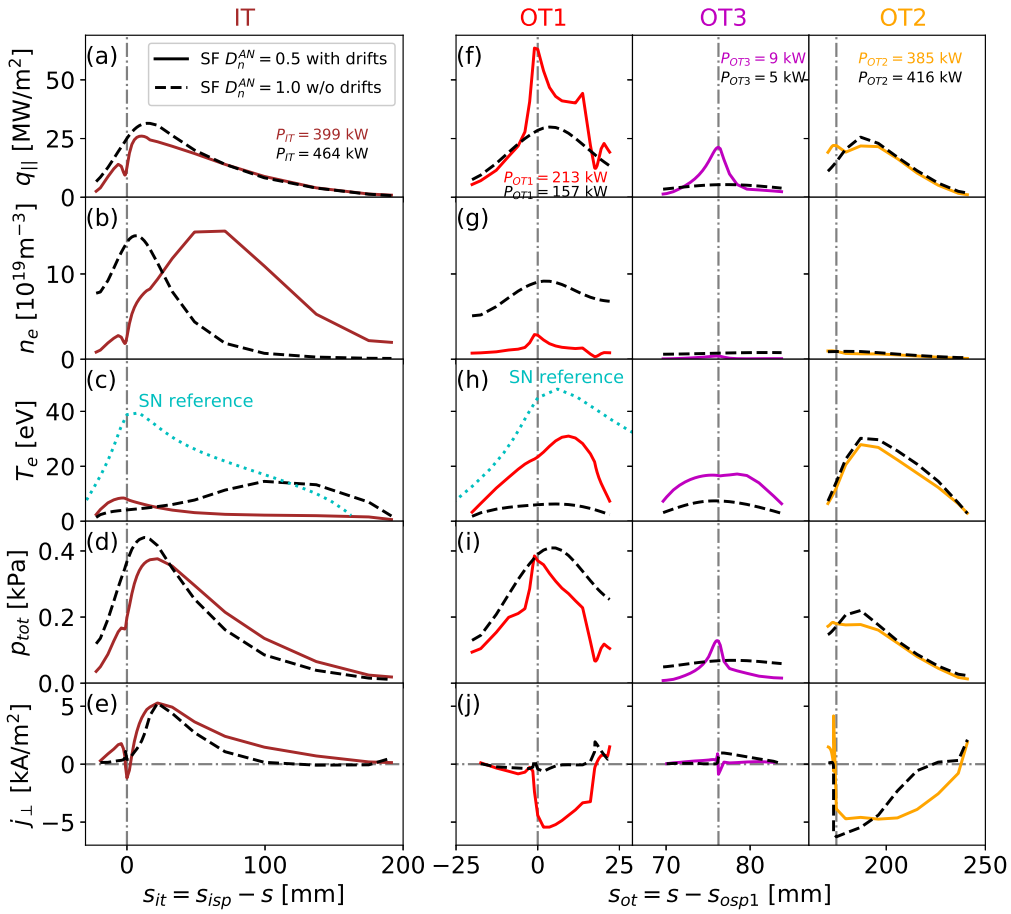

FIGURE 8.5: Parallel energy flux, density, temperature, total pressure and current profiles at inner (left column) and outer (right column) targets, comparing cases with and without drifts. In Figs. 8.5 (a), (e), (f) and (j), the positive value means that the flux points towards the divertor target. The numbers in Figs. 8.5 (a) and (f) are the integrated power to the targets. Taken from [97].

SOL near the targets and just outside the separatrices, reversed drift fluxes are found (see Fig. 8.4 (a) and (c)), which could contribute to multiple peaks in the power flux profiles. Multi-peak target profiles were also observed in single null configurations in JET [60] and in snowflake configurations in TCV [15]. EDGE2D [98] and SOLPS5.2 [99] simulations showed that the drifts played an important role to explain this phenomenon.

The change of the temperature at the outer targets is the same as the change in the power fluxes, i.e. the temperature increases at OT1 and OT3 and the one at the outer part of OT2 slightly decreases (see Fig. 8.5 (h)). It should be noticed that although the maximum temperature at OT1 (about 30 eV) is increased by drifts, it is still lower than the one (about 45 eV, the cyan dotted line in Fig. 8.5 (h)) in the single null configuration simulated with

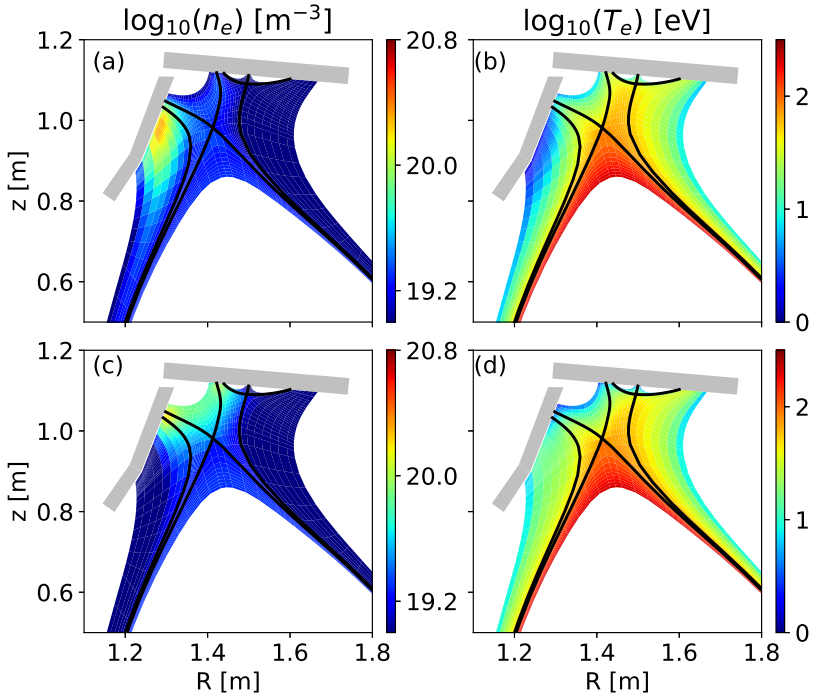

FIGURE 8.6: Electron density and electron temperature in the cases (a,b) with and (c,d) without drifts. Taken from [97].

similar upstream profiles (the cyan dotted lines in Fig. 8.2) and even without drifts. Similar to the snowflake case, one can expect that drifts would also lead to a increase of the maximum temperature at the outer target in the single null case, as discussed in Ref. [100].

The enhanced power flux and temperature at OT1 let the plasma return from a high recycling to one with less recycling, and the strong reduction of the ionization source results in a much lower density (see Fig. 8.5 (g)). The radial drift from the low-field side SOL across the separatrix near the primary X-point and the OT1 divertor leg to the high-field side could also contribute slightly to the reduction of the density, as well as the pressure (see Fig. 8.5 (i)) at OT1. Figures 8.5 (e) and (j) show the total current perpendicular to the inner and outer targets, respectively. In the SOL, the current is dominated by the poloidal projection of the parallel thermal current and travels from the hotter divertor (OT1 and OT2) to the colder one (IT).

8.3 Summary

In summary, converged SOLPS-ITER simulations with drifts fully activated are carried out in a low-field side snowflake minus (LFS SF^-) divertor config-

uration for the first time. The configuration corresponds to that of the future upper divertor of ASDEX Upgrade in normal toroidal field direction ($\vec{B} \times \nabla B$ points to the primary X-point). Comparing with a reference case without drifts but with similar upstream profiles, the simulation with drifts shows a larger low-field-side/high-field-side asymmetry in the power fluxes and an enhanced cross-field transport, especially in the inner divertor.

In addition, a redistribution of particles and power among the primary and secondary strike points is found in the outer divertor. With drifts, the target OT3 magnetically disconnected from the outer mid-plane is remarkably activated reaching a maximum parallel power flux density by a factor of 4 higher than that in the non-drift case. The activation of a secondary strike point like OT3 was one of the motivations to study snowflake configurations [14] and was also observed in experiments [15, 16] and non self-consistent simulations [23] in TCV. Given that the integral power flux to OT3 remains small, the relevance for a reactor still needs to be tested by simulations studying how this effect scales with machine size.

Chapter 9

Conclusion

The power exhaust problem is one of the most critical challenges for the construction of a fusion reactor. In the design of the future reactor DEMO, the maximum power flux density on the plasma facing components (PFCs) at the divertor target is limited to 5 MW/m^2 in order to guarantee a sufficiently long lifetime of the material components [4]. It is estimated that more than 95 % [4, 6] of the power transported from the plasma core into the scrape-off layer (SOL) needs to be dissipated before reaching the target. The operation of tokamak plasma in such a high radiative regime is challenging and can lead to instabilities and confinement degradation [88]. In addition to that, the ion particle flux to the targets can be so high that the power flux related to the energy released by the recombining ions at the surface alone would exceed the material limits [6]. For this reason, a detached divertor regime is required, in which volumetric processes and cross-field transport reduce also the particle fluxes before reaching the target [6]. Divertor concepts, which can reduce the power load at the target and achieve a higher radiative power fraction and a higher degree of divertor detachment without confinement degradation, are therefore strongly required.

The present divertor concepts for future fusion reactors rely on magnetic configurations with a single magnetic X-point. Divertor configurations with a second magnetic X-point, such as the X-divertor (XD) and the snowflake divertor (SF), are currently discussed as alternative solutions for the power exhaust problem. In the X-divertor, the magnetic field lines are flared in the divertor region by creating another X-point just in front of the divertor target surface. Thus a large poloidal flux expansion can potentially increase the plasma-wetted area. In the low-field side snowflake minus (LFS SF^-) configuration, a secondary X-point is located in the low-field side SOL near the primary X-point. The geometrical splitting of the SOL as well as the weak poloidal field region around the X-points are supposed to modify the energy transport and dissipation in the divertor region.

For the ASDEX Upgrade tokamak (AUG), it was recently decided to modify its upper divertor to study the alternative divertor configurations experimentally in a machine with a high heating power compared to its size.

Numerical simulations were used to get a better insight into their capacity of alternative divertors in solving the power exhaust problem. In this thesis, the SOLPS code package, which contains the relevant atomic and molecular processes including volumetric recombination and a comprehensive description of drifts, has been successfully applied for simulating the snowflake configuration foreseen for the future upper divertor of AUG. The additional separatrix branches and strike points were included by applying a new grid generator [74]. This made it possible to carry out the first SOLPS simulations that includes all strike points in the snowflake configuration. It was then possible to gain a more complete understanding of the potential of such a configuration to reduce the power load and facilitate detachment around each of the strike points.

In this study, two alternative divertor configurations, the X-divertor and the snowflake divertor, were compared to the existing single null configuration in AUG. As a start, we focused on the effect of the divertor configuration alone, while keeping the assumptions on the transport simple by using spatially constant transport coefficients in the simulations. Compared to the single null reference case with the same input power as well as similar upstream profiles and separatrix impurity concentrations, the simulations in the alternative divertor configurations showed a substantial reduction of the maximum power load at the target. The radiation fractions were 79 % and 88 % in the X-divertor and snowflake divertor cases, respectively, which were higher than the 71 % of the single null case. This was caused by the larger connection length and poloidal flux expansion in the alternative divertor configurations. A longer residence time of a particle on its way to the target, higher density in the divertor and a larger radiation volume with a suitable electron temperature enhanced the impurity radiation. In the snowflake divertor configuration, the enhanced radiation led to a 68 % lower target power load compared to that expected from a simple analytic SOL splitting model [19] describing the effect of heat diffusion into the additional private flux regions. This implied that the simple analytic model could not be used in such highly radiative scenario. In order to test the robustness and universality of these results and study the potential of the snowflake divertor configuration in facilitating divertor detachment, a more detailed parameter study was carried out by scanning the nitrogen impurity seeding rate. Compared to the single null reference, the snowflake cases showed higher radiative power fractions in the whole scan. Pressure loss between the outer mid-plane and the outer target, which is a sign of divertor detachment, was found at a 20 % lower nitrogen seeding rate in the snowflake divertor configuration. When the impurity seeding rate was sufficiently high,

the upstream pressure decreased in both configurations, which could lead to a degradation of plasma confinement. However, 70 % lower power loads and 50 % lower pressures at the targets, i.e. a higher degree of divertor detachment, was achieved in the snowflake divertor configuration before the upstream pressure degraded. This can be explained by the stronger momentum removal via cross-field transport across the additional divertor legs and by enhanced volumetric processes in the snowflake divertor configuration. This result extended the physical understanding of the snowflake divertor in the previous numerical studies which did not consider the additional strike points. Future numerical and experimental studies are foreseen to scan the radial and poloidal position of the secondary X-point to find an optimized position which leads to the lowest target loads.

Apart from contributing to a better physical insight, numerical simulations are important for predicting the divertor performance in future devices. A reasonable way is to extrapolate the experimental plasma conditions in the present divertor to those in the future one. For this purpose, a series of upper single null H-mode discharges were carried out in AUG and used for the comparison with SOLPS-ITER simulations. Different from the previous simulations with spatially constant transport coefficients, the spatially varying transport coefficients, boundary conditions and gas puffing rates were adapted iteratively to achieve the best overall fit of the experimental measurements at both the outer mid-plane and the target. With the same settings, the performance of the future upper divertor of AUG was investigated. The extrapolation confirmed the findings in the previous simulations and made an optimistic prediction for the power exhaust performance of the alternative divertor configurations. In addition to this, some suggestions for future studies can be made from this extrapolation. Compared to the single null case with the same fueling and seeding rates, the recycling and ionization in the outer divertor were much stronger in the X-divertor, resulting in higher densities not only at the outer target but also at the outer mid-plane. A reference simulation for the X-divertor with the pump switched off predicted a density in the confinement region reaching the Greenwald density limit [95]. For this reason, the pump could be essential in the future experimental operation for density control.

In the snowflake divertor configuration, a region with high density, low temperature and strong radiation was found inside the confinement region near the primary X-point, similar to the X-point radiator found in the lower single null experiments in AUG and JET [94]. The strong radiation in this region contributed to a substantial reduction of the target power load. Even when the input power was increased by a factor of 6 in the snowflake case and reaching the maximum heating capacity of AUG (30 MW), the peak power flux at the

outer target was still a factor of 4 lower than that in the single null case. This means the snowflake divertor (LFS SF^-) can suffer a much higher heating power and may extend the operational window in the future devices. The smaller magnetic pitch angle near the X-points in the snowflake configuration could facilitate the maintenance of the strong poloidal temperature gradient near the radiator. This could also be an attractive benefit of the snowflake divertor configuration and foreseen to be tested in future experiments.

In the last part of the thesis, the drift effects in the LFS SF^- configuration were studied with the SOLPS-ITER code. It is the first SOLPS-ITER simulation with drifts fully activated in such a configuration. Compared to a reference case without drifts but with similar upstream profiles, the simulation with drifts showed a larger low-field-side/high-field-side asymmetry and an enhanced cross-field transport especially in the inner divertor. A redistribution of particles and power among the primary and secondary strike points was found in the outer divertor. With the convective transport driven by drifts, the secondary strike point, which is magnetically disconnected from the outer mid-plane, was activated, reaching a maximum parallel power flux density by a factor of 4 higher than in the non-drift case. The activation of secondary strike points was one of the motivations to study snowflake configurations and was observed in experiments and non-self-consistent simulations in the TCV tokamak [15, 16, 22, 23]. The simulation in this thesis contributes to identifying the nature of the enhanced transport near the X-points in the snowflake configuration. Given that the integral power to the secondary strike point is still small compared to the total input power, this effect could be negligible when studying the power exhaust in a medium-size tokamak like AUG. However, the relevance for a large-size reactor like DEMO still needs to be tested by future simulations studying how this effect scales with machine size.

In conclusion, an optimistic prediction for the power exhaust performance of the alternative divertor configurations of the future upper AUG divertor can be made from this thesis.

For future research, there are still many open questions about the alternative divertor configurations, including the impurity transport with drifts, simulations for edge localized modes which require spatially and temporarily varying transport coefficients, neoclassical and turbulent transport especially in the region near the X-point and three-dimensional effects.

Bibliography

[1] D. E. Post *et al.*, *ITER physics* (IAEA, Vienna, 1991).

[2] H. Zohm *et al.*, Nucl. Fusion **53**, 073019 (2013).

[3] R. Wenninger *et al.*, Nucl. Fusion **57**, 016011 (2016).

[4] R. Wenninger *et al.*, Nucl. Fusion **54**, 114003 (2014).

[5] T. Eich *et al.*, Phys. Rev. Lett. **107**, 215001 (2011).

[6] M. Wischmeier *et al.*, J. Nucl. Mater. **463**, 22 (2015).

[7] O. Gruber *et al.*, Phys. Rev. Lett. **74**, 4217 (1995).

[8] J. Neuhauser *et al.*, Plasma Phys. Control. Fusion **37**, 37 (1995).

[9] S. I. Krasheninnikov *et al.*, Contrib. Plasma Phys. **36**, 314 (1996).

[10] A. Loarte *et al.*, Nucl. Fusion **38**, 331 (1998).

[11] V. A. Soukhanovskii *et al.*, Plasma Phys. Control. Fusion **59**, 064005 (2017).

[12] M. Kotschenreuther *et al.*, Phys. plasmas **14**, 072502 (2007).

[13] D. D. Ryutov *et al.*, Phys. Plasmas **14**, 064502 (2007).

[14] D. Ryutov and V. Soukhanovskii, Phys. Plasmas **22**, 110901 (2015).

[15] H. Reimerdes *et al.*, Plasma Phys. Control. Fusion **55**, 124027 (2013).

[16] T. Lunt *et al.*, Plasma Phys. Control. Fusion **56**, 035009 (2014).

[17] B. Labit *et al.*, Nucl. Mater. Energy **12**, 1015 (2017).

[18] ASDEX Upgrade Design Team and Tokamak Theory Group, IPP 1/197 **1**, 1 (1982).

[19] T. Lunt *et al.*, Nucl. Mater. Energy **12**, 1037 (2017).

[20] S. Potzel *et al.*, Nucl. Fusion **54**, 013001 (2015).

[21] F. Reimold *et al.*, Nucl. Mater. Energy **12**, 193 (2017).

[22] T. Lunt *et al.*, Plasma Phys. Control. Fusion **58**, 045027 (2016).

[23] G. P. Canal *et al.*, Nucl. Fusion **55**, 123023 (2015).

[24] E. T. Meier *et al.*, J. Nucl. Mater. **463**, 1200 (2015).

[25] E. T. Meier *et al.*, Nucl. Fusion **55**, 086002 (2015).

[26] R. Mao *et al.*, Contrib. Plasma Phys. **58**, 781 (2018).

[27] R. Schneider *et al.*, Contrib. Plasma Phys. **46**, 3 (2006).

[28] S. Wiesen *et al.*, J. Nucl. Mater. **463**, 480 (2015).

[29] F. Reimold, *Experimental studies and modeling of divertor plasma detachment in H-mode discharges in the ASDEX upgrade tokamak* (Technical University Munich, Munich, Germany, 2015).

[30] L. Aho-Mantila *et al.*, Nucl. Fusion **52**, 103006 (2012).

[31] L. Aho-Mantila *et al.*, Plasma Phys. Control. Fusion **59**, 035003 (2017).

[32] J. Wesson and D. J. Campbell, *Tokamaks* (Oxford university press, Oxford, 2011).

[33] J. D. Lawson *et al.*, Proceedings of the Physical Society **70**, 6 (1955).

[34] L. Spitzer *et al.*, The Physics of Fluids **1**, 253 (1958).

[35] M. Keilhacker *et al.*, in *Tokamak Reactors for Breakeven* (Pergamon, Oxford, 1978), Vol. 1, Chap. Magnetic divertors, p. 171.

[36] M. Keilhacker *et al.*, Physica Scripta **1982**, 443 (1982).

[37] S. I. Krasheninnikov *et al.*, J. Plasma Phys. **83**, 155830501 (2017).

[38] F. Wagner *et al.*, Phys. Rev. Lett. **49**, 1408 (1982).

[39] B. Streibl *et al.*, Fusion Sci. Technol. **44**, 578 (2003).

[40] M. Bernert *et al.*, Rev. Sci. Instrum. **53**, 104003 (2014).

[41] H. Murmann *et al.*, Rev. Sci. Instrum. **63**, 4941 (1992).

[42] B. Kurzan *et al.*, Plasma Phys. Control. Fusion **49**, 825 (2007).

[43] B. Kurzan *et al.*, Rev. Sci. Instrum. **82**, 103501 (2011).

[44] S. K. Rathgeber *et al.*, Plasma Phys. Control. Fusion **55**, 025004 (2012).

[45] M. Griener *et al.*, Plasma Phys. Control. Fusion **60**, 025008 (2017).

[46] E. Viezzer *et al.*, Rev. Sci. Instrum. **83**, 103501 (2012).

[47] M. Weinlich and A. Carlson, Contrib. Plasma Phys. **36**, 53 (1996).

[48] D. Brida, *Experimental and numerical investigation of power exhaust in the tokamak ASDEX upgrade with magnetic perturbations* (Technical University Munich, Munich, Germany, 2018).

[49] A. Herrmann *et al.*, Plasma Phys. Control. Fusion **37**, 17 (1995).

[50] B. Sieglin *et al.*, *Experimental Investigation of Heat Transport and Divertor Loads of Fusion Plasma in All Metal ASDEX Upgrade and JET* (Technical University Munich, Munich, Germany, 2014).

[51] D. Bohm *et al.*, *The characteristics of electrical discharges in magnetic fields* (A. Guthrie and RK Wakerling, New York, USA, 1949).

[52] R. Chodura *et al.*, in *Physics of plasma-wall interactions in controlled fusion* (Springer, Boston, 1986), Vol. 1, Chap. Plasma flow in the sheath and the presheath of a scrape-off layer, p. 99.

[53] H. J. Sun *et al.*, Plasma Phys. Control. Fusion **59**, 105010 (2017).

[54] M. A. Makowski *et al.*, Phys. Plasmas **19**, 056122 (2012).

[55] T. Eich *et al.*, Plasma Phys. Control. Fusion **49**, 573 (2007).

[56] P. C. Stangeby *et al.*, *The plasma boundary of magnetic fusion devices* (Institute of Physics Pub., Philadelphia, Pennsylvania, 2000).

[57] H. P. Summers *et al.*, Plasma Phys. Control. Fusion **48**, 263 (2006).

[58] A. Kallenbach *et al.*, Plasma Phys. Control. Fusion **55**, 124041 (2013).

[59] H. P. Summers, *ADAS user manual* (The ADAS Project, UK, 2004).

[60] A. Loarte *et al.*, Nucl. Fusion **38**, 331 (1998).

[61] F. Reimold *et al.*, Nucl. Fusion **55**, 033004 (2015).

[62] A. Kallenbach *et al.*, Nucl. Fusion **55**, 053026 (2015).

[63] A. Loarte *et al.*, Plasma Phys. Control. Fusion **43**, 183 (2001).

[64] H. Kawashima *et al.*, Fusion Sci. Technol. **49**, 168 (2006).

[65] I. Mazul *et al.*, Nucl. Fusion **56**, 126009 (2016).

[66] D. D. Ryutov *et al.*, Phys. Plasmas **20**, 092509 (2013).

[67] C. S. Pitcher and P. C. Stangeby, Plasma Phys. Control. Fusion **39**, 779 (1997).

[68] J. Kesner *et al.*, Nucl. Fusion **30**, 548 (1990).

[69] D. K. Owens *et al.*, J. Nucl. Mater. **93**, 213 (1980).

[70] P. M. Valanju *et al.*, Fusion Eng. Des. **85**, 46 (2010).

[71] I. Katramados *et al.*, Fusion Eng. Des. **86**, 1595 (2011).

[72] G. Fishpool *et al.*, J. Nucl. Mater. **438**, 356 (2013).

[73] Y. Feng *et al.*, Contrib. Plasma Phys. **44**, 57 (2004).

[74] O. Pan *et al.*, Plasma Phys. Control. Fusion **60**, 085005 (2018).

[75] D. Reiter *et al.*, Fusion Sci. Technol. **47**, 172 (2005).

[76] B. J. Braams *et al.*, *Hydrodynamic and Hydromagnetic Stability* (Oxford University Press, Princeton, USA, 1987).

[77] V. Rozhansky *et al.*, Nucl. Fusion **49**, 025007 (2009).

[78] A. S. Kukushkin *et al.*, Fusion Eng. Des. **86**, 2865 (2011).

[79] T. D. Rognlien *et al.*, Phys. Plasmas **6**, 1851 (1999).

[80] *SOLPS-ITER user manual* (ITER organization, France, 2019).

[81] V. A. Rozhansky *et al.*, Nucl. Fusion **41**, 387 (2001).

[82] A. V. Chankin *et al.*, Plasma Phys. Control. Fusion **36**, 1485 (1994).

[83] C. M. Rhie and W. L. Chow, AIAA journal **21**, 1525 (1983).

[84] D. Reiter *et al.*, *The EIRENE Code User Manual* (Forschungszentrum Juelich GmbH, Juelich, Germany, 2019).

[85] W. Eckstein *et al.*, IPP Report **17**, 1 (2009).

[86] T. Lunt and O. Pan, Nucl. Mater. Energy **19**, 107 (2019).

[87] A. S. Kukushkin *et al.*, Nucl. Fusion **43**, 716 (2003).

[88] A. W. Leonard *et al.*, Plasma Phys. Control. Fusion **60**, 044001 (2018).

[89] A. G. Mclean *et al.*, J. Nucl. Mater. **463**, 533 (2015).

[90] A. A. Pshenov *et al.*, Phys. Plasmas **24**, 072508 (2017).

[91] A. V. Chankin *et al.*, Plasma Phys. Control. Fusion **46**, 839 (2006).

[92] ITER Physics Expert Groups on Confinement, Transport, Confinement Modelling, and Database, Nucl. Fusion **39**, 2175 (1999).

[93] R. Fischer *et al.*, Fusion Sci. Technol. **58**, 675 (2010).

[94] M. Bernert *et al.*, Nucl. Mater. Energy **12**, 111 (2017).

[95] M. Greenwald *et al.*, Plasma Phys. Control. Fusion **44**, 27 (2002).

[96] E. Kaveeva *et al.*, Nucl. Fusion **58**, 126018 (2018).

[97] O. Pan *et al.*, Plasma Phys. Control. Fusion **62**, 045005 (2020).

[98] A. V. Chankin *et al.*, Plasma Phys. Control. Fusion **43**, 299 (2001).

[99] V. Rozhansky *et al.*, Nucl. Fusion **52**, 103017 (2012).

[100] I. P. Pérez *et al.*, Contrib. Plasma Phys. **1**, 201900166 (2020).

Publications:

1. O. Pan, Y. Xu, *et al.*, "Evidence of enhanced self-organized criticality (SOC) dynamics during the radially non-local transient transport in the HL-2A tokamak", Nucl. Fusion **55**, 113010 (2015).

2. O. Pan, *et al.*, "SOLPS simulations of detachment in a snowflake configuration for the future upper divertor in ASDEX Upgrade", Plasma Phys. Control. Fusion **60**, 085005 (2018).

3. T. Lunt, O. Pan, *et al,*. "2D and 3D studies of the X-divertor configuration in the future upper divertor of ASDEX upgrade". Nucl. Mater. Energy **19**, 107–112 (2019).

4. O. Pan, *et al.*, "SOLPS-ITER modeling with activated drifts for a snowflake divertor in ASDEX Upgrade", Plasma Phys. Control. Fusion **62**, 045005 (2020).